STUDY OF THE ELECTRODYNAMICS OF CUPRATE SUPERCONDUCTORS BY A NOVEL SURFACE IMPEDANCE MEASUREMENT TECHNIQUE

by

Jian Mao

Dissertation submitted to the Faculty of the Graduate School
of The University of Maryland in partial fulfillment
of the requirements for the degree of
Doctor of Philosophy
1995

UNIVERSITY OF MARYLAND

DEPARTMENT OF PHYSICS

COLLEGE PARK, MARYLAND 20742

ABSTRACT

Title of Dissertation: STUDY OF THE ELECTRODYNAMICS OF CUPRATE
SUPERCONDUCTORS BY A NOVEL SURFACE
IMPEDANCE MEASUREMENT TECHNIQUE

Jian Mao, Doctor of Philosophy, 1995

Dissertation directed by: Assistant Professor Steven M. Anlage
Department of Physics

We studied the microwave surface impedance of superconductors by employing a novel cavity perturbation technique. We have refined the technique in both theoretical and experimental aspects. To clarify the existing confusion about the interpretation of the measured quantities , we carried out a first principles calculation by considering the fundamental principles underlying microwave perturbation measurements. Measurements were performed using a recrystallized Nb cavity which has a very high $Q \sim 2.3 \times 10^7$ and a resonant frequency stability $\delta f/f \sim 10^{-10}$ at T $= 4.2$ K.

In addition, we measured the electrodynamic properties of Nb, $Nd_{1.85}Ce_{0.15}CuO_{4-y}$ (NCCO) and $YBa_2Cu_3O_{7-\delta}$ (YBCO) unambiguously. For the first time, we demonstrated the exponentially activated behavior at low temperatures of the in-plane penetration depth $\lambda_{||}$ and surface

resistance R_s of NCCO. The results reveal striking similarities to Nb, and can be well described within the BCS framework, yielding an energy gap ratio $2\Delta/k_BT_c = 4.1\pm0.2$ and the London penetration depth $\lambda_{LI}(0\ K) \sim 1000$ Å, indicating that the electrodynamics of NCCO is consistent with a single-gap s-wave BCS behavior. For YBCO single crystals, the anisotropic surface resistance $R_{s\text{-}ab}$ and $R_{s\text{-}c}$, as well as the penetration depth λ_{ab} and λ_c, are clearly inconsistent with s-wave BCS theory. $\lambda_c(T)$ and $\lambda_{ab}(T)$ are linear in temperature at low temperatures with very different slopes, consistent with the existence of line nodes on the Fermi surface. A rather unusual rapid decrease of quasiparticle scattering rate in the ab plane and c-axis below T_C is also observed. Also fluctuation effects are evident in the behavior of $\lambda_{ab}(T)$ and $\sigma(T)$ of YBCO crystals in the vicinity of T_C.

The distinct differences between NCCO and YBCO, although both of them possess several common features such as CuO planes, may suggest that the pairing in cuprates includes both s-wave and d-wave components, and that the dominant component may vary from one material to another. With this possible scenario, we made a brief discussion on the consequences of d-wave superconductivity for high frequency applications.

STUDY OF THE ELECTRODYNAMICS OF CUPRATE SUPERCONDUCTORS BY A NOVEL SURFACE IMPEDANCE MEASUREMENT TECHNIQUE

by

Jian Mao

Dissertation submitted to the Faculty of the Graduate School
of The University of Maryland in partial fulfillment
of the requirements for the degree of
Doctor of Philosophy
1995

Advisory   Committee
         Assistant Professor Steven M. Anlage, Chairman/Advisor
         Professor R. L. Greene
         Professor T. Venkatesan
         Professor Chuan Sheng Liu
         Professor Kawthar A. Zaki

DEDICATION

To my parents

ACKNOWLEDGMENTS

I owe my thanks to many people, whose encouragement, support and collaboration made this dissertation work possible.

I am grateful for my advisor Professor Steven M. Anlage for introducing me to microwave techniques which is used throughout this thesis work. His guidance, encouragement, support and insight are essential to keep me working fruitfully and complete this task.

I thank Dr. Dong Ho Wu. His expertise and valuable experience in the microwave characterization kept me going through many difficulties. Thanks for working late into the morning with me many times and thanks for many interesting and helpful discussions.

Without Dr. J. L. Peng's crystals and Sining Mao's thin film samples, this work could not be done. I like to thank them for providing me samples, as well as many helpful discussions and suggestions. The close collaboration is critical to improve the microwave properties of the samples used in this work.

It was a pleasure to work with Michael Pambianchi and James Booth who shared the high frequency lab at the Center for Superconductivity Research (CSR). Under the guidance of Professor Anlage, we together built up every piece of our microwave lab in a few years. I learn many interesting ideas from them through many frank and

TABLE OF CONTENTS

LIST OF TABLES

LIST OF FIGURES

ix

CHAPTER 1

INTRODUCTION

Since Bednorz and Müller's paper[1] on "Possible High T_c Superconductivity in the Ba-La-Cu-O System" was published in 1986, high temperature superconductors with CuO planes, which are also called cuprate superconductors, have been found in many systems. The transition temperature has reached 134 K in $HgBa_2Ca_2Cu_4O_{8+\delta}$[2] at normal pressure. Many systems such as $YBa_2Cu_3O_{7-\delta}$,[3] $Tl_2Ba_2CaCu_2O_8$[4] with transition temperatures T_c above the liquid nitrogen boiling point of 77 K offer great opportunities to explore superconducting devices that outperform devices based on conventional technology.[5 - 8] Because of this, a tremendous effort worldwide to investigate the material properties and the mechanism of high temperature superconductivity has been going on for the last 8 years. This work presented here is related to my investigation related to these issues.

1-1   The Implication of Microwave Measurements

Why do we measure the microwave properties of high temperature superconductors?

Microwave surface impedance measurements of high temperature superconductors provide essential information on the fundamental physics of cuprates and their applications. From the measured surface impedance, we can extract the conductivity σ and the penetration depth

1

λ.[9 - 11] The temperature dependence of the penetration depth $\lambda(T)$ of a superconductor, especially at low temperatures, as well as the conductivity $\sigma(T)$, are directly related to the symmetry of the ground state wave function and the electronic excitations of the superconductor. Therefore, microwave surface impedance measurements, which probe the electrodynamic response of a superconductor, may also help to answer these most important problems in the study of cuprate superconductors today. Also, one of the most promising applications for high T_c superconductors is in microwave devices, such as filters for cellular base stations.[12] Applications of superconductors at high frequencies rely mainly on their low surface resistance properties along with the frequency independent magnetic penetration depth. Hence the high frequency properties, which may be described by a single complex parameter - the surface impedance Z_s, are essential to the design and manufacture of such devices. The study of the fundamental pairing state is related to this technological application. For instance, if the cuprates are s-wave superconductors, then their surface resistance, at least in principle, can be made arbitrarily small by perfecting the material and going to low enough temperatures. By contrast, if the cuprates are d-wave superconductors, there is a finite intrinsic minimum surface resistance.[9] Since both the order parameter and the microstructure strongly influence the physical properties of the cuprates, understanding the physics of these materials is essential for engineering systems.

1-2   High T_c Cuprates: YBCO and NCCO

YBCO and $Nd_{1.85}Ce_{0.15}CuO_{4-y}$ (NCCO) are two of the most interesting and important members in the new class of high T_c cuprates. YBCO with a transition temperature around 93 K, has a comfortable margin over the liquid nitrogen boiling point of 77 K, and is easy to fabricate. This is important for high T_c applications because if a superconducting device can be operated above 77 K, the cooling cost and related complexity can be greatly reduced. High quality films of YBCO have been made by various methods. For instance, the microwave losses of YBCO have been brought as low as 180 $\mu\Omega$ at 10 GHz at 77 K, the lowest microwave loss among the cuprates[13]. Hence YBCO remains by far the most intensively investigated cuprate system and together with $Tl_2Ba_2CaCu_2O_8$ has been the most widely applied materials for high T_c microwave applications.[14 - 17] While YBCO has a transition temperature about 93 K, NCCO has only $T_c \sim 23$ K. The T_c of NCCO is not much different from that of Nb_3Sn, which is a conventional superconductor without CuO planes. Understanding the mechanism of superconductivity in these systems may help us to find a way to engineer room temperature superconductors one day, which is the biggest dream in this field. While the charge carriers in YBCO are holes, NCCO is the one compound among the copper oxide superconductors in which the charge carriers appear to be electrons[18], although recent report suggests evidence of possible hole type carriers.[19] Extensive materials characterization has been done on NCCO[20][21] and YBCO[3][8]. Although both NCCO and YBCO have the CuO plane layered structure, it has been found that the superconducting state properties as well as the normal state properties are distinctly

3

different. The microwave measurements of the penetration depth and the surface resistance of NCCO reveal a single-gap s-wave BCS behavior while similar measurements of YBCO[9][11] and BiSrCaCuO[22] can not be explained by a simple s-wave BCS model.

1-3   The s- vs. d-Wave Controversy

The pair wave function of two electrons can be written as a product of a space and spin part,

$$\Psi(r_1, s_1, r_2, s_2) = \psi(r_1, r_2)\chi(s_1, s_2), \tag{1}$$

where r and s are the spatial and spin coordinates. Because the electrons are fermions with spin s=1/2, the total wave function for a pair of electrons is antisymmetric with respect to an exchange of all the labels of the two particles. The total wave function with total spin S is either a spin singlet (S=0) or a spin triplet (S=1) and can be written as

$$\Psi_{S=0} = \psi_{even}(r_1, r_2)\chi_{odd}^{S=0} \tag{2}$$

$$\Psi_{S=1} = \psi_{odd}(r_1, r_2)\chi_{even}^{S=1} \tag{3}$$

where

$$\psi_{even}(r_1, r_2) = \psi_{even}(r_2, r_1) , \quad \psi_{odd}(r_1, r_2) = -\psi_{odd}(r_2, r_1), \tag{4}$$

$$\chi_{odd}^{S=0}(s_1, s_2) = -\chi_{odd}^{S=0}(s_2, s_1) \text{ and } \chi_{even}^{S=1}(s_1, s_2) = \chi_{even}^{S=1}(s_2, s_1). \tag{5}$$

Thus, for spin singlet state S=0, the space part of the pair wave function must be symmetric, e.g. the orbital angular momentum L must be an even number, such as an s-state, d-state,...; for the spin triplet state S=1, L must be a odd number, such as an p-state, f-state,....

Cooper in 1956 suggested the idea of Cooper pairs, which says that electrons form pairs in the ground state through an electron-phonon

interaction. Bardeen, Cooper and Schrieffer[23, 24] later constructed a many-body generalization of the Cooper pairs. This is the famous BCS model for superconductivity. The ground state wave function for most of the conventional superconductors in the BCS model for many electrons is an antisymmetric product of identical pair wave functions, where each pair wave function has a total crystal momentum L of zero and a total spin S of zero.

In the early days of the discovery of high temperature superconductors, experiments such as the observation of flux quantization in units of hc/2e in YBCO (fluxoid quantization ring experiment by C. E. Gough[25] and flux lattice studies by P. Gammel[26]) have shown that the superconducting carriers in cuprates consist of paired electrons, just as in conventional superconductors[27]. Knight shift measurements[28-30] below T_c provided evidence that the electron pairs were in a singlet state (S=0). Thus the orbital angular momentum L must be an even number and the orbital part of the wave function must have either s-state (L=0) or d-state (L=2) or g-state or....[27][31]

The controversy of s-wave vs. d-wave pairing in high Tc superconductors has generated lots of hot debate.[31-33]

Figures 1 and 2 provide a general idea of the difference between the s-wave and d-wave pictures. Figure 1 shows these two pictures in terms of the energy gap at the Fermi surface. Figure 2 shows the density of states expected based on these two pictures. For a conventional s-wave superconductor, the energy gap is uniform and the density of states is independent of the angle on the Fermi surface (i. e. the CuO plane). In

5

Conventional s-wave Superconductivity

Fermi Surface

Δ = Energy gap

d-wave Superconductivity

k_y

Fermi Surface

Δ_{max}

$+$

$-$

$+$

$-$

k_x
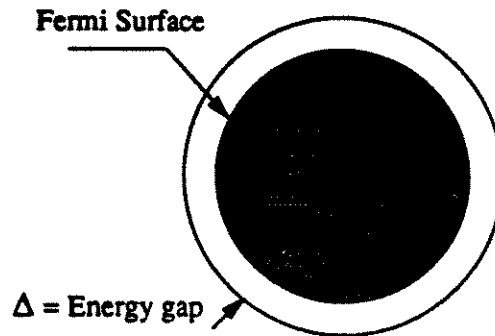
Energy gap = $|\Delta(k)|$

Figure 1.1   (a) A constant energy gap Δ at the Fermi Surface for a conventional s-wave superconductor. (b) The d-wave energy gap at the Fermi surface. Note the gap is a function of the position in the K_{xy} space.

Conventional s-wave Superconductivity

d-wave Superconductivity
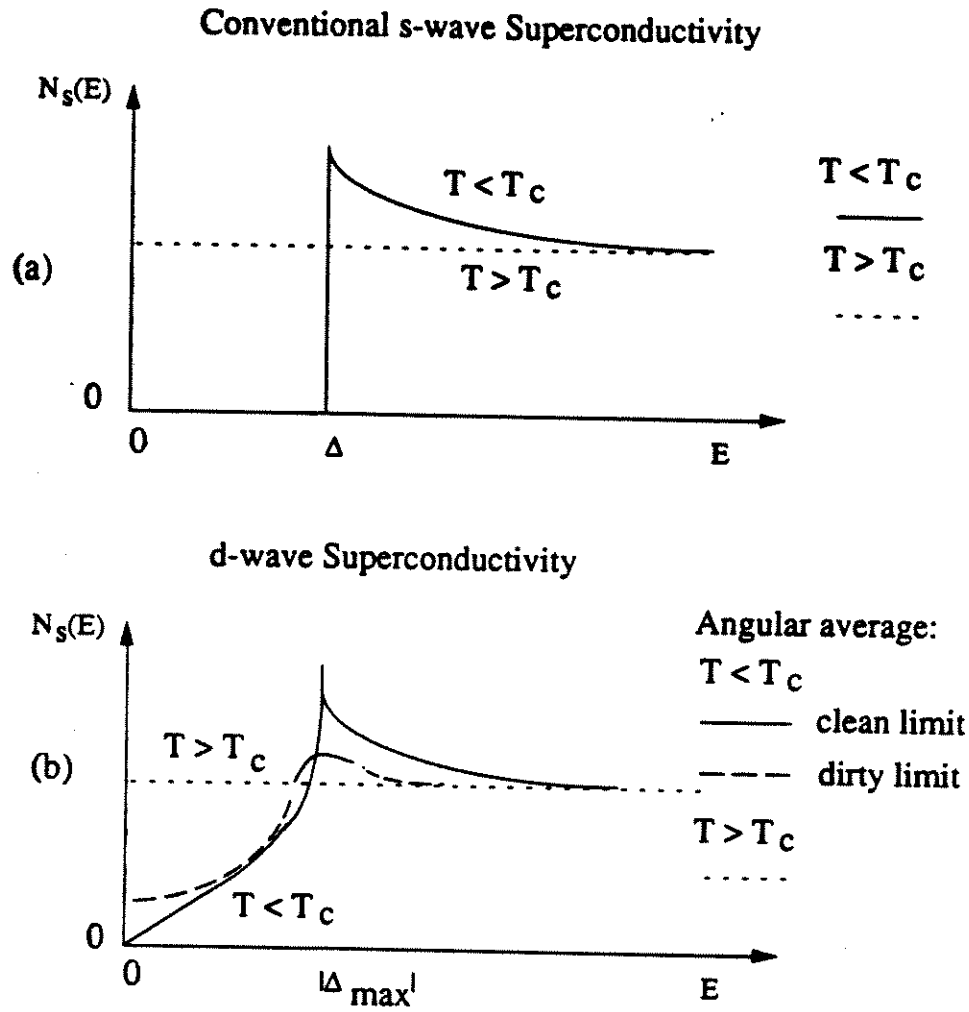
Figure 1.2 The density of states $N_s(E)$ for single electrons expected for s-wave superconductors and d-wave superconductors. Dotted lines represent $T>T_c$ case when there is no superconductivity. At $T<T_c$, (a) Solid line represents the $N_s(E)$ expected for s-wave superconductors; (b) Solid line represents the $N_s(E)$ expected for d-wave superconductors in the clean limit; Dashed line represents the $N_s(E)$ expected for d-wave superconductors in the dirty limit, which remains non zero at zero energy.

contrast, the density of states depends on the angle for a d-wave superconductor. The angular averaged density of states is shown in Figure 2(a).

Many experiments have been done and a lot of new theoretical models have been proposed to explain high temperature superconductivity. Theorists are basically divided into two camps. One believes that the pairing symmetry is s-wave, similar to that of the conventional superconductors, while the other believes the d-wave picture, with models postulating that pairing mechanism involves the exchange of anti-ferromagnetic spin fluctuations and hence suggesting that the pairing in YBCO may occur in the d-wave state.[34-36]

Experiments interpreted as supporting the d-wave picture can be found in

a) quantum interference and tunneling experiments: measurements of flux quantization in tricrystal YBCO grain boundary rings by C. Tsuei[37], tunneling in Pb-YBCO junctions - corner Josephson junction studies by D. Wollman et al.[38] time reversal symmetry experiments by Mathai et al.;[39]

b) evidence of a highly anisotropic gap in Bi2212 crystals by angular resolved photo-emission spectroscopy (ARPES)[40];

c) microwave measurements on YBCO.[10-11]

However, there are other experiments which raise questions regarding the existence of a $d_{x^2-y^2}$ gap. Those include the recent ARPES results of Campuzano et al.[41] in Bi2212, the experiment by Chaudhari and Lin[42] on interfacial tunneling, the c-axis Pb-YBCO Josephson current

8

work by Sun et al.[43] and the microwave measurements by our group on NCCO.[44]

1-4   Summary

In this work, we applied the microwave surface impedance measurement technique to obtain important physical information, such as conductivity and penetration depth, to study the mechanism of cuprate superconductivity and electrodynamics of high temperature superconductors. Although the experimental results do not provide all the clues required to understand the mechanism of the superconductivity in cuprates, the results can be used to obtain more control of the material and the directions of its applications.

This thesis is divided into seven chapters. Development of a resonant cavity perturbation technique and measurement systems will be discussed in Chapter 2. In Chapter 3, we consider the fundamental principles underlying microwave surface impedance and conductivity measurements, and perform a first principles calculation relating the conductivity σ and penetration depth λ to the measured quantities. Examples of bulk and thin film samples are given to illustrate the procedure to obtain σ and λ from the measured quality factor Q and resonant frequency f. Chapter 4 deals with the general material characterization of NCCO and YBCO single crystals and thin films. The surface impedance of YBCO single crystals, high quality NCCO thin films and crystals has been studied systematically and the results are discussed in detail in Chapter 5. Measurements of the conventional superconductor Nb

9

is also performed and the comparison among YBCO, NCCO and Nb are also discussed in Chapter 5. In Chapter 6, we discuss some of the direct theoretical consequences of d-wave superconductivity for high frequency applications. Chapter 7 is a summary of this thesis work.

References

[1] J. G. Bednorz and K. A. Müller, Z. Phys. B 64, 189 (1986).

[2] A. Schilling, M. Cantoni, J. D. Guo, and H. R. Ott, Nature 362, 56 (1993).

[3] M. K. Wu et al., Phys. Rev. Lett. 58, 908 (1987).

[4] Z. Z. Sheng and A. M. Hermann, Nature 332, 55 (1988).

[5] T. H. Geballe and J. H. Hulm, Science 239, 29-35 (1988).

[6] J. Talvacchio, G. R. Wagner and S. H. Talisa, Microwave Journal, 105-113 (July, 1991).

[7] W. G. Lyons and R. S. Withers, Microwave Journal, November, 85-102 (1990).

[8] N. Newman and W. G. Lyons, J. Supercond. 6, 119-160 (1993).

[9] Jian Mao, Steven M. Anlage, J. L. Peng and R. L. Greene, IEEE Trans. Appl. Supercon. 5, 1997- 2000 (1995).

[10] Jian Mao et al., Phys. Rev. B Rapid Comm. 51, 3316-3319 (1995).

[11] W. N. Hardy et al., Phys. Rev. Lett. 70, 3999-4002 (1993).

[12] G.-C. Liang et al., 1994 IEEE MTT-S Symposium Digest, Vol. 1, 183-186 (1994).

[13] The lowest surface resistance at 77 K, 10 GHz in a YBCO film is about 185 $\mu\Omega$, as measured by A. Lauder, et al., Proc. 5th Intern. Symp. on Superconductivity, edited by Y. Bando and H. Yamauchi (Springer-Verlag, Tokyo, 1993).

[14] W. L. Holstein et al., Appl. Phys. Lett. 60, 2014-2016, 1992.

[15] N. Newman et al., IEEE Trans. Magnetics 27, 1276-1279 (1991).

[16] A. Mogro-Campero et al., Appl. Phys. Lett. 60, 3310-3312 (1992).

[17] George W. Mitschang, IEEE Transactions Appl. Supercond. **5, 69** (1995).

[18] Y. Tokura, H. Takagi and S. Uchida, Nature **337**, 345 (1989).

[19] Wu Jiang et. al., Phys. Rev. Lett. **73**, 1291 (1994).

[20] S. N. Mao et al., Appl. Phys. Lett. **61**, 2356-2358 (1992); D. Prasad Beesabathina et al., J. Mater. Res. **9**, 1376-1383 (1994).

[21] J. L. Peng et al., Mater. Res. Soc. Symp. Proc. **169**, 173 (1990).

[22] Zhengxiang Ma et al., Phys. Rev. Lett. **71**, 781-784 (1993).

[23] L. N. Cooper, Phys. Rev. **104**, 1189 (1956).

[24] J. Bardeen, L. N. Cooper, and J. R. Schrieffer, Phys. Rev. **108**, 1175 (1957).

[25] C. E. Gough, et al, "Flux quantization in a high-T_c superconductor", Nature **326**, 855 (1987).

[26] P. Gammel et al., "Observation of Hexagonally Correlated Flux Quanta In $YBa_2Cu_3O_7$", Phys. Rev. Lett. **59**, 2592-2595 (1987).

[27] Gerald Burns, "An Introduction to High Temperature Superconductivity", Chapter 5, Academic Press, Inc. (1992).

[28] S. E. Barret et al., Phys. Rev. B. **41**, 6283 (1990).

[29] S. E. Barret et al., Phys. Rev. Lett. **66**, 108 (1991).

[30] M. Takigawa et al., Phys. Rev. B **39**, 7371 (1989).

[31] M. R. Beasley, IEEE Trans. Appl. Supercon. **5**, 141 (1995).

[32] Robert F. Service, Research News, Science **265**, 2014(1994).

[33] "In explaining high T_c, is d-wave a washout?", Physics Today, page 11, Feburary (1994).

12

[34] N. E. Bickers, D. J. Scalapino, S. R. White, Phys. Rev. Lett. **62**, 961 (1989).

[35] Bulut, D. J. Scalapino, and S. R. White, Phys. Rev. B **47**, 14 599 (1993).

[36] J. Annett, N. Goldenfeld, and S. R. Renn, Phys. Rev. B **43**, 2778 (1991).

[37] C. C. Tsuei et al., Phys. Rev. Lett. **73**, 593-596 (1994).

[38] D. A. Wohlman et al., Phys. Rev. Lett. **71**, 2134 (1993).

[39] Anna Mathai et al., Phys. Rev. Lett. **74**, 4523 (1995).

[40] Z. X. Shen et al., Phys. Rev. Lett. **70**, 1553 (1993); J. Chem. Solids **54**, 1169 (1993).

[41] Juan Carlos Campuzano et al., APS March Meeting (1995).

[42] P. Chaudhari and Lin, Phys. Rev. Lett. **72**, 1084 (1994).

[43] A. G. Sun, D. A. Gajewski, M. B. Maple, and R. C. Dynes, Phys. Rev. Lett. **72**, 2267 (1994).]

[44] Dong Ho Wu, Jian Mao and Steven M. Anlage, Phys. Rev. Lett. **70**, 85-88 (1993).

CHAPTER 2

MICROWAVE MEASUREMENT SET UP

In this Chapter, I give a brief review of several microwave measurement techniques used for high T_c material characterization. Then I discuss the experimental set-up of a novel cavity perturbation technique which was employed in studying the electrodynamic response of superconductors. This response is traditionally described by a parameter called the surface impedance. The fundamental principles underlying the microwave surface impedance and conductivity measurements by the resonant perturbation technique will be addressed in Chapter 3. Experimental results on the surface impedance of cuprates obtained by this technique will be presented in Chapter 5.

2-1   Introduction

The microwave spectrum ranges from about 900 MHz to about 50 GHz. It overlaps the radio wave and millimeter wave spectra at the low and high end of the spectrum, respectively. As mentioned in Chapter 1, microwave surface impedance characterization is very important for understanding the physics of high T_c superconductivity and developing high T_c microwave applications. Many resonant techniques have been established, including the parallel plate resonator[1-3], the ring resonator[4], the dielectric resonator[5-6], the confocal resonantor[7], the stripline resonator[8] and the endwall replacement cavity.[9] The basic idea behind

14

these techniques is that the sample becomes part of the resonator or an internal load of a cavity, and the electrodynamic properties of the surface can be inferred from the response of the cavity to the induced currents in the sample.

Throughout this work, we employed and greatly refined the hot finger technique, which was first developed by S. Sridhar and W. L. Kennedy[10-11], to study the surface impedance of cuprate materials. The quality factor Q of the superconducting Nb cavity (without sample) has been improved by recrystallizing the Nb surface, so that we have a enhanced $Q \sim 2.5 \times 10^7$ at T = 4.2 K[12]. The improved Q is almost a factor of 5 better than that of reference [11]. The coupling and frequency stability are also improved dramatically by using special electrical ground contact pieces and maintaining a very high vacuum ($<10^{-4}$ torr before cryogenic cooling) in the cavity. The frequency shift of the cavity and sapphire rod without the sample is minimized by a using small c-axis oriented sapphire rod (diameter $\sim$ 1mm). These improvements enable us to do precise measurements of Z_s in small samples. We can measure the surface resistance and change in the surface reactance (change of penetration depth $\Delta\lambda$) simultaneously from low temperatures ($\leq$4.2 K) to temperatures far above the transition temperature (>200 K), with high sensitivity. Also we have some flexibility of field orientations with respect to the sample crystal axes, which may be used to study the anisotropy of the high T_c materials.[13] This technique can also be applied to the measurement of films of any shape and small bulk samples, such as single crystals. Single crystals have less defects than films and hence may be more suitable to study the intrinsic properties of material.

15

2-2 Microwave Measurement Techniques

In this section, I will discuss several techniques which I used for surface impedance characterization in the last few years. All of them are commonly used methods.

Some of these techniques are useful only for R_s measurements, while others permit simultaneous R_s and X_s measurements. The sensitivity, sample preparation requirements and measurement temperature range are different for each method.

2-2.1 Parallel Plate Resonator

One of the commonly used techniques to characterize the surface resistance of high quality superconducting films is the parallel plate resonator (PPR). PPR was developed to measure superconducting films with very low surface resistance [1]. It can also measure the change of the surface reactance and the penetration depth with a high resolution. The schematic view is shown in **Figure 2.1**. A pair of "identical" superconducting films parallel to each other forms a parallel plate resonator. This resonator is usually placed in a copper cavity housing. A dielectric spacer, such as Teflon, separates the two films. Usually capacitive coupling is used to excite the resonance. If the fringing field effect is neglected, a standing wave can form between the two plates. The resonant frequency f_0 in the TEM_{mn} mode for a PPR formed by a pair of rectangular films is

$$f_0(m,n) = \frac{c}{2\sqrt{\varepsilon_r}} \sqrt{(\tfrac{m}{a})^2 + (\tfrac{n}{b})^2} \Big/ \sqrt{1 + \frac{2\lambda}{s}\coth(\tfrac{t}{\lambda})} \qquad (1)$$

16

Parallel Plate Resonator
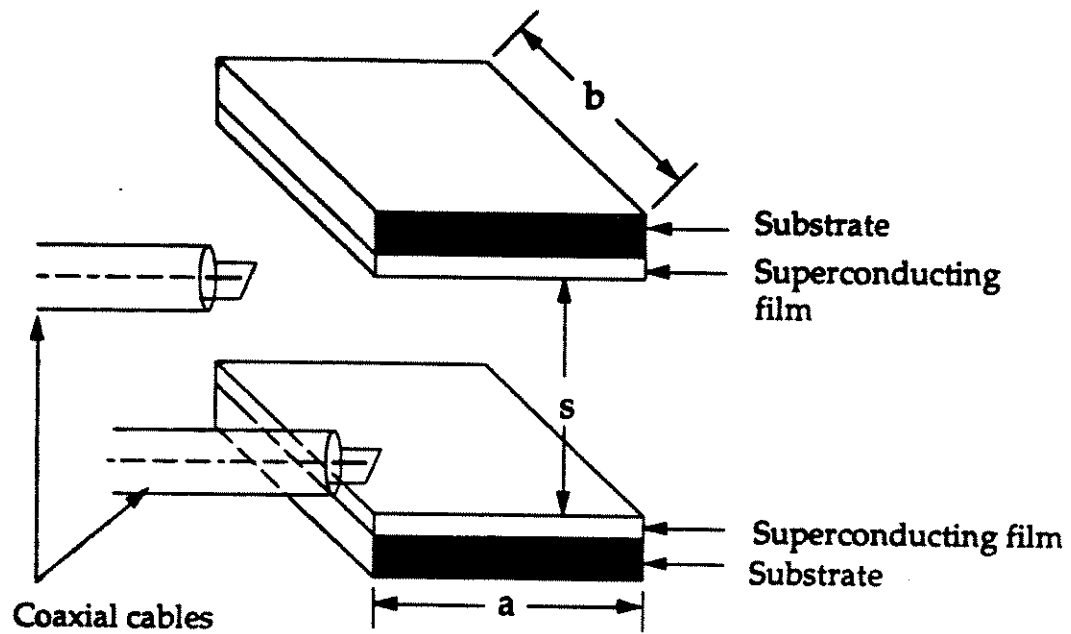
Figure 2.1   Parallel Resonator

where a and b are the dimensions of the film, s is the spacing between the films, λ is the penetration depth and t is the film thickness. The surface resistance R_s is

$$R_s = \frac{\pi \mu_0 f_0 s}{Q_s} \qquad (2)$$

where Q_s is the quality factor due to the superconducting films. The measured Q_0 can be expressed as

$$\frac{1}{Q_0} = \frac{1}{Q_s} + \frac{1}{Q_d} + \frac{1}{Q_r} \qquad (3)$$

where Q_d is due to the loss of the dielectric spacer and Q_r is due to the radiation loss. Q_d is related to the loss tangent $\tan\delta$ of the spacer by

$$\frac{1}{Q_d} = \tan\delta \qquad (4)$$

where $\tan\delta$ for Teflon at low temperatures is less than $10^{-5} \sim 10^{-6}$.

Generally the thicker the spacer, the bigger the radiation loss compared with the loss due to the sample.

The advantage of PPR is that it has a high sensitivity, requires no background subtraction and is nondestructive. Fast dipping measurements can be easily performed. For a Teflon spacer of thickness 12.5 μm, the resolution of R_S is as low as 4 $\mu\Omega$ at 10 GHz. The disadvantages mainly come from the lack of certainty in the spacer thickness and the problem of air gaps between the pair of films. Also the coupling is weak and the resonance dies out when R_S approaches $\sim$ 2 mΩ at 10 GHz (this typically happens near the transition temperature of the sample). For YBCO films, the signal is hard to distinguish from the background noise when the temperature is above 80 K. Thus it is not possible to study the microwave properties through the transition and above T_c. While a thicker spacer increases the coupling strength, the radiation loss tends to increase at the same time and becomes

18

intolerable. Besides these, the mixing of the cavity housing mode and the resonance from the parallel plates sometimes causes the problem of separating them in the measurement.

2-2.2 Confocal Resonator

The confocal resonator is used for measuring R_s at millimeter wave frequencies[7]. A schematic view is given in **Figure 2.2.** The microwave comes through a waveguide on top of the mirror of curvature r and focuses to a spot of size $\sqrt{rc/2\pi f}$. The multiple reflections between the sample surface and the mirror form a resonator. If r >> c/λ, then the radiation loss is small compared with the loss due to the conducting sample and conducting normal metal (usually copper) mirror. The quality factor Q can be expressed as[7]

$$Q = \frac{30\pi^4 r^3 f^3}{c^3[R_{s-sample}(0.5k^2 r^2 + kr) + 0.375k^2 r^2 R_{s-mirror}]} \qquad (5)$$

where $R_{s-sample}$ and $R_{s-mirror}$ (in ohms per square) are the surface resistance of the superconducting sample and the normal metal of the inner surface of the mirror respectively, and $k = 2\pi f / c$. With the calibration of $R_{s-mirror}$, the $R_{s-sample}$ can be calculated from the measured Q by Eq. (5). At higher frequencies, the beam spot size becomes smaller and the first term of the denominator in Eq. (5) becomes larger compared with the second term.

The sensitivity is about 1 mΩ at 36 GHz at 77 K.[7] This method is convenient and is good for fast scanning of the film surface because the beam can be focused at a small spot on the surface of the sample. Contour mapping of the R_S on the surface of the sample is possible. It also requires no sample preparation and is nondestructive. The disadvantage is that the sensitivity is

Confocal Resonator
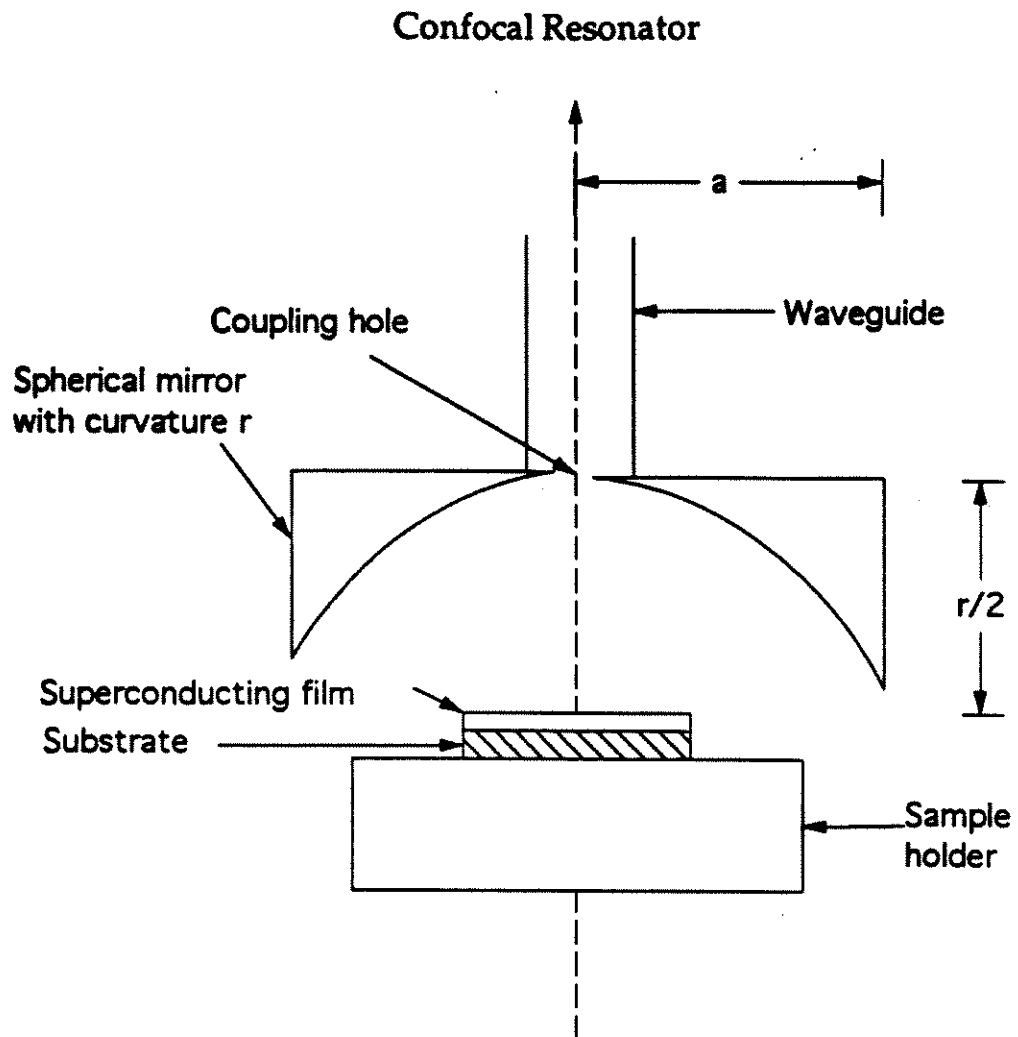
Figure 2.2   Confocal Resonator.

20

low and accuracy is moderate. Also it operates only at one (liquid nitrogen) temperature.

2-2.3   Dielectric Resonator

The dielectric resonator provides a convenient way to measure the surface resistance of films of relatively large size (up to a few inches). Figure 2.3 shows a schematic view of the experimental configuration. The dielectric resonator is confined in a copper housing. The resonator itself is formed by a dielectric cylinder with a high dielectric constant and very low loss, and two superconducting films on the top and the bottom of the cylinder. The resonator normally is operated in the TE_{011} mode. The RF fields are concentrated around the dielectric cylinder because of its high dielectric constant. The surface resistance can be obtained by measuring the quality factor Q

$$R_s = G / Q_c \tag{6}$$

where G is a geometry factor which can be calculated. The calculation can be found in reference [14]. The reported sensitivity by C. Wilker et al. [15] is ~ 50 $\mu\Omega$ at 27.5 GHz.

The disadvantage of this technique is that it is hard to measure the surface reactance X_s and the data analysis is quite complicated.

2-3   Hot Finger Microwave Cavity Technique

Among all the microwave characterization techniques, the hot finger microwave cavity technique uniquely provides very high sensitivity and

21

Dielectric Resonator
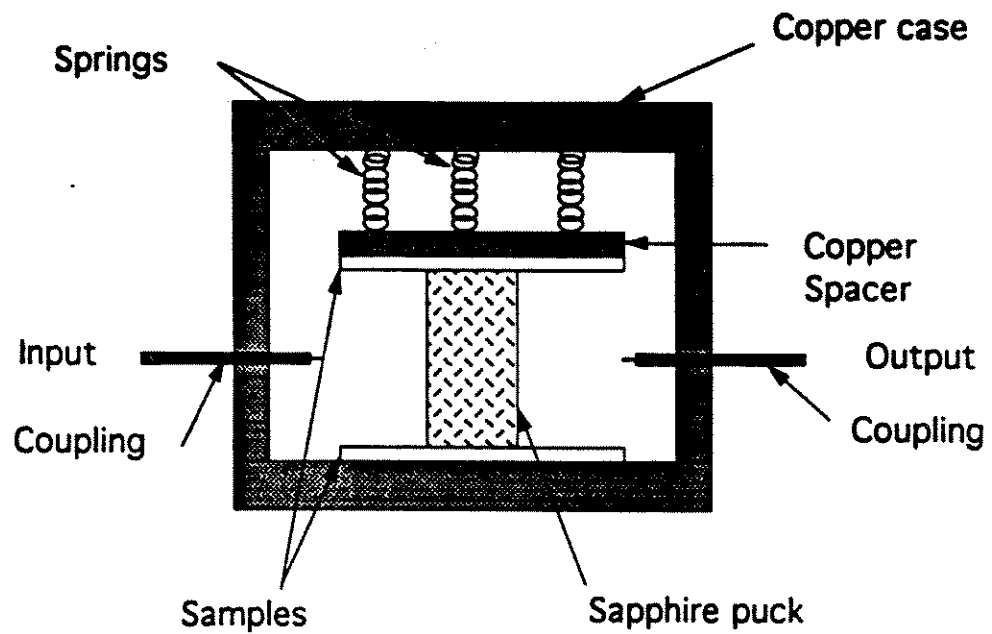
Figure 2.3   Dielectric Resonator

simultaneous measurements of R_s and X_s. We will discuss this technique in detail in this section.

2-3.1 Calculation of Modes In A Cylindrical Cavity

Following any standard textbook on electrodynamics, we can calculate the normal modes in a cylindrical cavity[16]. The cylinder is shown in **Figure 2.4**, with inner radius R and length L. With a sinusoidal time dependence $e^{-i\omega t}$ for the fields inside the cavity, Maxwell's equations take the form,

$$\nabla \times E = i\omega B \qquad \nabla \times B = -i\frac{\omega}{c^2}E \tag{7}$$

$$\nabla \cdot E = 0 \qquad \nabla \cdot B = 0 \tag{8}$$

where it is assumed that the cavity is in vacuum with dielectric constant ε_0 and permeability μ_0. The boundary conditions are

$$n \times E = 0, \qquad n \cdot B = 0 \tag{9}$$

where n is a unit normal at the surface S. In words, the magnetic field H can have no component normal to a perfect conductor, and the electric field E can have no component parallel.

Because of the cylindrical geometry, it is useful to single out the spatial variation of the fields in the z direction and assume

$$\left.\begin{matrix} E(x,y,z,t) \\ E(x,y,z,t) \end{matrix}\right\} = \begin{cases} E(x,y)e^{\pm ikz-i\omega t} \\ B(x,y)e^{\pm ikz-i\omega t} \end{cases} \tag{10}$$

With this assumed z dependence of the fields, the wave equation reduces to the two-dimensional form:

$$\nabla_t^2 + (\omega^2 - k^2)\begin{Bmatrix} E \\ B \end{Bmatrix} = 0 \tag{11}$$

where ∇_t^2 is the transverse part of the Laplacian operator:

$$\nabla_t^2 = \nabla^2 - \frac{\partial^2}{\partial z^2} \tag{12}$$

23
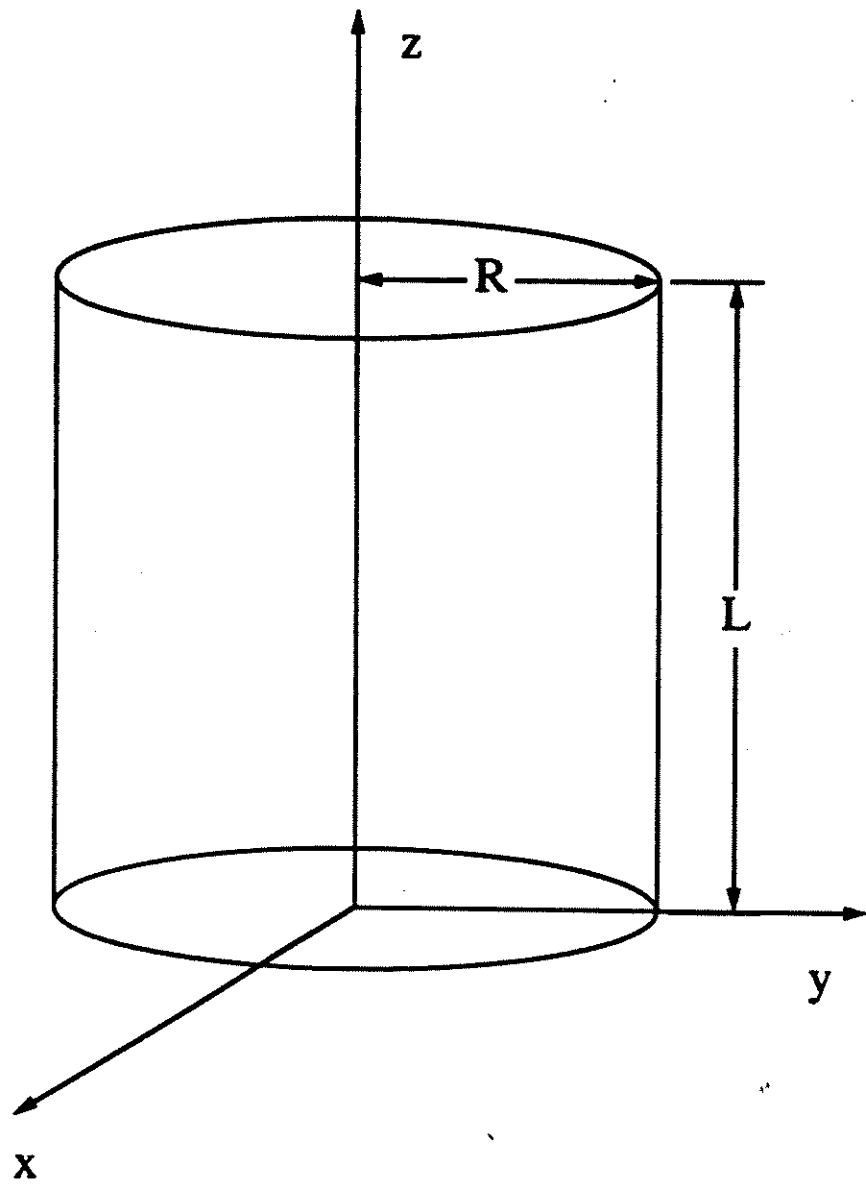
Figure 2.4   A cylindrical cavity.

It is useful to separate the fields into components parallel to and transverse to the z axis:

$$E = E_z + E_t \tag{13}$$

where
$$E_z = e_3 E_z$$
$$E_t = (e_3 \times E) \times e_3 \tag{14}$$

and e_3 is a unit vector in the z direction. Similar definitions hold for the magnetic field B.

The general solutions are

TE fields
$$\begin{cases} E_t = -\dfrac{i\omega\mu_0}{c\gamma^2}\sin(\dfrac{p\pi z}{L})\hat{e}_3 \times \nabla_t \psi \\[4mm] H_t = \dfrac{p\pi}{L\gamma^2}\cos(\dfrac{p\pi z}{L})\nabla_t \psi \end{cases} \tag{15}$$

TM fields
$$\begin{cases} E_t = \dfrac{i\omega\varepsilon_0}{c\gamma^2}\cos(\dfrac{p\pi z}{L})\hat{e}_3 \times \nabla_t \psi \\[4mm] H_t = -\dfrac{p\pi}{L\gamma^2}\sin(\dfrac{p\pi z}{L})\nabla_t \psi \end{cases} \tag{16}$$

where $\psi e^{\pm ikz}$ is the $E_z (H_z)$ for TM (TE) waves and the constant γ^2 is

$$\gamma^2 = \omega^2 - (\frac{p\pi}{L})^2. \tag{17}$$

For each value of p the eigenvalue γ_κ^2 determines an eigen frequency $\omega_{\kappa p}$:

$$\omega_{\kappa p}^2 = \gamma_\kappa^2 + (\frac{p\pi}{L})^2 \tag{18}$$

and the corresponding fields of that resonant mode. Transverse electric (TE) waves are defined as $E_z=0$ everywhere with boundary condition, $\dfrac{\partial B_t}{\partial n}\bigg|_{u} = 0$;

Transverse magnetic (TM) waves are defined as $B_z=0$ everywhere with boundary conditions $E_t\big|_u = 0$. The various TE and TM waves constitute a complete set of fields to describe an arbitrary electromagnetic disturbance in a waveguide or cavity.

25

For a cylindrical resonant cavity, using polar coordinates, $\psi(\rho,\phi)$ satisfies the two dimensional wave equation

$$(\nabla_t^2 + \gamma^2)\psi(\rho,\phi) = 0 \tag{18}$$

or

$$(\frac{\partial^2}{\partial\rho^2} + \frac{1}{\rho}\frac{\partial}{\partial\rho} + \frac{1}{\rho^2}\frac{\partial^2}{\partial\phi^2} + \gamma^2)\psi(\rho,\phi) = 0 \tag{19}$$

If we separate the variable with $\psi(\rho,\phi) = R(\rho)\Phi(\phi)$, the solutions are

$$\psi(\rho,\phi) = \left.\begin{matrix} E_0 \\ H_0 \end{matrix}\right\} J_m(\gamma_{mn}\rho)e^{\pm im\phi} \tag{20}$$

for $\left.\begin{matrix} TM \\ TE \end{matrix}\right\}$ modes.

Consideration of the boundary conditions yields γ expressed in terms of the zeros of the Bessel functions:

TE: $\left.\dfrac{\partial H_z}{\partial\rho}\right|_{\rho=R} = 0$ makes $\dfrac{\partial J_m(\gamma_{mn}R)}{\partial\rho} = 0$, hence

$$\gamma_{mn} = \frac{x'_{mn}}{R} \tag{21}$$

where x'_{mn} is the nth root of $J'_m(x) = 0$.

TM: $\left.E_z\right|_{\rho=R} = 0$ makes $J_m(\gamma_{mn}R) = 0$, hence

$$\gamma_{mn} = \frac{x_{mn}}{R} \tag{22}$$

where x_{mn} is the nth root of $J_m(x) = 0$.

The resonant frequencies are given by

$$\omega_{mnp} = c\sqrt{\frac{x'^2_{mn}}{R^2} + \frac{p^2\pi^2}{L^2}} \tag{23}$$

for TE modes, and

$$\omega_{mnp} = c\sqrt{\frac{x^2_{mn}}{R^2} + \frac{p^2\pi^2}{L^2}} \tag{24}$$

for TM modes.
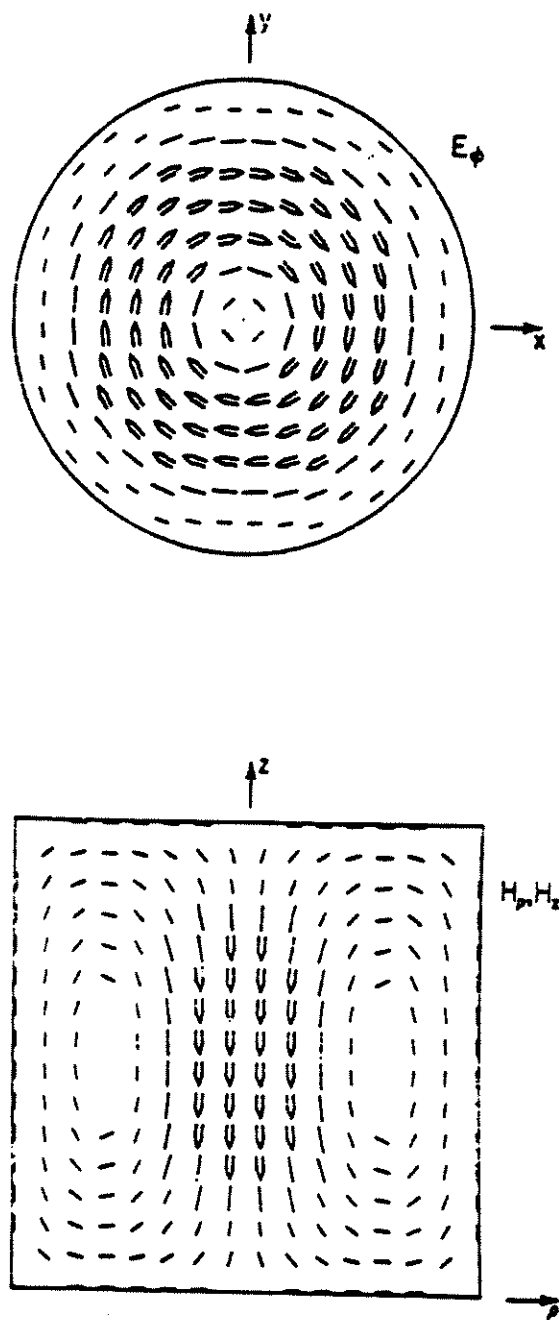
Figure 2.5 Field configuration in the TE$_{011}$ mode: (a) Electric field in the equatorial plane; (b) Magnetic field in the meridian plane.

27

For the TE_{011} mode, the fields configurations are shown in **Figure 2.5** and can be expressed as

$$E_{TE_{011}}(r,z) = \hat{\phi}\mu_0 c H_0 \sqrt{(\frac{\pi R}{x_{01}L})^2 + 1}\, J_1(x_{01}'\frac{r}{R})\sin(\pi\frac{z}{L}) \qquad (25)$$

$$H_{TE_{011}}(r,z) = H_0[-\hat{r}(\frac{\pi R}{x_{01}L})^2 J_1(x_{01}'\frac{r}{R})\cos(\pi\frac{z}{L}) + \hat{z}J_0(x_{01}'\frac{r}{R})\sin(\pi\frac{z}{L})] \qquad (26)$$

When a small sample is introduced into a resonant cavity, the resonance response (the resonant frequency and bandwidth of the resonance) is changed by a small amount. The relation between the response of the resonance and the properties of the sample can be derived by perturbation theory and is explained in great detail in Chapter 3.

2-3.2   Cavity Fabrication

A Nb cavity was made of bulk high purity Nb pieces obtained from Peter Kneisel at CEBAF (Newport News, VA) and was fabricated in house. The surface was mechanically polished, and sent to CEBAF to be recrystallized under ultra high vacuum and high temperature. [12] This resulted in an increase in the quality factor Q by a factor of at least two. The cavity is cylindrical with inner dimensions 1.625" diameter and 1.617" long and was designed to be operated at 9.6 GHz in the TE_{011} mode.

2-3.3   General Consideration for the Hot-Finger Probe Design

Figure 2.6 is a schematic drawing of the probe. It is placed in a 50" dewar with a diameter of 5"[17] for the measurement. The inner space of the probe, which includes the space inside the Nb cavity, the bottom sample supporting assembly, and the tubes for holding the coaxial cables and pumping the vacuum, are maintained in high vacuum. The probe part

28

Superconducting Nb Cavity Resonator
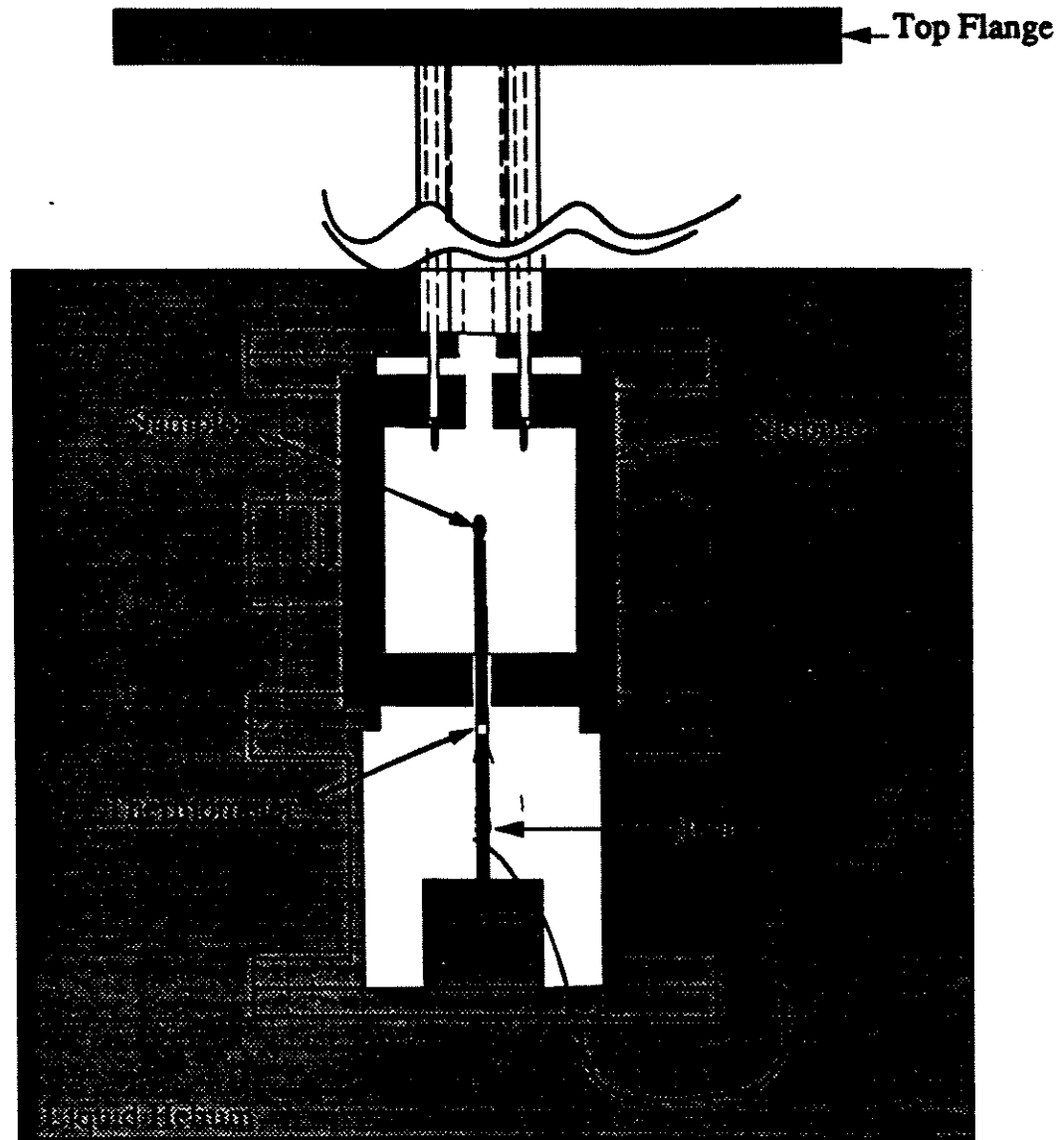
Top Flange

Figure 2.6   A schematic drawing of the hot finger probe used for

microwave characterization of material (not drawn to scale).

below the top flange (See **Figure 2.6**) is maintained inside the liquid helium, so that the cavity temperature stays at liquid helium temperature of 4.2 K. Occasionally, when we would like to go below 4.2 K, the helium bath can be pumped.

It is critical to keep the cavity in a very high vacuum in order to achieve reliable results, as the variation of resonant frequency is particularly sensitive to the quality of the vacuum. Existing gas may cause random fluctuation of the resonant frequency. The sample is mounted on the top of a sapphire rod and is placed at the center of the cavity. The sapphire rod has a very low microwave loss and a very high thermal conductivity. The bottom pedestal, which holds the sapphire rod upright, is made of thin wall stainless steel with low thermal conductivity. A calibrated Si-diode thermometer from Lakeshore is attached to a flat surface cut by a diamond wheel on the sapphire rod with a thin layer of GE varnish between them. With a heater made of Chromel-Constantan wires mounted on the rod, the sample temperature can be easily varied between 4.2 K and 250 K (or even higher) using a LakeShore DRC-93CA temperature controller.

For most of the perturbation techniques, the sample is placed at a region of either maximum magnetic H or electric E field. When one field is zero (minimum), the other is at a maximum. The fields may be taken as uniform over a limited range. The TE_{011} mode offers several advantages to study the properties of a sample. The configuration of fields is shown in **Figure 2.5**. In the TE mode the currents in the walls of the cavity are azimuthal, while in TM modes the currents are induced along the cylindrical axis and need to pass the corners between the cylindrical piece and

30

top or bottom piece. These later currents will cause much more loss. To keep the symmetry of the field configuration along the z-axis, e.g. no dependence on the azimuthal angle (m=0), and to have the highest sensitivity (e.g. highest Q), the TE_{011} mode is chosen among TE_{mnp} modes. From Eqs. (25) and (26), one can see that the magnetic field is at maximum and is reasonably uniform at the center of the cavity. Also the electric field is almost zero at the center of cavity for a single crystal sample of typical size 1 mm x 2 mm, which is less than 5% of the cavity dimension. This allows one to treat the rf magnetic field over the sample surface as a uniform field and ignore the E field. Hence it is valid to treat the sample as a perturbation. (See Chapter 3) When the sample dimensions become comparable with the dimensions of a cavity operating at higher frequencies, the straightforward perturbation treatment will not be valid and one may need to find an alternative method.

The block diagram of the measurement system is shown in **Figure 2.7**. A HP-8510C network analyzer system is used as the microwave power source and detector. It has three components: HP-83651A (45 MHz - 50 GHz) synthesizer sweeper, HP-8517A (45 MHz - 50 GHz) S-parameter test set, and a 8510C network analyzer. The source power from the synthesizer ranges from -17 dbm to 17 dbm, and the signal is attenuated when coming out of the ports of the S-parameter test sets. The attenuation depends on frequency and is about 8 dbm at 10 GHz between the source (HP-83651A) and the output ports of the HP-8517A S-parameter test sets. The system has a frequency resolution of 1 Hz. A LakeShore temperature controller controls the temperature of the sample. All the instruments are controlled by a personal computer (IBM PC

31

Measurement System
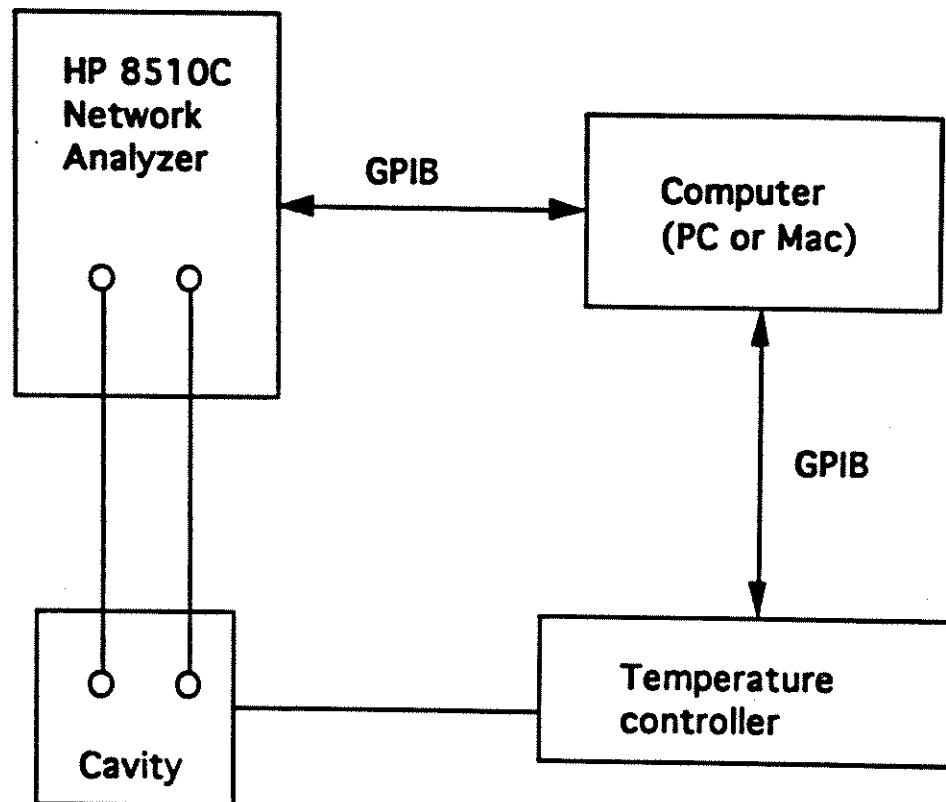
Figure 2.7   A schematic of the measurement system.

or Macintosh) through a standard IEEE 488 GPIB card. Data are saved as a text-file and can be analyzed by either IBM PC or Macintosh computers.

2-3.4 Mode Excitation and Isolation

Coaxial cables are used to transmit the microwaves. The coaxial cable is a 50 Ω semi-rigid type with the outer diameter of 0.086 inches. In our system, the type A cables, which are mainly inside the dewar during the experiment, have a stainless steel shell. The type B cables, connecting the ports of network analyzer and the type A cables coming out the top flange of the probe, have a copper shell and are maintained at room temperature during the experiment. The cables are vacuum sealed by rubber O-rings when they come out of the top flange of the probe so that the inner space remains in a high vacuum. By reducing the thermal (cold) transfer to the top of the probe from the lower parts immersed in liquid helium, it takes less effort to seal the vacuum properly and reduces the risk of breaking the rubber O-ring seal. The O-ring tends to become fragile when it is cold, and motion of the cable may break the O-ring. Hence minimizing the thermal transfer by using stainless steel coax helps to seal the vacuum. The insulator between inner and outer conductors of the cable is Teflon.

To feed the microwave signal, and to pick up the output signal from the cavity, two small coupling holes were drilled onto the top piece of the cavity. The coupling holes are made at the location where the rf magnetic field strength is maximum, as determined from Eq. (26). The microwave transmission through the coaxial cables is magnetically (inductively) coupled into the cavity through a loop at the end of the cables. The center pin of the

33

coaxial cable sticks out and makes an electrical contact with the outer shell (by soldering) and hence forms a small loop antenna. To optimize the coupling, we need to adjust the antenna position in the z-direction while the antenna maintains good electrical contact with the cavity. To accomplish this, we made ground contact pieces for both input and output antennae. Precise adjustment of the coupling was made by installing micrometers on the top of the probe flange for both antennae. The coupling is precisely adjusted by pulling out or pushing in the coaxial lines through the wave guide hole on the top piece of the cavity. A third hole at the center of the bottom piece of the cavity is to let the sapphire rod into the cavity. The size of this hole is chosen to be fairly bigger than the rod to avoid any possible physical contact or serious thermal conduction (through residual gas) or radiation between the rod and the cavity. The fourth hole is located at the center of the top piece to allow evacuation of the cavity. All the holes essentially act like cylindrical waveguides, hence their sizes are limited by the requirement of being small enough to have cut-off frequencies well above the resonant frequency of the cavity. The two coupling holes have a diameter about 0.09", which are very small compared with the radius of the cavity. The two center holes have a radius less than 5 mm and are also much less than the radius of the cavity. The center holes are located at the place of minimum fields at TE_{011} mode of the cavity. Therefore these holes minimally affect the cavity TE_{011} mode.

From Eq. (24), and because $x_{01} = x_{11} = 3.832\cdots$, the resonant frequency $\omega_{TE_{011}} = \omega_{TM_{111}}$. Hence the TE_{011} mode and TM_{111} modes are degenerate. It is important to separate these two modes, because the TM_{111} mode causes more

loss and hence yields effectively a much lower quality factor Q. Therefore, a mode trap, which is a deformation of the surface, has to be set up. This can be achieved, for instance by cutting a groove half way between the top and the bottom walls on the cylindrical cavity. However, the four holes on the top and bottom cavity pieces already serve the purpose and lift the degeneracy between these two modes.[18][20] It was found that the TE_{011} mode is more than 20 MHz above the TM_{111} mode.

2-3.5 Sample and Sapphire Rod Supporting Assembly

The probe is designed to place the sample at the center of the cavity where the magnetic field of the TE_{011} mode is parallel to the z-axis (**Figure 2.4**). This requires the sapphire rod to sit upright, aligned strictly along the z-axis. The sapphire rod used is 3 mm diameter for films or 1 mm for single crystal samples, and is placed into the cavity through the hole on the bottom piece of the Nb cavity.

The sample and sapphire rod supporting assembly are composed of several pieces shown in **Figure 2.8**, and are kept in vacuum during measurements. The materials are chosen to satisfy the following requirements: there should be enough thermal conduction to cool the sample down to the helium bath temperature (there is almost no heat transfer through convection because of the very high vacuum inside the cavity) while the pedestal provides enough thermal insulation to easily heat up the sample and maintain it at a temperature up to 200 K. We choose thin-wall stainless steel tube to support the rod and mount them on a bulk

Sample Supporting Assembly

sapphire rod

epoxied together

thin wall stainless steel tube

soldered together

extension of the tube

tighten together by screws

screws

pedestal

Material: stainless steel
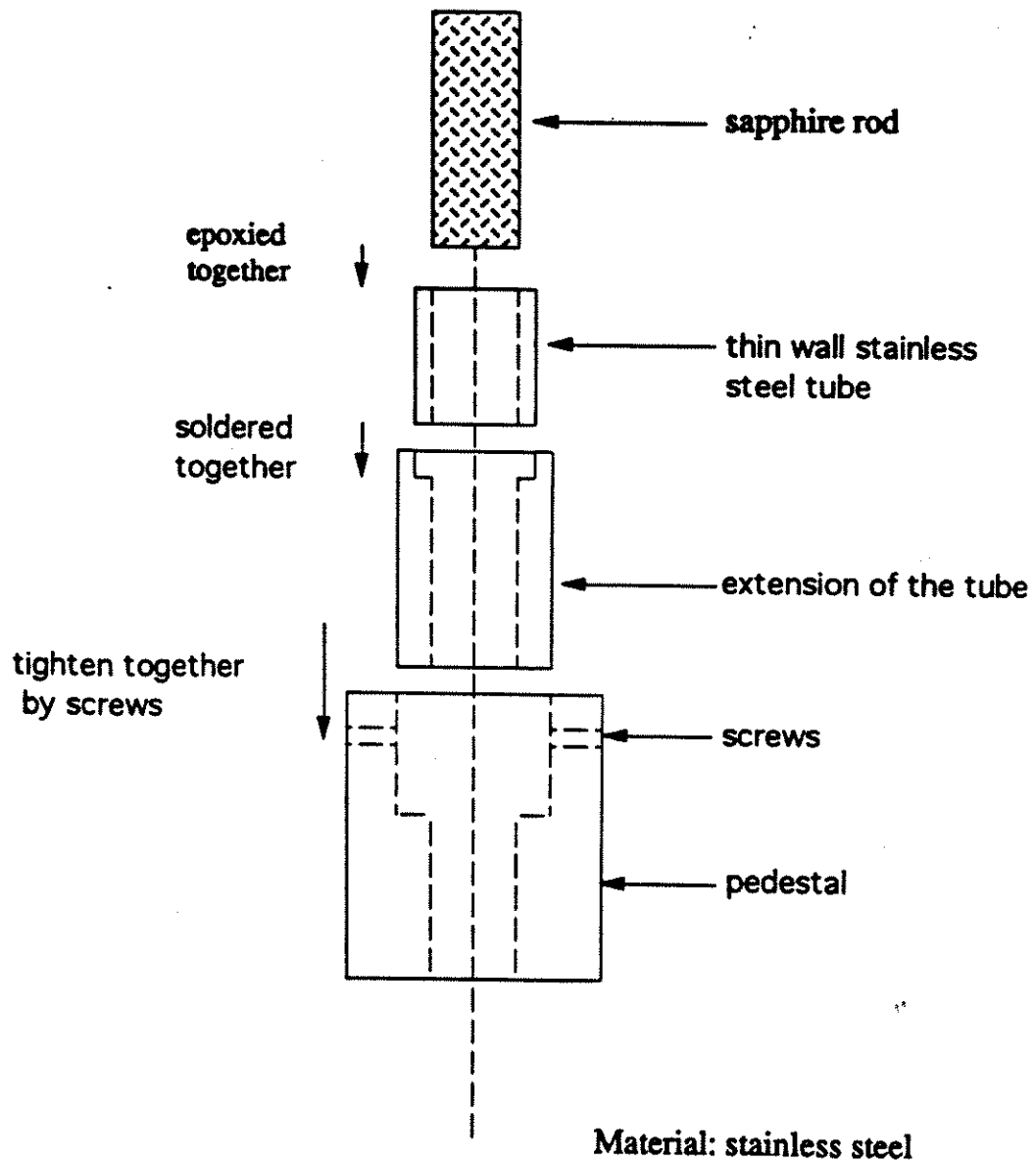
Figure 2.8   A schematic of the sample supporting assembly. A sapphire rod fits into a thin wall stainless steel tube snugly. An extension piece for the tube, which is mounted on a stainless pedestal, also serves to support the rod.

36

stainless steel pedestal which silver-soldered onto the bottom piece of the probe.

2-3.6 High Vacuum

The Nb cavity pieces are clamped together by several stainless steel pieces. The screws used are made of titanium, which has a similar thermal expansion coefficient as that of the niobium. Indium O-rings are placed on the O-ring grooves. Screws for flanges are about one for every 3/4" of perimeter. We drilled eight screw holes on the flanges. In order to avoid stress distortion, the thickness of the flanges is from 1/4" to 1/2", depending on the size of the flanges. To obtain high vacuum, welding, hard soldering (silver soldering) were used to joining tubes to flanges and plates. Chapter 3 of Reference[21] gives a detailed discussion on these cryogenic design conventions.

It has been our experience that the ultra-torr fitting seals for coaxial cables coming out of the vacuum of the cavity, and the hermetic seal for letting electrical wires come out of the cavity, tend to be the best candidates for a vacuum leak. Thus, before each experiment, it is necessary to make sure the rubber O-rings in the ultra-torr fittings are in good condition. Also high vacuum sealant-resin made by the Space Environment Laboratories are used to seal the possible leaks on the hermetic seal. With this care, a vacuum of better than 10^{-5} torr can be achieved, and can be maintained at low temperatures.

The importance of very high vacuum can not be over-emphasized for this type of measurement. High vacuum not only helps to thermally isolate

the sapphire rod and the sample from cavity walls, but also helps to measure the resonant frequency reliably and reproducibly. Because even a very small amount of helium gas can result in a significant fluctuation of the resonant frequency.

2-3.7 Thermal Aspects of Design and Performance

The thermal characteristics of the sample mounting assembly and heat radiation loss are determined by parameters, such as the spatial separation of the sample and the sensing thermometer, the thermal time constant of the assembly, and the thermal radiation.[11]

As shown in **Figure 2.6**, the diode temperature sensor and the heater are mounted on the sapphire rod, staying outside the cavity. Taking into account the thermal conduction and radiation losses of the sapphire and sample, we can estimate the temperature difference between the sample temperature T and the measured temperature T_m (i.e. sensor temperature) by

$$T_m - T \cong \frac{\sigma_{sb}}{K_s} l[1 + \frac{2}{a}(l + t)] T_m^4 \qquad (27)$$

where σ_{sb} is the Stefan-Boltzman constant, K_s the thermal conductivity of sapphire, a is the radius of the rod, l is the length between the sample and the diode sensor along the sapphire rod, and t is the thickness of the sample. In this simple calculation, we assume a uniform thermal gradient along the rod, taking into account radiation loss in vacuum (assuming the emissivity of all materials to be unity), and neglect the losses from the rod/sample interface and thermal gradient across the sample. For a nominal rod of dimensions l = 2.2 cm, a = 1.0 mm, t ≈ 10 μm - 1 mm, and thermal conductivity K_s = 60 W cm^{-1} K^{-1}, the estimate of the temperature correction

is ~ 0.65 mK at 100 K. This temperature correction is negligible. It is due to the excellent thermal conductivity of the sapphire.

Experimentally we have observed that the temperature control by a standard equipment such as the LakeShore DRC-93CA controller is fairly responsive: temperature reaches the set point in a very short time and remains stable. The maximum power output for a 25 Ω heater wire from the temperature controller is about 25 W, and 1/10 th of it is sufficient to heat the sample to 250 K.

2-3.8 Transmission Measurement

A Network Analyzer HP 8510C system is used to measure the S-parameters between port 1 and port 2. From the S-parameters, the quality factor Q and the resonant frequency f of the cavity are extracted. The block diagram of the measurement system is shown in **Figure 2.7**.

Figure 2.9 shows a typical trace of transmission coefficient S_{21} around the resonant frequency. The frequency dependence of S_{21} is expected to be

$$S_{21}(\omega) = \frac{1}{\sqrt{2\pi}} \int_0^\infty S_{21,0} e^{-\omega_0 t/2Q} e^{i(\omega-\omega')t} dt \tag{28}$$

where $S_{21,0}$ is a normalization factor. The integral in Eq. (28) leads to a frequency distribution for the energy in the cavity having a resonant shape:

$$|S_{21}(\omega)|^2 \propto \frac{1}{(\omega-\omega')^2 + (\omega_0/2Q)^2} \tag{29}$$

Or more precisely, we can take account of both the magnitude and the phase information, which can be easily measured using the HP8510C Network Analyzer system. The trace of the S_{21} is

$$S_{21}(\omega) \propto \frac{1}{\frac{1}{2Q} + i\frac{\omega-\omega'}{\omega_0}} \tag{30}$$

39

Maryland Superconductivity Center
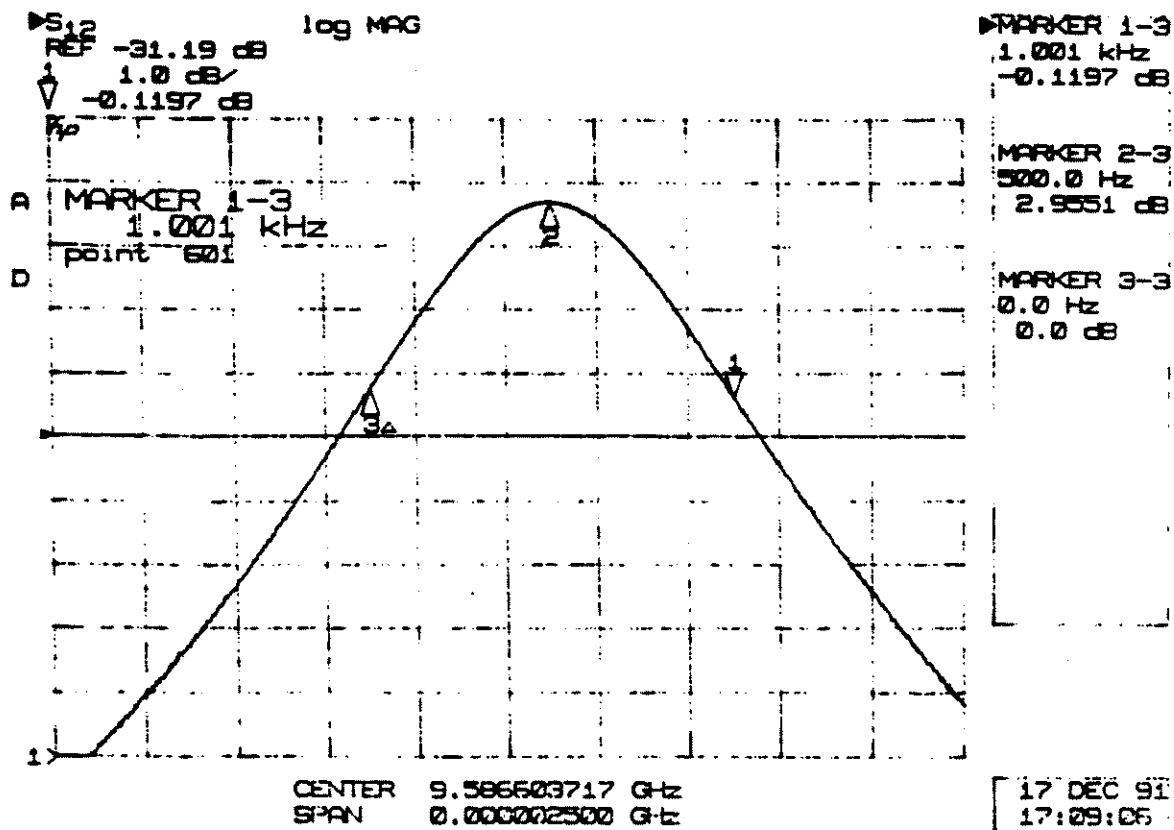
Figure 2.9   A trace of transimision coefficient S_{21}.

By measuring the $S_{21}(\omega)$ at different frequencies around the resonance, we can obtain Q and ω'. This Q gives the value of loaded Q_L, which includes the loss of the cavity itself and the coupling losses. In order to obtain the unloaded Q_{unload}, we need to know the coupling parameter β, which is a measure of the efficiency with which the energy stored in the cavity coupling system is coupled to the external load. There are three different cases. If $\beta < 1$, the cavity is said to be under-coupled; if $\beta = 1$, the cavity is said to be critically coupled; if $\beta > 1$, the cavity is said to be over-coupled. Let us first consider the input coupling loop, labeled as port 1. The relation between the unloaded quality factor Q_{unload} and the loaded quality factor Q_L is[22]

$$Q_{unload} = Q_L \frac{1 + |S_{11,on}|}{1 + |S_{11,off}|} \tag{31}$$

where $S_{11,on}$ is the magnitude of the reflection coefficient on resonance and $S_{11,off}$ is the magnitude of the reflection coefficient off resonance. Eq. (31) can be rewritten as

$$Q_{unload} = Q_L \left(1 + \frac{S_{11,on} - S_{11,off}}{S_{11,on}} \right) = Q_L (1 + \beta_1) \tag{32}$$

Hence

$$\beta_1 = \frac{|S_{11,off}| - |S_{11,on}|}{|S_{11,off}| + |S_{11,on}|} \tag{33}$$

For the pick up loop (port 2), the coupling parameter β_2 can be obtained similarly by

$$\beta_2 = \frac{|S_{22,off}| - |S_{22,on}|}{|S_{22,off}| + |S_{22,on}|} \tag{34}$$

where S_{22} is the reflection coefficient at port 2. Therefore, the unloaded Q can be obtained by

$$Q_{unload} = Q_L (1 + \beta_1 + \beta_2) \tag{35}$$

41

Measurements are done at weak coupling with coupling parameters β_1 and β_2 less than 1% ~ 2%. It sets the upper limit of the measurement error for $Q_{unloaded}$.

2-4 Summary

In conclusion, we discussed several commonly used microwave characterization techniques for high T_c superconductors. The hot finger technique is believed to be an effective, unique technique which provides very high sensitivity and simultaneous measurement of surface resistance R_s and surface reactance X_s. We have thoroughly discussed the design and fabrication of the measurement system based on the hot finger technique.

REFERENCES

[1]   R. C. Taber, Rev. Sci. Instrum. **61**, 2200 (1990).

[2]   Zhengxiang Ma et al., Phys. Rev. Lett. **71**, 781 (1993).

[3]   Michael S. Pambianchi, Jian Mao and S. M. Anlage, Phys. Rev. B **50**, 13659 (1994).

[4]   W. N. Hardy and L. A. Whitehead, Rev. Sci. Instrum. **52**, 213-216 (1981).

[5]   S. J. Fiedziuszko and P. D. Heidmann, 1989 IEEE MTT-S Int. Microwave Symp. Digest **2**, 555-558(1989).

[6]   Z. Y. Shen., et al., 1992 IEEE IEEE MTT-S Int. Microwave Symp. Digest **1**, 193-196 (1992).

[7]   J. S. Martens et al., Appl. Phys. Lett. **58**, 2543-2545 (1991).

[8]   D. E. Oates, A. C. Anderson and P. M. Mankiewich, J. Supercond. **3**, 251-259 (1990).

[9]   L. Drebeck et al., J. Supercond. **3**, 317-321(1990).

[10]   Sridhar et al., Phys. Rev. Lett. **63**, 1873 (1989).

[11]   William Kennedy, Ph. D thesis, Northeastern University (1990).

[12]   We wish to acknowledge Dr. Peter Kneisel at CEBAF for donating the niobium starting material and for the heat treatment of the machined parts.

[13]   Jian Mao et al., Phys. Rev. B Rapid Communication **51**, 3316 (1995).

[14]   Zhi-Yuan Shen, "High-Temperature Superconducting Microwave Circuits", Chapter 7, Artech House, Inc. (1994).

[15]   C. Wilker et al., 1992 IEEE MTT-S Int. Microwave Symp. Digest **1**, 193-196 (1992).

[16] J. D. Jackson, Classical Electrodynamics, second edition, John Wiley & Sons (1975).

[17] Kadel Engineering, Main Street, Danville, Indiana 46122.

[18] Slater's theorem[19] gives

$$\omega^2 - \omega_0^2 = 4\omega_0^2 \frac{\int_{\Delta V}(\mu_0 H^2 - \varepsilon_0 E^2)dV}{\frac{1}{4}\int_{V}(\mu_0 H^2 + \varepsilon_0 E^2)dV}$$

where ω_0 is the unperturbed resonant frequency and $\omega - \omega_0$ is the change of the resonant frequency when the resonator volume changes by ΔV. The upper integral is evaluated over the perturbed volume, and the lower integral gives total energy contained in the resonator. For different modes, the resonant frequency changes differently because the fields at the perturbed volume are different for each mode.

[19] J. C. Slater, "Microwave Transimission", McGraw-Hill book Company, New York (1942).

[20] The real part of Eq. (A1.9) in Appendix 1 of next Chapter.

[21] Robert C. Richardson and Eric N. Smith, "Experimental Techniques in Condensed Matter Physics at Low Temperatures", Addison-Wesley, Inc. (1988).

[22] M. Sucher and J. Fox, Handbook of Microwave Measurements, Third Edition, Vol. II, John Wiley & Sons, Inc. (1963).

CHAPTER 3

THEORY OF SURFACE IMPEDANCE OF SUPERCONDUCTORS IN A RESONANT CAVITY

In this Chapter, we present a simple theory to describe surface impedance of superconductors in a resonant cavity. It is important because this provides the theoretical foundation for understanding how to apply the microwave perturbation measurement techniques to study the electrodynamics of superconductors. We first consider the fundamental principles underlying microwave surface impedance and conductivity measurements by the resonant cavity perturbation technique, and then perform a first principles calculation relating the measured quality factor and resonant frequency to the Poynting vector integrated over the superconducting sample surface. We also treat the case of anisotropic crystals at finite frequencies and include losses due to normal currents. A two-fluid constitutive equation is used for the superconductor, although the main results of the paper are independent of this assumption. A detailed calculation is given for the hot finger cavity perturbation technique. Data on a high quality single crystal of YBCO is used to illustrate the method, and the effective surface impedance of a thin film superconductor is also considered.

3-1   Introduction

Since the discovery of high temperature superconductors, there has been much work on the microwave characterization of cuprate materials and devices. Microwave surface impedance measurements can provide essential information in the study of mechanisms of high T_c superconductors, as well as for the design and fabrication of microwave devices. One of the most effective techniques of microwave characterization is the cavity perturbation technique. While a great number of papers have been published about these measurements, there is still confusion over the definition of the surface impedance Z_s of a superconductor, its connection with quantities that can be experimentally measured, such as quality factor Q and resonant frequency f_{res} of a cavity, and quantities which bear important physical information, such as the magnetic penetration depth and conductivity.[1-2] A detailed derivation of the perturbation formula from first principles for the complex frequency shift of a cavity perturbed by a superconducting sample is given in this Chapter. These results are of great generality, applying to cavity end-plate replacement measurements[3], dielectric resonators[4] and other forms of cavity perturbation.[5-8] Later in this paper, we use the "hot finger" technique[1-2][7-9] as a specific example of cavity perturbation.

It is important and necessary to make clear what assumptions are made in order to understand the physical meaning of Z_s of a superconductor at finite frequency. A great deal of early work on cavity perturbation was done on dielectrics, and ferrites in particular. Hence it is not surprising that some formulas dealing with ferrites or dielectric materials[10][11] have been mistakenly applied to superconductors.[9]

46

There are two ways to look at a superconductor in a magnetic field. One way is to consider a superconductor as a material with permeability μ_0 and dielectric constant ε_0 carrying an induced supercurrent J, which produces a magnetic field to cancel the applied field H_0 inside the superconductor, such that $B = \mu_0 H = 0$ inside the material (Meissner effect). This view shall be designated as method I. The second view is that a superconductor will be magnetized, and magnetization M is induced by the applied field H so that $B = \mu_0(H+M) = 0$ inside the superconductor to account for the Meissner effect. In this case there is no supercurrent; the superconductor has permittivity ε_0 and permeability $\mu_0 M/H$, where M normally is a function of position.[12] This view shall be designated method II (See Appendix 3).

Perturbation calculations for conventional ferrite and dielectric materials have been done mainly along the lines of method II. In method II, the microscopic physical picture, such as the concepts of superfluid (Cooper pairs) and normal fluid (unpaired carriers) components, play no role. Although these formulae may be applied to superconductors, the difficulty lies in the calculation of $M(r)$ or the relative permeability $\mu_r(r)$ for a superconductor, especially when one dimension of the sample becomes comparable to the screening length. In most of the cases (geometries and field configurations), use of the two-fluid model and method I is most appropriate and convenient for superconductors. The treatment in view of method II is given in Appendix 3.

This Chapter deals with the microwave characterization of materials, especially superconducting bulk samples and films, but the

concept are important for interpreting material measurements for applications of superconductors to RF circuits. This Chapter is divided into six sections. In section 1, the complex frequency shift of the cavity due a general perturbation is derived and related to the complex power loss, which is represented by the integral of the Poynting vector over the sample surfaces. In section 2 the relation is made between the measured quantities (Q and resonant frequency) and the complex frequency shift. In section 3, we perform a first-principles calculation relating the measured quality factor and resonant frequency to the surface impedance and conductivity of the sample. A general definition of effective surface impedance is also given. In section 4, a similar calculation for the more general case of anisotropic samples is given in detail. In section 5, the hot-finger technique is discussed and data for a $YBa_2Cu_3O_{7-\delta}$(YBCO) single crystal taken by this technique is shown as an example to understand the results of sections 1 - 4. Also some general requirements of the data for bulk superconducting samples in the local London limit are discussed, and this can be used to make sure that no mistakes are made in collecting and analyzing the data. At the end of the section 5, the example of a NbN superconducting thin film is given. The understanding of the effective surface impedance discussed in section 3 is important for thin films, and the corrections to the bulk surface impedance are significant. Section 6 serves as the conclusion. There are also three apperdicer to this Chapter. Appendix 1 describe a simple alternative way to derive the complex frequency shift in a perturbed resonant cavity. Appendix 2 is a brief derivation for the energy stored in the TE_{011} mode of the cavity. Appendix

48

3 derives the complex frequency shift for a superconductor in a perturbed resonant cavity from the view of method II.

3-2   Complex Frequency Shift

Let us first consider the general theory of cavity perturbation.[10] In the unperturbed state, i.e. assuming an empty cavity with perfectly conducting walls, let the electric field and magnetic field in the cavity in one of its resonant modes be

$$E = E_0(r)e^{-i\omega_0 t}, \qquad H = H_0(r)e^{-i\omega_0 t} \tag{1}$$

where $E_0(r)=E_0 f(r)$ and $H_0(r) = H_0 g(r)$ are functions of position, and they are out of phase by $\pi/2$. E_0 and H_0 are the maximum field amplitudes inside the cavity, and ω_0 is the unperturbed resonant frequency. After loading a superconducting sample into the cavity and allowing for the finite conductivity of the walls, the resonant frequency ω_0 and the fields are modified so that

$$E = (E_0 + E_1)e^{i(\omega_0 + \delta\omega)t} \qquad H'' = (H_0{}'' + H_1{}'')e^{i(\omega_0 + \delta\tilde{\omega})t} \tag{2}$$

where we assume that the perturbations are small and the perturbed fields can be represented by $E_1(r)$ and $H_1(r)$ along with a complex frequency change $|\delta\tilde{\omega}| \ll \omega_0$. This is equivalent to requiring that the field configurations are only slightly distorted, or saying E_1 and H_1 are small compared with E_0 and H_0, except in the neighborhood of the perturbation, e. g. near the sample or the wall of the cavity. Similar calculations have been done by Waldron.[10] Using Maxwell's equations inside the cavity and following Waldron's calculation, we obtain[10]

$$-i\omega_0(E_1 \cdot D_0 - H_1 \cdot B_0) - \nabla \cdot [(H_0 \times E_1) + (E_0 \times H_1)]$$
$$= -i\omega_0(E_0 \cdot D_1 - H_0 \cdot B_1) - i\delta\tilde{\omega}[(E_0 \cdot D_0 - H_0 \cdot B_0) + (E_0 \cdot D_1 - H_0 \cdot B_1)] \tag{3}$$

49

where we have assumed that outside the perturbed locations

$$B_0 = \mu_0 H_0, \ D_0 = \epsilon_0 E_0 ; \qquad\qquad B_1 = \mu_0 H_1, \ D_1 = \epsilon_0 E_1; \qquad\qquad (4)$$

Inside the sample and the walls of the cavity,

$$B_1 = \mu_0 [\mu_r(H_1+H_0)-H_0], \qquad D_1 = \epsilon_0[\epsilon_r(E_1+E_0)-E_0] ; \qquad\qquad (5)$$

Here μ_r is the relative permeability of the sample or the wall of the cavity and ϵ_r is the relative dielectric constant. Inside a superconductor, such as the cavity wall or the sample, we consider both μ_r and ϵ_r to be equal to 1 (method I). The treatment using method II is given in Appendix 3.

At this point we deviate away from Waldron's calculation. Let V_0 be the total volume of the cavity and V_1 the volume of the sample. V_0-V_1 will be the part of the cavity not occupied by the sample, with boundary surfaces being the cavity walls and the surfaces of the sample. Hence upon integrating Eq. (3) over the volume V_0 - V_1,[13] we have

$$i\omega_0 \iiint_{V_0-V_1} (E_1 \cdot D_0 - H_1 \cdot B_0)dV + \iint_{V_0-V_1} \nabla \cdot [(H_0 \times E_1)+(E_0 \times H_1)]dV$$

$$= i\omega_0 \iiint_{V_0-V_1} (E_0 \cdot D_1 - H_0 \cdot B_1)dV$$

$$+ i\delta\tilde{\omega} \iiint_{V_0-V_1} [(E_0 \cdot D_0 - H_0 \cdot B_0)+(E_0 \cdot D_1 - H_0 \cdot B_1)]dV$$

In the volume V_0 - V_1, as $E_0 \cdot D_1 = E_1 \cdot D_0$ and $H_0 \cdot B_1 = H_1 \cdot B_0$, we have

$$\frac{\delta\tilde{\omega}}{\omega_0} = \frac{\iiint_{V_0-V_1} \nabla \cdot [(H_0 \times E_1)+(E_0 \times H_1)]dV}{i\omega_0 \iiint_{V_0-V_1} [(E_0 \cdot D_0 - H_0 \cdot B_0)+(E_0 \cdot D_1 - H_0 \cdot B_1)]dV}$$

By Green's theorem, the divergence integral becomes,

$$\iiint_{V_0-V_1} \nabla \cdot [(H_0 \times E_1)+(E_0 \times H_1)]dV$$

$$= \oiint_{S_{cavity}} [(H_0 \times E_1)+(E_0 \times H_1)] \cdot ndS + \oiint_{S_{sample}} [(H_0 \times E_1)+(E_0 \times H_1)] \cdot ndS \qquad (6)$$

where S_{cavity} is the surface of the cavity wall with corresponding normal unit vector n to the element of dS_{cavity} pointing out of the cavity, and S_{sample} is the surface of the sample with corresponding unit

50

Cavity Perturbation
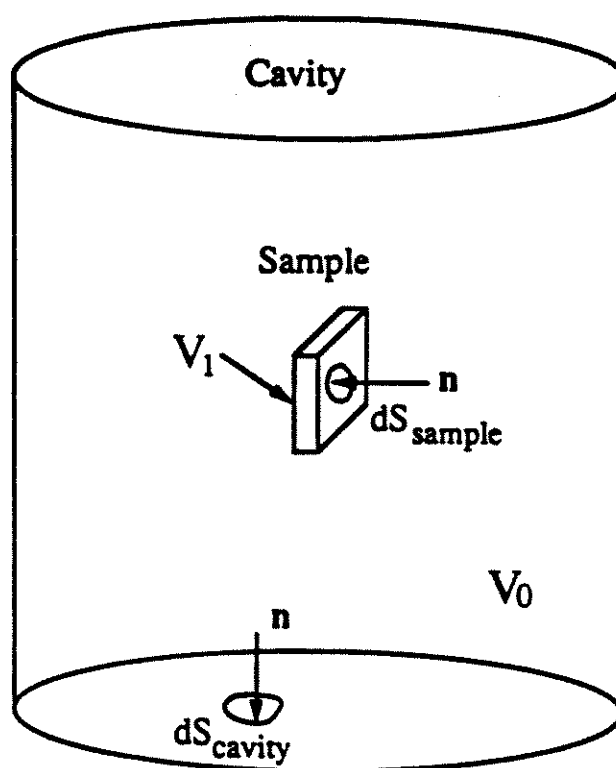
Figure 3.1 Cylindrical cavity with a rectangular sample in the center. The empty cavity is volume V_0, while the sample occupies volume V_1. The unit normal vectors used in the calculations in this paper are shown on the sample surfaces and cavity walls.

vector n normal to the element of dS_{sample} pointing into the sample (see Figure 3.1). Also because E_1 and H_1 are small compared with E_0 and H_0, and $V_1 \ll V_0$, the denominator simplifies and we have

$$\frac{\delta\tilde{\omega}}{\omega_0} \cong \frac{\oiint_{S_{walls}}[(H_0 \times E_1)+(E_0 \times H_1)]\cdot n dS + \oiint_{S_{sample}}[(H_0 \times E_1)+(E_0 \times H_1)]\cdot n dS}{i\omega_0\iiint_{V_0}(E_0 \cdot D_0 - H_0 \cdot B_0)dV} \tag{7}$$

The Poynting vector is defined as

$$p(\omega) = E \times H \tag{8}$$

$$= (E_0 + E_1) \times (H_0 + H_1).$$

For the unperturbed case, in which all surfaces are considered to be perfectly conducting, E_0 is everywhere parallel to n, and $E_0 \times H$ is always perpendicular to the surfaces, so that the surface integrals of $(E_0 \times H) \cdot n$ are zero.[14] Also, we shall henceforth neglect the second order small quality $H_1 \times E_1$. Hence the integral of the Poynting vector $p(\omega)$ reduces to the integral of $-H_0 \times E_1$ on the surface of the cavity walls and the surfaces of the sample. We can rewrite our equation for the complex frequency shift of the resonant frequency as follows:

$$\frac{\delta\tilde{\omega}}{\omega_0} = -\frac{\sum_{cavity\ walls}P(\omega) + \sum_{sample\ surfaces}P(\omega)}{2i\omega_0 <U>} \tag{9}*$$

where $P(\omega) = \oiint_{surface}p(\omega)\cdot n dS \tag{10}$

is the complex power "loss" at a surface, and

$$<U> = \tfrac{1}{2}\iiint_{V_0}(E_0 \cdot D_0 - H_0 \cdot B_0)dV \tag{11}$$

---

* The perturbation due to a superconducting sample can be thought as two step process. First is the insertion of a perfect conducting small sample into the cavity. This step causes a small constant frequency shift which is independent of the sample temperature and can be treated as an offset of the ω_0. The second step is the perturbation by considering the loss in the superconducting sample. The discussion of the perturbation due to the sample in this chapter involves the second part only.

is the time average of energy stored in the empty cavity, and by the definition of Eq. (1), $E_0 \cdot D_0 = H_0 \cdot B_0 = \mu_0 |H_0^2|$ for any cavity modes. Eqs. (9) - (11) are the general results of the cavity perturbation calculation for a sample and cavity with conducting surfaces. [For an alternative derivation of Eqs. (7) or (9), and (11), see Appendix 1; The equivalent formulae for a superconductor under method II are given in Appendix 3.]

3-3   Complex Frequency Shift and Quality Factor Q

Assume the resonant frequency of an empty, perfectly conducting cavity is ω_0, and after the introduction of a superconductor inside the cavity, it is ω',

$$\omega' = \omega_0 + \Delta\omega + i\omega'' = \omega_0 + \delta\tilde{\omega}. \tag{12}$$

There will be two contributions to the complex frequency shift $\delta\tilde{\omega}$. One is from the finite Q. It not only contributes to the imaginary part of $\delta\tilde{\omega}$, but also pulls down the resonant frequency. The second contribution to the frequency shift comes from the imaginary part of the energy "loss" (Poynting vector). This is related to the non-zero magnetic penetration depth λ of the sample or the cavity walls, which in turn changes the total inductance of the cavity.

Let us first examine the effects of a finite Q. By the well known definition of quality factor[15]

$$Q = \frac{\omega_0 <U>}{P_{absorption}}, \tag{13}$$

where $P_{absorption}$ is the real part of $P(\omega)$, we have $\frac{dU}{dt} = -\frac{\omega_0}{Q}U$, with solution $U(t) = U_0 e^{-\omega_0 t/Q}$, where U_0 is the initial amount of energy stored in the cavity.[15] The time dependence in the above equation implies that the

53

free oscillations of the fields in the cavity are damped. For the field E (or H), we must therefore have in general $\ddot{E} + 2\gamma\dot{E} + \omega_0^2 E = 0$, with solution $E = E_0 e^{-\gamma t} e^{-i(\omega_0 + \Delta\omega)t}$, $\omega_0 + \Delta\omega = \sqrt{\omega_0^2 - \gamma^2}$. As $U \propto E^2$ we can make the identity $\gamma = -\frac{\omega_0}{2Q}$, which is the damping coefficient. Since $Q \gg 1$, it is clear that $\gamma \ll \omega_0$ and $\Delta\omega = \sqrt{\omega_0^2 - \gamma^2} - \omega_0 \approx -\frac{\omega_0}{8Q^2}$. For a typical x-band superconducting cavity[16] $Q \geq 10^5$, $\omega_0 \sim 2\pi \times 10^{10}$ rad/sec, the contribution to $\Delta\omega$ due to finite Q is much less than 1 rad/sec and therefore can be ignored.

We can write ω'' from Eq. (12) as $\frac{\omega_0}{2Q}$ because

$$E(t) = E_0 e^{-\gamma t} e^{-i(\omega_0 + \Delta\omega)t} = E_0 e^{-i(\omega_0 + \Delta\omega + i(-\gamma))t} = E_0 e^{-i(\omega_0 + \Delta\omega + i\omega'')t}$$

and the complex frequency shift finally becomes

$$\frac{\delta\tilde{\omega}}{\omega_0} = \frac{\omega' - \omega_0}{\omega_0} = \frac{\Delta\omega}{\omega_0} + \frac{i}{2Q}. \tag{14}$$

with $\Delta\omega$ due mainly to the imaginary part of the energy "loss".

3-4 Complex Frequency Shift, Surface Impedance and Penetration Depth
for a Superconducting Sample

Let us consider the effect on $\Delta\omega$ due to the change of magnetic penetration depth λ of the sample. For the hot finger technique, the TE$_{011}$ mode is typically used and the sample is placed at the center of the cavity where the unperturbed electric field is zero and the magnetic field is maximum. The experimental configuration is shown in **Figure 3.2** and **Figure 3.3**.

3-4.1 Field Distribution in a Superconducting Sample
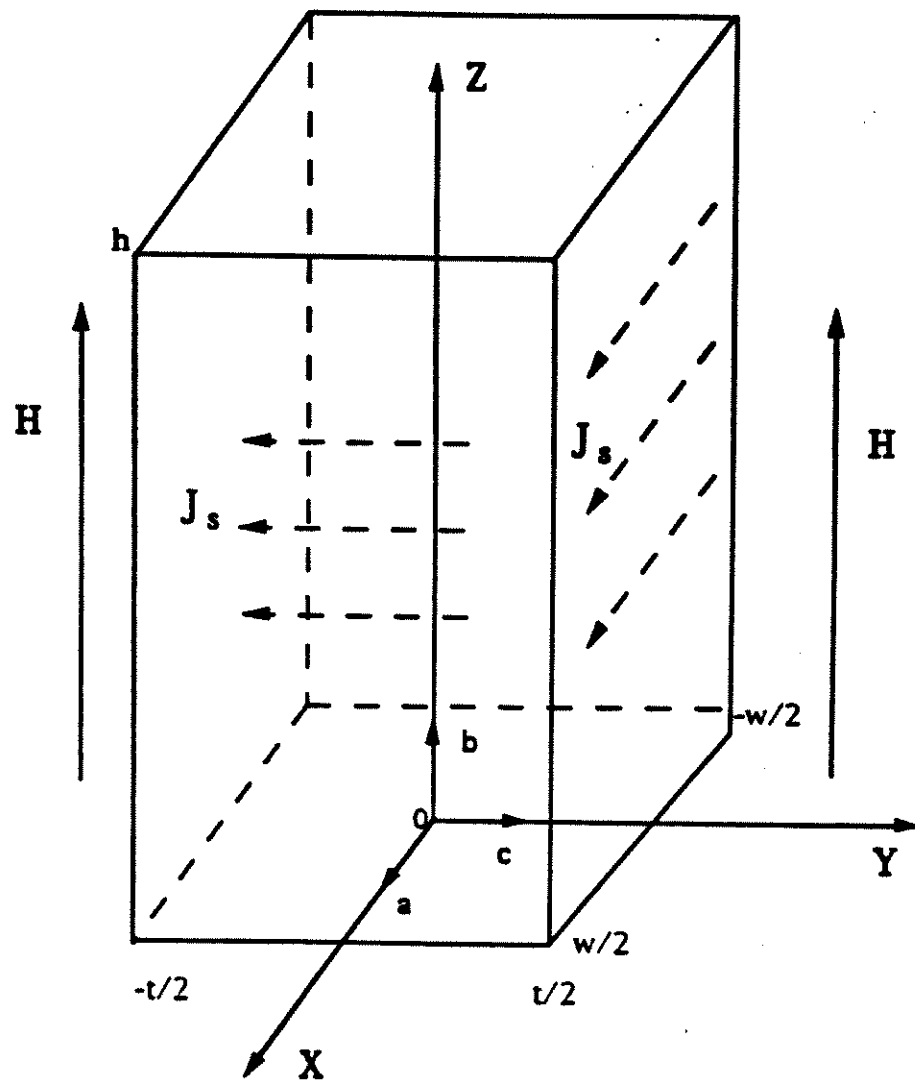
Figure 3.2 Rectangular crystal sample of width w, thickness t and height h. Note that the origin of the coordinate system is in the center of the bottom face of the crystal. Magnetic field is applied uniformly along the z-direction on four faces. Also note the orientation of the three principle crystal axes, a, b, and c, for the anisotropic crystal.

Nb Cavity

Sample Orientations

Experiment I   Experiment II
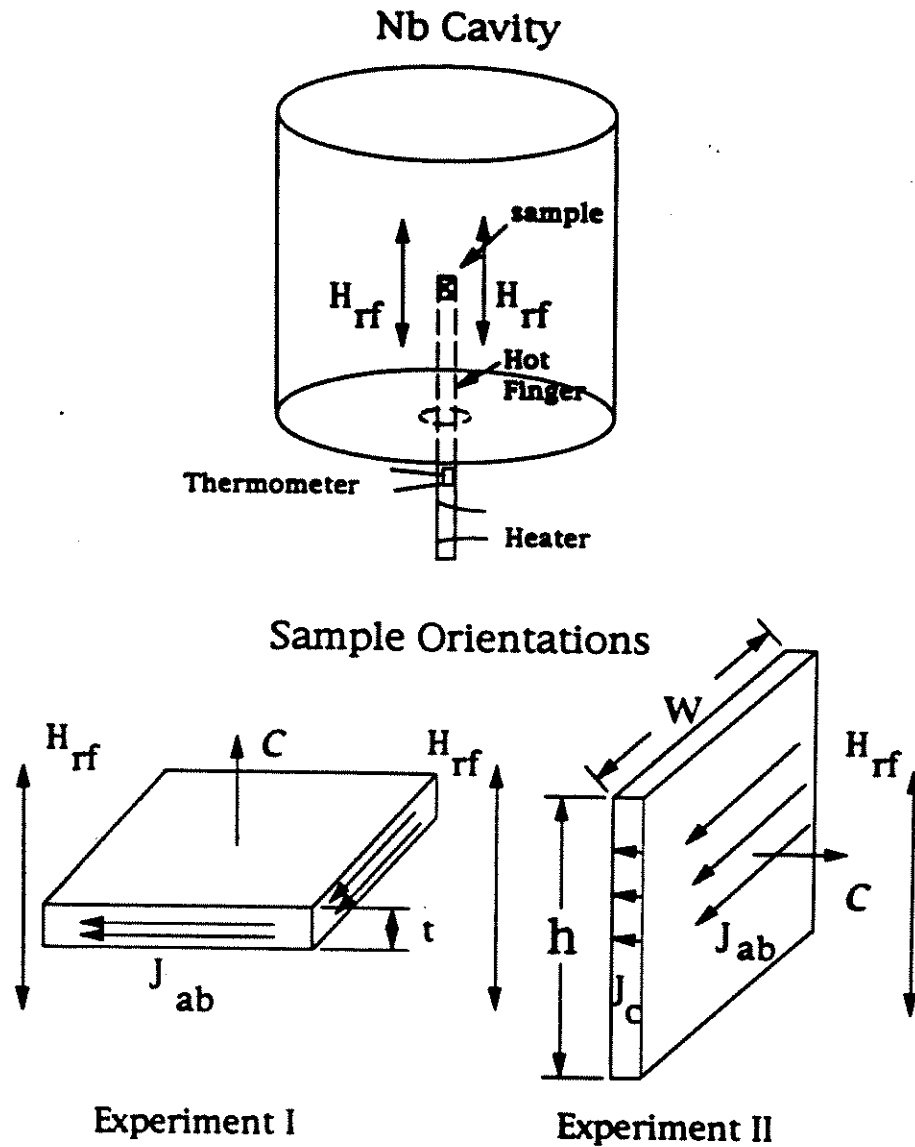
Figure 3.3 Schematic view of the hot finger technique showing the heater and thermometer on the sapphire rod hot finger outside the cavity. Also shown are experiments I and II with the sample placed in two different orientations to evaluate the anisotropy of the electrodynamic properties.

56

For an isotropic superconductor in the Meissner state in an electromagnetic field at frequency ω, Maxwell's equations and the London equations constitute a complete set of equations to calculate the electrodynamic quantities. For method I, they are

Maxwell's Equations

$$\nabla \times B = \mu_0 J_{total} + \mu_0 \frac{\partial D}{\partial t} \qquad \nabla \times E = -\frac{\partial B}{\partial t}$$

$$\nabla \cdot B = 0 \qquad\qquad \nabla \cdot E = \rho / \varepsilon_0$$

Constitutive Equations

$$B = \mu_0 H, \quad D = \varepsilon_0 E$$

$$E = \frac{\partial(\Lambda J_s)}{\partial t} \qquad \text{1st London Equation} \tag{15}$$

$$B = -\nabla \times (\Lambda J_s) \qquad \text{2nd London Equation}$$

$$\left.\begin{array}{c} J_{total} = J_s + J_n \\ J_n = \sigma_1 E \end{array}\right\} \quad \text{Two Fluid Model}$$

where $\Lambda = \mu_0 \lambda^2$.

Assume there is no free charge and no applied supercurrent. Assume the time variation of $e^{-i\omega t}$, and ignore the displacement current because it is small at microwave frequencies. We have

$$E = i\omega \Lambda J_s, \quad J_n = \sigma_1 E = i\omega \sigma_1 \Lambda J_s, \quad J_{total} = J_s + J_n = (\sigma_1 - i\sigma_2)E = \nabla \times H \tag{16}$$

Consider a simple situation: the sample thickness t is small compared with the height h and width w of the sample. In this case we can ignore field penetration from the surfaces $x = \pm w/2$ (**Figure 3.2**) and the electrodynamics are particularly simple. Solving the equations for this one dimensional problem, we have

$$\nabla^2 H = \frac{H}{\lambda'^2} \tag{17}$$

where

$$\frac{1}{\lambda'^2} = \frac{1}{\lambda^2}(1 + i\omega\sigma_1\mu_0\lambda^2) = \frac{1}{\lambda^2}(1 + i\frac{\sigma_1}{\sigma_2}) \tag{18}$$

57

and $\sigma_2 = 1/\omega\mu_0\lambda^2$.

Hence

$$H = H_0 \frac{\cosh(\frac{y}{\lambda^*})}{\cosh(\frac{t}{2\lambda^*})}, \quad E = \frac{1}{\sigma_1 - i\sigma_2}\frac{dH}{dy} = \frac{1}{\sigma_1 - i\sigma_2}\frac{H_0 \sinh(\frac{y}{\lambda^*})}{\lambda^* \cosh(\frac{t}{2\lambda^*})} \qquad (19)$$

for $-t/2 \leq y \leq t/2$ (note the geometry in **Figure 3.2**). In Eq. (19), H_0 is the applied magnetic field and is assumed to be the same at $y = \pm t/2$. Note that when $\sigma_1 \ll \sigma_2$ (T < T$_c$), $\lambda^* \sim \lambda$; whereas for T > T$_c$, $\lambda^* \cong \frac{\delta}{(1+i)}$ where $\delta = \sqrt{\frac{2}{\omega\mu_0\sigma_n}}$ is the skin depth in the normal state. In the normal state the supercurrent is zero and Eqs. (15) reduce to the normal metal case where London's equations are no longer valid, and

$$J_{total} = J_n = \sigma_1 E = \sigma_n E.$$

3-4.2 Surface Impedance and Penetration Depth

Now we define the surface impedance Z_s clearly and relate it to the measured quantities of the complex frequency shift $\delta\tilde{\omega}$ which correspond to the quality factor Q and resonant frequency ω. The effective surface impedance is defined as [15][17]

$$Z_{s\text{-}eff} \equiv \frac{P(\omega)}{\oiint_{surfaces\ of\ sample} H_t^2 dS} \qquad (20)$$

where H_t is the tangential component of the applied field. This definition is a generalization of power dissipation in an Ohmic conductor: $P = I^2 R$. As such, it requires that the conductor be in the region of linear response to the applied magnetic field. For the hot finger technique,

$$Z_{s\text{-}eff} = \frac{P(\omega)}{A H_{applied}^2} \qquad (21)$$

58

where A is the area of the sample over which (the assumed uniform) $H_{applied}$ exists, which is 2hw in the approximation of t << w, h(see **Figure 3.2**). The field $H_{applied}$ is parallel to the surfaces in the hot-finger technique.

The Poynting vector $E \times H$ is always pointed toward the inside of the sample, and by Eq. (19), we have the power loss

$$P(\omega) = \iint_{surfaces\ of\ sample} (E \times H) \cdot n\, dS = 2hw H_{applied} E|_{y=t/2}$$

$$= 2\frac{hw}{\lambda} H^2_{applied} \frac{1}{\sigma_1 - i\sigma_2} \tanh(\frac{t}{2\lambda})$$

$$= 2\frac{hw}{\lambda} H^2_{applied} \frac{i\omega\mu_0\lambda^2}{1 + i\sigma_1\omega\mu_0\lambda^2} \tanh(\frac{t}{2\lambda})$$ (assumes t<<w, h)(22)

$$\equiv Z_{s-eff} A H^2_{applied}$$

with n as defined in Eq. (6). Define

$$Z_s = R_s + iX_s \qquad (23)$$

where R_s is the surface resistance and X_s is the surface reactance. Thus

$$R_{s-eff} = \mathrm{Re}\{Z_{s-eff}\} = \frac{\omega^2\mu_0^2\lambda^3\sigma_1}{1 + (\omega\sigma_1\mu_0\lambda^2)^2} \tanh(\frac{t}{2\lambda}) \equiv R_{s,bulk} \tanh(\frac{t}{2\lambda})$$

$$X_{s-eff} = \mathrm{Im}\{Z_{s-eff}\} = \frac{\omega\mu_0\lambda}{1 + (\omega\sigma_1\mu_0\lambda^2)^2} \tanh(\frac{t}{2\lambda}) \equiv X_{s,bulk} \tanh(\frac{t}{2\lambda})$$ (24)

If the sample is several penetration depths thick but still satisfies t << h, w, then these expressions reduce to the bulk expressions for the surface impedance. For thin films, it is important to notice the $\tanh(\frac{t}{2\lambda})$ term. In this case, what is really measured is the effective surface impedance, which will be a factor of $\tanh(\frac{t}{2\lambda}) \cong \frac{t}{2\lambda}$ smaller than the bulk surface impedance. For instance, two thin films of different thickness may have the same bulk surface resistance but very different measured (effective) surface resistances (the quality factor Q), roughly proportional to the ratio of the thicknesses.

From Eqs. (8), (9), (10), and performing the integral in Eq. (20), we can now relate the measured quantities of the complex frequency shift to the surface impedance of the sample and the cavity walls,

$$\frac{\delta\tilde{\omega}}{\omega_0} = \frac{\omega' - \omega_0}{\omega_0} = \frac{\Delta\omega}{\omega_0} + \frac{i}{2Q}$$

$$= -\frac{1}{2i}\frac{\sum_{surface\ of\ sample} Z_{s,sample} A_{sample} H^2_{applied} + \sum_{cavity\ walls} Z_{s,wall} A_{wall} H^2_{applied}}{\omega_0 <U>} \quad (25)$$

From the imaginary part of above equation, we have

$$R_{s,sample} = \Gamma_s (\frac{1}{Q} - \frac{1}{Q_{cavity}}) \quad (26)$$

where

$$\Gamma_s = \frac{\omega_0 <U>}{\sum_{surface\ of\ sample} A_{sample} H^2_{applied}}, \quad \frac{1}{Q_{cavity}} = \frac{\sum_{cavity\ walls} R_{s,cavity} A_{wall} H^2_{applied}}{\omega_0 <U>} = \frac{R_{s,cavity}}{\Gamma_c} \quad \text{and}$$

$$\Gamma_c = \frac{\omega_0 <U>}{\sum_{at\ cavity\ walls} A_{area\ of\ walls} H^2_{applied}}. \quad (27)$$

Q_{cavity} is the quality factor of the cavity without the sample present.

For the reactance, the real part of Eq. (25) yields
$\Delta\omega = \omega - \omega_0$

$$= -\frac{1}{2}\frac{\sum_{cavity\ walls} X_{s,cavity} A_{wall} H^2_{applied} + \sum_{surfaces\ of\ sample} X_{s,sample} A_{sample} H^2_{applied}}{<U>} \quad (28)$$

Theoretically we can measure the resonant frequency of the cavity with and without the sample and get the reactance of the sample by use of Eq. (28). However, there will be a small difference of alignment of the cavity each time the cavity is assembled (to insert or remove the sample), therefore the cavity resonant frequency ω can not be reproduced or accounted for up to the precision we need, which is on the order of 1 rad/sec, or less. (This problem is not generally encountered with the quality factor because the loss will be dominated by the sample in most of the cases. However, the variation in Q due to measurement noise and the

60

re-assembly process will ultimately limit the surface resistance measurement resolution.) Hence we are reduced to measuring only the change of reactance of the sample, δX_s, due to the change of temperature or other reproducible variables. We must therefore define the following measurable quantities,

$$\delta\omega_{cavity\ and\ sample}(T)$$

$$=-\frac{1}{2}\frac{\sum_{walls}\delta X_{s,cavity}(T)A_{walls}H^2_{applied}+\sum_{sample\ surfaces}\delta X_{s,sample}(T)A_{sample}H^2_{applied}}{<U>}$$

$$\delta\omega_{cavity}(T)=-\frac{1}{2}\frac{\sum_{walls}\delta X_{s,cavity}(T)A_{walls}H^2_{applied}}{<U>}\qquad(29)$$

$$\nabla\omega\equiv\delta\omega_{cavity\ and\ sample}(T)-\delta\omega_{cavity}(T)$$

$$=-\frac{1}{2}\frac{\sum_{sample\ surfaces}\delta X_{s,sample}(T)A_{sample}H^2_{applied}}{<U>}$$

where $\delta\omega_{cavity\ and\ sample}(T)=\omega_{cavity\ and\ sample}(T)-\omega_{cavity\ and\ sample}(T_0)$ is the change of resonant frequency between temperature T_0 and T measured when the sample is present, and $\delta\omega_{cavity}$ is the change of resonant frequency between T_0 and T measured with the sample absent, and T refers to the temperature of the sample and finger in the hot finger technique (see Figure 3.3). We have defined a new measurable quantity

$$\nabla\omega=\delta\omega_{cavity\ and\ sample}(T)-\delta\omega_{cavity}(T),\qquad(30)$$

and find that it is proportional to the change in surface reactance of the sample: $\delta X_{s,sample}(T)=X_{s,sample}(T)-X_{s,sample}(T_0)$.

Solving for the change in surface reactance, we have

$$\delta X_{s,sample}=-\frac{\omega_0<U>}{\sum_{sample\ surfaces}A_{sample}H^2_{applied}}\frac{2}{\omega_0}\nabla\omega=-\Gamma_s\frac{2}{\omega_0}\nabla\omega=-\zeta_s\nabla\omega\qquad(31)$$

where $\zeta_s=2\frac{<U>}{\sum_{sample\ surfaces}A_{sample}H^2_{applied}}=\frac{2\Gamma_s}{\omega_0}\qquad(32)$

61

As $X_s = \text{Im}(Z_s) = \dfrac{\omega \mu_0 \lambda}{1 + (\omega \sigma_1 \Lambda)^2}\tanh(\dfrac{t}{2\lambda})$, in the limit of $t \gg \lambda$, and $T \ll T_c$, we

have

$X_s = \omega \mu_0 \lambda$ for a bulk superconductor. $\qquad\qquad$ (33)

Hence in the superconducting state for sufficiently thick samples, we have

$$\Delta\lambda = -\Gamma_s \frac{2}{\mu_0 \omega_0^2}\nabla\omega = -\xi_s \nabla\omega \qquad\qquad (34)$$

where $\xi_s = \dfrac{2}{\mu_0 \omega_0^2}\Gamma_s = \dfrac{\zeta_s}{\mu_0 \omega}$ $\qquad\qquad$ (35)

Now we understand how the measurable quantities $\Delta\omega$ and Q are related to surface resistance, surface reactance and penetration depth through Eqs.(11), (26), (28), (33) and (34).

3-5 Anisotropic Crystals

Let us consider a more general case: the sample has anisotropic electromagnetic properties, with width w, height h and thickness t. Here we generalize the results of Ning, et al.[18] to finite frequencies and the inclusion of losses (for instance due to the non zero normal current at finite temperature for a superconductor). We shall assume that de-magnetization effects are negligible (see [19]). Eqs. (15) still apply except that the conductivity σ and parameter Λ become tensor quantities $\bar{\sigma}$ and $\bar{\Lambda}$.

Maxwell's Eqs:

$$\nabla \times E = -\frac{\partial B}{\partial t} \qquad\qquad (36)$$

$$\nabla \times H = J_{total} \qquad\qquad (37)$$

Constitutive Eqs:

$$E = \frac{\partial(\bar{\Lambda}\cdot J_s)}{\partial t} \qquad\qquad (38)$$

$$B = -\nabla \times (\bar{\Lambda}\cdot J_s) \qquad\qquad (39)$$

62

$$J_{total} = J_s + J_n$$

$$= (\bar{\sigma}_1 - i\bar{\sigma}_2) \cdot E \tag{40}$$

$$J_n = \bar{\sigma}_1 \cdot E \tag{41}$$

Combining Eqs.(37) , (40) and (41), we get

$$J_s = \nabla \times H - J_n = \nabla \times H - \bar{\sigma}_1 \cdot E$$

Now use Eq. (38) and again assume the time dependence of $e^{-i\omega t}$ for $E, H,$ and J, we have

$$J_s = \nabla \times H - i\omega \bar{\sigma}_1 \cdot \bar{\Lambda} \cdot J_s$$

Solving for J_s yields:

$$J_s = \frac{\nabla \times H}{(1 + i\omega \bar{\sigma}_1 \cdot \bar{\Lambda})} \tag{42}$$

Now put this into Eq.(39) to get an equation for the magnetic field in the sample

$$\mu_0 H = -\nabla \times \left\{ \bar{\Lambda} \cdot \frac{\nabla \times H}{(1 + i\omega \bar{\sigma}_1 \cdot \bar{\Lambda})} \right\} \tag{43}$$

Suppose H is in the z-direction, $H = H_z\hat{z}$ and also assume that the z-direction is along one of the principle crystal axes, such as the b direction in a cuprate superconductor (see **Figure 3.2**). Then

$$\nabla \times H = \hat{i}\frac{\partial H_z}{\partial y} - \hat{j}\frac{\partial H_z}{\partial x} = \begin{pmatrix} \frac{\partial H_z}{\partial y} \\ -\frac{\partial H_z}{\partial x} \\ 0 \end{pmatrix}. \tag{44}$$

The tensors are (see **Figure 3.2**)

$$\bar{\Lambda} = \begin{pmatrix} \Lambda_a \hat{x}\hat{x} & 0 & 0 \\ 0 & \Lambda_c \hat{y}\hat{y} & 0 \\ 0 & 0 & \Lambda_b \hat{z}\hat{z} \end{pmatrix} \tag{45}$$

where Λ_i is associated with the current flowing in the ith direction.

$$\bar{\sigma}_1 = \begin{pmatrix} \sigma_a \hat{x}\hat{x} & 0 & 0 \\ 0 & \sigma_c \hat{y}\hat{y} & 0 \\ 0 & 0 & \sigma_b \hat{z}\hat{z} \end{pmatrix} \qquad (46)$$

where σ_i is the conductivity along the ith axis of the crystal.

Doing the matrix multiplication, we have

$$\frac{1}{(1+i\omega\bar{\sigma}_1 \cdot \bar{\Lambda})} = \begin{pmatrix} \frac{1}{(1+i\omega\sigma_a\Lambda_a)}\hat{x}\hat{x} & 0 & 0 \\ 0 & \frac{1}{(1+i\omega\sigma_c\Lambda_c)}\hat{y}\hat{y} & 0 \\ 0 & 0 & \frac{1}{(1+i\omega\sigma_b\Lambda_b)}\hat{z}\hat{z} \end{pmatrix} \qquad (47)$$

$$\bar{\Lambda} \cdot \frac{\nabla \times H}{(1+i\omega\bar{\sigma}_1 \cdot \bar{\Lambda})} = \begin{pmatrix} \Lambda_a\hat{x}\hat{x} & 0 & 0 \\ 0 & \Lambda_c\hat{y}\hat{y} & 0 \\ 0 & 0 & \Lambda_b\hat{z}\hat{z} \end{pmatrix} \begin{pmatrix} \frac{1}{1+i\omega\sigma_a\Lambda_a}\frac{\partial H}{\partial y} \\ -\frac{1}{1+i\omega\sigma_c\Lambda_c}\frac{\partial H}{\partial x} \\ 0 \end{pmatrix}$$

$$= \begin{pmatrix} \frac{\Lambda_a}{1+i\omega\sigma_a\Lambda_a}\frac{\partial H}{\partial y} \\ -\frac{\Lambda_c}{1+i\omega\sigma_c\Lambda_c}\frac{\partial H}{\partial x} \\ 0 \end{pmatrix} \qquad (48)$$

$$-\nabla \times \left(\bar{\Lambda} \cdot \frac{\nabla \times H}{(1+i\omega\bar{\sigma}_1 \cdot \bar{\Lambda})} \right) = - \begin{vmatrix} \hat{i} & \hat{j} & \hat{k} \\ \frac{\partial}{\partial x} & \frac{\partial}{\partial y} & \frac{\partial}{\partial z} \\ \frac{\Lambda_a}{1+i\omega\sigma_a\Lambda_a}\frac{\partial H}{\partial y} & -\frac{\Lambda_c}{1+i\omega\sigma_c\Lambda_c}\frac{\partial H}{\partial x} & 0 \end{vmatrix} \qquad (49)$$

$$= \hat{k}\left(\frac{\Lambda_a}{1+i\omega\sigma_a\Lambda_a}\frac{\partial^2 H}{\partial y^2} + \frac{\Lambda_c}{1+i\omega\sigma_c\Lambda_c}\frac{\partial^2 H}{\partial x^2} \right)$$

As $H = H_a\hat{k}$ at the surfaces of the rectangular crystal, we have a simple scalar equation for the magnetic field

$$\mu_0 H = \frac{\Lambda_a}{1+i\omega\sigma_a\Lambda_a}\frac{\partial^2 H}{\partial y^2} + \frac{\Lambda_c}{1+i\omega\sigma_c\Lambda_c}\frac{\partial^2 H}{\partial x^2} \qquad (50)$$

The solution to this equation is given in Ning's thesis as Eq. III-3.3.2,[20]

64

$$H(x,y) = \sum_{n=odd} \frac{4H_o}{n\pi}\left(\cosh(\beta_n x) - \sinh(\beta_n x)\tanh(\frac{\beta_n w}{2})\right)\sin(\frac{n\pi}{t}y)$$

$$+ \sum_{n=odd} \frac{4H_o}{n\pi}\left(\cosh(\gamma_n y) + \sinh(\gamma_n y)\tanh(\frac{\gamma_n t}{2})\right)\sin(\frac{n\pi}{w}x) \qquad (51)$$

where

$$\beta_n = \frac{\sqrt{1+i\omega\sigma_c\lambda_c^2}}{\lambda_c}\sqrt{(\frac{n\pi}{t})^2\frac{\lambda_a^2}{1+i\omega\sigma_a\lambda_a^2}+1}$$

$$\gamma_n = \frac{\sqrt{1+i\omega\sigma_a\lambda_a^2}}{\lambda_a}\sqrt{(\frac{n\pi}{w})^2\frac{\lambda_c^2}{1+i\omega\sigma_c\lambda_c^2}+1} \qquad (52)$$

This solution is valid everywhere except along the edges of the sample (e. g. the set of points along y = t/2 and x = w/2). The power absorbed in an anisotropic crystal (refer to **Figure 3.2.**) is given by,

$$P(\omega) = \oiint_{surfaces} p(\omega) \cdot n dS$$

$$= \oiint_{surfaces} (E \times H) \cdot n dS \qquad (53)$$

$$= \oiint_{surfaces}\left(\left(i\omega\bar{\Lambda}\cdot\frac{\nabla\times H}{(1+i\omega\bar{\sigma}_1\bar{\Lambda})}\right)\times H\right)\cdot n dS$$

Using Eq.(48), we have

$$P(\omega) = \oiint_{surfaces} i\omega \begin{vmatrix} \hat{i} & \hat{j} & \hat{k} \\ \frac{\Lambda_a}{1+i\omega\sigma_a\Lambda_a}\frac{\partial H}{\partial y} & -\frac{\Lambda_c}{1+i\omega\sigma_c\Lambda_c}\frac{\partial H}{\partial x} & 0 \\ 0 & 0 & H \end{vmatrix} \cdot n dS$$

$$= \oiint_{surfaces} -\left(\hat{j}(H\frac{\Lambda_a}{1+i\omega\sigma_a\Lambda_a}\frac{\partial H}{\partial y}) + \hat{i}(H\frac{\Lambda_c}{1+i\omega\sigma_c\Lambda_c}\frac{\partial H}{\partial x})\right) n dS$$

$$P(\omega) = 2i\omega h\oint_{y=\frac{t}{2} surface}(H\frac{\Lambda_a}{1+i\omega\sigma_a\Lambda_a}\frac{\partial H}{\partial y})dx$$

$$+ 2i\omega h\oint_{x=\frac{w}{2} surface}(H\frac{\Lambda_c}{1+i\omega\sigma_c\Lambda_c}\frac{\partial H}{\partial x})dy \qquad (54)$$

where the unit normal vector n is pointing into the sample, so that the power goes into the sample, and H(x, y) is given by Eq. (51) in general.

65

To simplify this problem, we consider the situation of a slightly anisotropic crystal so that one has a linear superposition of fields applied on each side of the sample. In other words, let us make an approximation that the crystal is thick compared to the penetration depths, i. e. $w \gg \lambda_c$, $t \gg \lambda_a$. Then when we evaluate the integrals in Eq. (54), such as the one on the $y = t/2$ surface, we can ignore the contribution from the applied field on the sides $x = \pm w/2$. This is because the field will decay very fast (in length scale λ_c) from the edges (e.g. $y = t/2$ and $x = \pm w/2$) and the contribution to the integral over this small edge area, as well as over the $y = t/2$ surface, will be small compared with the contribution from the applied fields on the $y = \pm t/2$ surface. In this case, we may use

$$H(x,y) \approx H(y) = H_a \frac{\cosh(\frac{y}{\lambda_{ab}})}{\cosh(\frac{t}{2\lambda_{ab}})}$$ to evaluate the integral of Eq. (54) at surface y

$= t/2$ and $H(x,y) \approx H(x) = H_a \dfrac{\cosh(\frac{x}{\lambda_c})}{\cosh(\frac{w}{2\lambda_c})}$ to evaluate the integral of Eq. (54) at

surface $x = w/2$. Hence Eq. (54) gives us

$$P(\omega) \cong 2H_a \frac{i\omega\Lambda_a}{1+i\omega\sigma_a\Lambda_a} \frac{H_a}{\lambda_a} \frac{\sinh(\frac{t}{2\lambda_a})}{\cosh(\frac{t}{2\lambda_a})} hw + 2H_a \frac{i\omega\Lambda_c}{1+i\omega\sigma_c\Lambda_c} \frac{H_a}{\lambda_c} \frac{\sinh(\frac{w}{2\lambda_c})}{\cosh(\frac{w}{2\lambda_c})} ht$$

$$= 2H_a^2 hw \frac{i\omega\Lambda_a}{1+i\omega\sigma_{ab}\Lambda_a} \tanh(\frac{t}{2\lambda_a}) + 2H_a^2 ht \frac{i\omega\Lambda_c}{1+i\omega\sigma_c\Lambda_c} \tanh(\frac{w}{2\lambda_c}) \qquad (55)$$

$$\cong 2H_a^2 hw \frac{i\omega\Lambda_a}{1+i\omega\sigma_{ab}\Lambda_a} + 2H_a^2 ht \frac{i\omega\Lambda_c}{1+i\omega\sigma_c\Lambda_c}$$

$$= Z_{s,a,bulk}H_a^2 hw + Z_{s,c,bulk}H_a^2 ht \qquad \text{(assuming } w \gg \lambda_c, t \gg \lambda_a)$$

where $Z_{s,a}$ and $Z_{s,c}$ are the surface impedance associated with current flowing along the a-axis or along the c-axis, respectively. Hence a measurement of Q(T) and f_{res}(T) for an anisotropic crystal in the

66

configuration shown in **Figure 3.2** results in a weighted sum of the a-axis and c-axis surface impedances. Obviously, two other measurements done on the crystal with its a, b and c-axes permuted will result in two additional weighted sums, from which the three surface impedances can be deduced. An example of this method applied to a bi-axial crystal was done by Mao *et al.*, on twinned crystals of $YBa_2Cu_3O_7$.[1] In that paper two experiments were performed. In experiment I, illustrated in **Figure 3.3**, the induced rf current only runs in the ab-plane. The measurements of the quality factor Q and resonant frequency ω, using Eqs. (26), (33) and (34), give us the surface resistance and penetration depth of the ab-plane in the twinned crystal. And in experiment II, the induced current flows along a- (or b-) and c-axis directions. The measurements of Q and ω give us the the effective surface impedance and penetration depth, which is a weighted sum of ab-plane and c-axis properties. The power loss in experiment II is

$$P(\omega) = Z_{s,eff,bulk}H_s^2h(w+t)$$

$$= Z_{s,ab,bulk}H_s^2hw + Z_{s,c,bulk}H_s^2ht$$

(56)

By Eqs. (23), (33), we have

$$\lambda_c = [\lambda_{eff}(w+h) - \lambda_{ab}w]/t$$

$$R_{s-c} = [R_{s-eff}(w+h) - R_{s-ab}w]/t$$

(57)

Therefore we can deduce the c-axis information through de-convolution of Experiments I and II.[1]

3.6   Discussion of the Hot-Finger Technique

In the past there has been a great deal of confusion about the connection between the complex frequency shift and the surface impedance of a superconductor. For example, consider the following

equation for the complex frequency shift as described in reference 9 as Eq. (3.9):

$$\frac{\Delta\tilde{\omega}}{\omega} \equiv \frac{(1-\mu_r)\mu_0}{4<U>}\iiint_{sample} H \cdot H_0 dV + \frac{(1-\varepsilon_r)\varepsilon_0}{4<U>}\iiint_{sample} E \cdot E_0 dV ,$$

where $\tilde{\omega} = \omega - i\omega/2Q$, originated from Waldron's calculation[6]. Apparently it assumes method II because this formula will be only valid if we consider a superconductor as a material with magnetization but without supercurrent.[13] A good example of the field distribution for a superconductor in a magnetic field using method II is given in reference [12]. In this formalism, a magnetization replaces the circulating supercurrent of method I, and the magnetic field H is a constant inside and outside the sample, and is equal to the applied field. The use of Eq. (1.2) of [9]: $Z_s = i\omega\mu_0\int\frac{H_z(y)}{H_z(0)}dy$ (Figure 3.2, in the case of t << h,w) will not give a valid definition for Z_s as $H_z(y) \equiv H_z(0)$ inside the sample and hence can not be applied to derive Eq. (3.11) of [9]: $\Delta(\frac{1}{Q}) - i2\frac{\Delta\omega}{\omega} = Z_s\frac{1-\mu_r}{2\omega_0<U>}\int H_t(0) \cdot H_c \, dA_s$. Therefore, the derivation of the geometric factor in [9] is not valid at all. Obviously, the mistake is in Eq. (3.9) above, as $\mu_r = M_z(y)/H_z + 1$ is a function of position, and while using method II it can not be moved out of the integral, and Z_s should be defined by our Eq. (20).

3-6.1 Geometric Factor for TE$_{011}$ mode

The derivation of the geometry factor is as follows. In the TE$_{011}$ mode of a cylindrical cavity of radius R and height L, the average energy stored in a cycle is (see Appendix 2),

68

$$\langle U \rangle = \frac{1}{2} \iiint_{V_0} (E_0 \cdot D_0 - H_0 \cdot B_0) dV$$

$$= \frac{B_0^2 V_0}{4\mu_0} [1 + (\frac{\pi R}{x_{01} L})^2] J_0^2(x_{01}') \tag{58}$$

where J_0 is the Bessel function, x_{01}' is the 1st root of $J_0'(x) = 0$, and $B_0 = \mu_0 H_0$ is the maximum magnetic field in the TE_{011} mode. For the hot finger technique (**Figure 3.3**), $H_{applied}$ is H_0 and calculation of the geometric factor by Eqs. (27) and (58) yields

$$\Gamma_s = \frac{\omega_0 \mu_0}{4} \frac{V_0}{A} [1 + (\frac{\pi R}{x_{01} L})^2] J_0^2(x_{01}'). \tag{59}$$

where $A = 2hw$ is the area of the sample in the approximation that $t \ll h$, w. (See Appendix 2).

3-6.2 $YBa_2Cu_3O_7$ crystal data

Here we shall discuss in detail the data analysis for an interesting superconducting sample, $YBa_2Cu_3O_7$ (YBCO). A cylindrical Nb cavity is immersed in liquid helium at 4.2K, and the small crystal of $YBa_2Cu_3O_7$ is placed in the center of the cavity on the tip of a sapphire hot finger (see Fig. 3.3). The cavity is a two port microwave device, so that a transmission measurement can be made of the TE_{011} resonance using the S-parameters S_{12} and S_{21}. The measurements of quality factor Q and resonant frequency are done by taking both the magnitude and phase information of the transmission S-parameter S_{21} into account at weak coupling (with coupling constants β less than 1%) using a HP-8510C vector network analyzer system. The coupling constants used to determine the unloaded Q are determined by measuring the reflection coefficients S_{11} and S_{22} on resonance. (See Chapter 2).
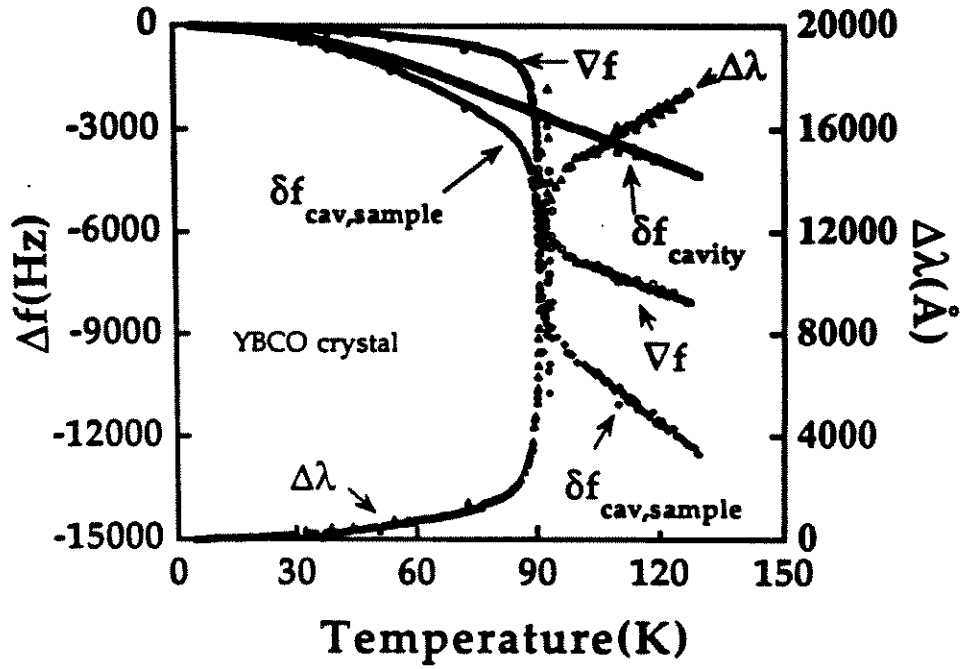
Figure 3.4 Data of the temperature dependence of the measured resonant frequency shift and the change of penetration depth of a $YBa_2Cu_3O_{7-\delta}$ single crystal. δf_{cavity} is the background resonant frequency measured without a sample (including the sapphire rod). $\delta f_{cav \ and \ sample}$ is the resonant frequency measured with the sample present. Both measurements were done with a cavity temperature of 4.2 K. ∇f is resonant frequency shift due to the sample and is obtained through $\delta f_{cav \ and \ sample}$ - δf_{cavity}. $\Delta\lambda$ is determined by Eqs. (34) and (35).

70

Figure 3.4 shows the raw data for the change of resonant frequency of the cavity with and without a $YBa_2Cu_3O_7$ single crystal sample in the geometry of experiment I of **Figure 3.3**. The δf_{cavity} of Eq. (29) in the case of the hot finger technique also includes the (background) frequency shift due to the very low loss sapphire rod (with a radius of 1 mm in our experiments[1], **Figure 3.3**). This background can be fitted to a polynomial in temperature, and is found to be highly reproducible. The frequency shift $\nabla f(T)$ due to the sample is obtained by Eq. (29), via the measured quantities $\delta f_{cavity\ and\ sample}(T)$ and $\delta f_{cavity}(T)$, also shown in **Figure 3.4**. Finally, the change in penetration depth of the sample, $\Delta\lambda(T)$, can be obtained using Eq. (34), and is also shown in **Figure 3.4**. Data obtained in this way clearly show that $\Delta\lambda \sim T$ at low temperatures in the YBCO crystals. The measurements are performed at approximately 9.6 GHz.

Figure 3.5 shows the raw data of the quality factor Q of the cavity with and without the $YBa_2Cu_3O_7$ single crystal sample in the geometry of experiment I of **Figure 3.3**. Note that the "empty" cavity has a Q exceeding 20 million at 4.2K. One can then apply Eqs. (26), (27) and (59) to obtain the surface resistance $R_s(T)$, also shown in **Figure 3.5** on a log scale.[1][16] This crystal has a rather broad transition, but shows the interesting non-monotonic temperature dependence originally noted by Bonn, *et al.*[22] in high quality YBCO crystals.

3-6.3   Consistency Checks on the Data

In this section we set down some basic requirements that one can impose on data obtained by the cavity perturbation technique for bulk
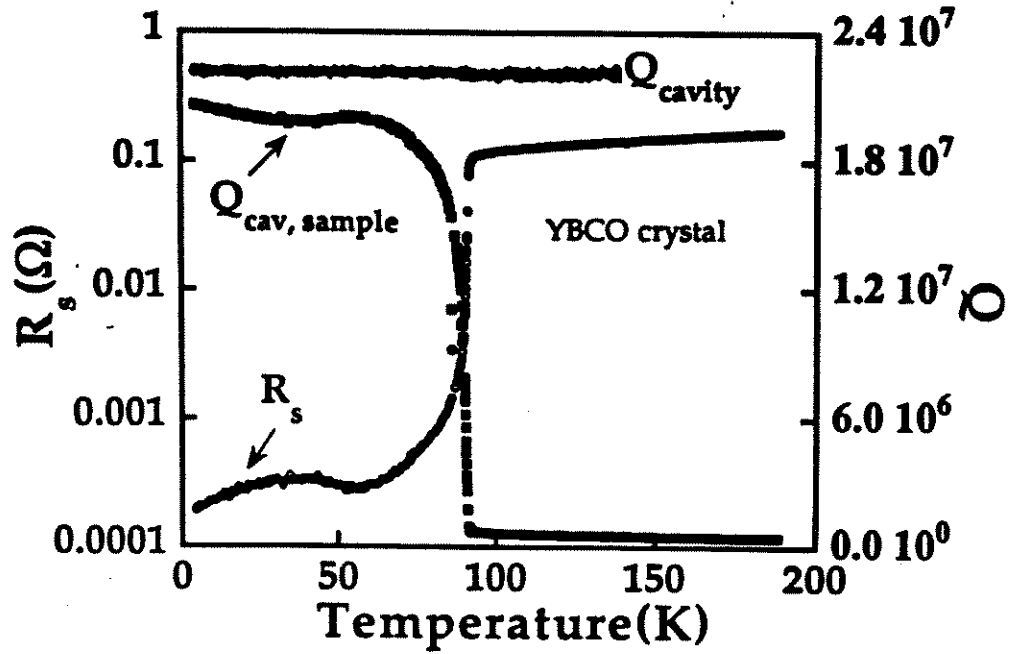
Figure 3.5 Data of the temperature dependence of the measured quality factor Q and the surface resistance of a $YBa_2Cu_3O_{7-\delta}$ single crystal. Q_{cavity} is the background quality factor measured without a sample (including the sapphire rod). $Q_{cav\ and\ sample}$ is the quality factor measured with the sample. Both measurements were done with a cavity temperature of 4.2 K. The surface resistance R_s is determined by Eq. (26) and is shown on a log-linear plot. At temperatures above 140 K where the sample is in the normal state, the loss due to the cavity background is neglegible. Thus Q_{cavity} is not measured and the surface resistance is determined solely by $Q_{cav\ and\ sample}$.

superconducting metals in the local limit. We have found these guidelines very useful in our work.

Generally, the data for a bulk sample must satisfy the following requirements:

1. $X_s (T > T_c) = R_s (T > T_c)$ (55)

for the normal state of a superconductor in the local limit. However, this condition may not hold for highly anisotropic crystals.[19]

2. Twice the frequency shift Δf of the cavity between the normal and superconducting state should equal the total change in bandwidth of the resonance $\delta f_N - \delta f_S$:

$2\Delta f = f_S - f_N \approx \delta f_N - \delta f_S$ (56)

with the assumption that $X_s (T > T_c) = R_s (T > T_c) >> X_s(T << T_c), R_s(T << T_c)$, which holds for most superconductors. This can be deduced by putting Eqs. (26), (27) and Eqs (31), (32) into

$X_s(T > T_c) - X_s(T << T_c) \approx R_s(T > T_c) - R_s(T << T_c)$. **Figure   3.6** shows the relation.

3. The measured normal state surface resistance should satisfy

$R_s(T > T_c) \cong \sqrt{\dfrac{\mu_0 \omega \rho_n(T > T_c)}{2}}$ (57)

where $\rho_n(T)$ is the dc resistivity. Again this is true only in the local limit.

It is a good practice to check these conditions to make sure that no mistakes were made in collecting and analyzing the data. For instance, in the data shown in **Figs. 3.4** and **3.5**, the Q (100 K) is about 6.5×10^5, and Q (4.2 K) is about 2.1×10^7 at 9.6 GHz. The total change of bandwidth $\Delta \delta f$ is thus about 1.46×10^4, and we can see from **Figure 3.4** that the frequency
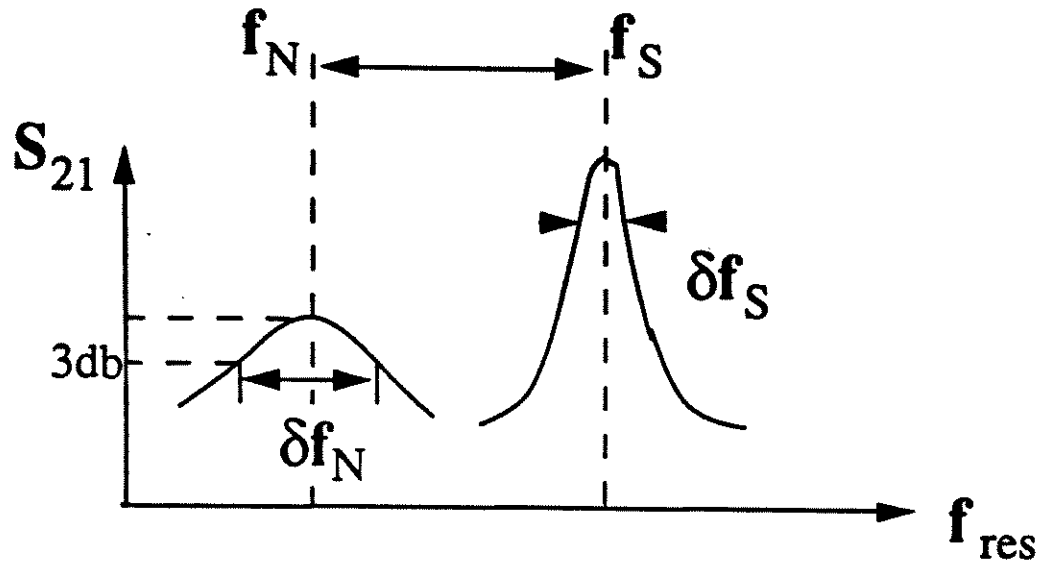
Figure 3.6 f_N is the resonant frequency in the normal state just above the transition temperature. δf_N is the corresponding 3db bandwidth. f_s is the resonant frequency in the superconducting state at low temperatures. δf_s is the related 3db bandwidth. They satisfy $2\Delta f = f_N - f_s \approx \delta f_N - \delta f_s$.

shift Δf of the cavity between the normal and superconducting state is about 7100 Hz, therefore requirement 2 above is satisfied.

Comparisons of the measured normal state surface resistance and DC resistivity through Eq. (57) are also carried out routinely in our lab.

Also note that $\lambda(0)$ may be estimated from the comparison of $R_s(T)$ and $\Delta X_s(T)$ in the normal state.[1] For a bulk material, since $X_s = \mu_0 \omega \lambda$, we have

$$X_s(0K) = \mu_0 \omega \lambda(0) = X_s(T > T_c) - \mu_0 \omega \Delta \lambda \qquad (58)$$

where $\Delta \lambda$ is the measured penetration depth change from 0 K to temperature T. We have used this method to estimate the zero temperature penetration depth of $YBa_2Cu_3O_7$ single crystals.[1]

3-6.4 Thin Film Superconductor

Figure 3.7 shows the effective surface impedance data for a NbN film with thickness t ~ 8000Å on a Si substrate measured by the hot finger technique in the geometry of experiment II in **Figure 3.3**. The effective impedance is obtained from the Q and resonant frequency shift via Eqs. (26), (59), (31) and (32). There is a mysterious peak in $X_{s,eff}(T)$ (or a dip in resonant frequency vs. temperature) just below T_c which has not been seen in measurements on any bulk sample. With a dc resistivity in the normal state of 85 $\mu\Omega$cm, the bulk surface resistance and surface reactance are expected to be similar to those shown in **Figs. 3.4** and **3.5**, namely $R_s = X_s = 0.174 \ \Omega$, which is requirement 3 of section 5c. Comparing this estimate with the data shown in **Figure 3.7**, it is easy to see that in the normal state, the measured R_s and X_s are far smaller than the bulk

75
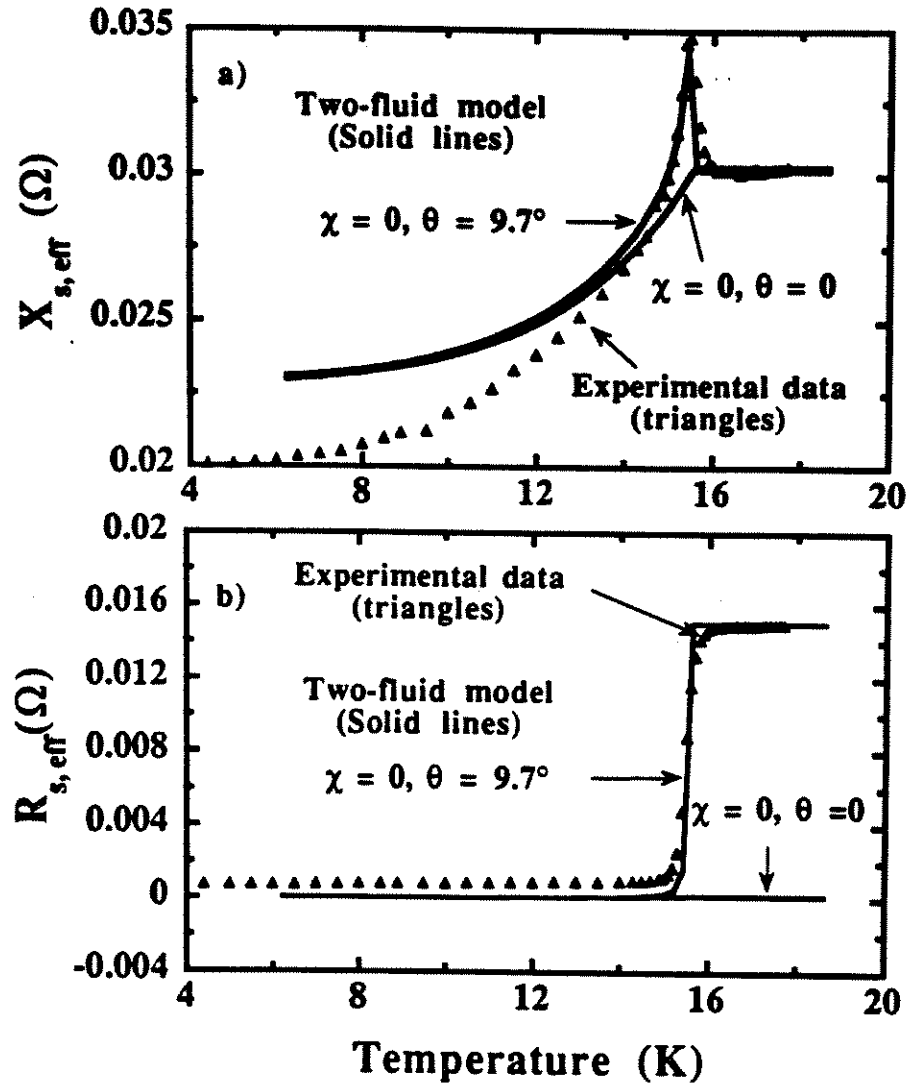
Figure 3.7 The effective surface impedance vs. temperature for a NbN thin film. The solid lines are the two-fluid model fits. The fits labelled χ = 0, θ = 0 are the prediction of Eq. (24). The fits labelled χ = 0, θ = 9.7° assume only a phase difference between fields on either side of the film and reproduce all the major features of the data.

estimates. Similar effects, i. e. *a peak* in $X_{s, eff}(T)$ but not in $R_{s, eff}(T)$, with the *peak height* varying from sample to sample, and even $X_{s, eff}(T > T_c)$ being smaller than $X_{s, eff}(T = 0)$, have been seen in all measurements of thin films, including NbN, $YBa_2Cu_3O_{7-\delta}$ and $Nd_{1.85}Ce_{0.15}CuO_4$ superconductors. Again, this behavior is never seen in measurements of bulk samples.

Of course, thin films will have a significant correction to the measured surface impedance, as we saw in the derivation of Eq. (24). In the normal state, Eq. (24) can be simplified with the assumption that the thickness t ~ 8000Å is much less than the skin depth $\delta = \sqrt{\frac{2}{\omega\mu_0\sigma_n}} \approx 4.7\mu m$ for the NbN film, using the expansion of hyperbolic functions in a power series

$$\tanh x = x - \frac{x^3}{3} + \cdots \text{ and } \coth x = \frac{1}{x} + \frac{x}{3} - \cdots \tag{59}$$

for small variable x[23]. For the NbN film, in the normal state, the penetration depth is replaced by $\lambda^* = \frac{\delta}{1+i}$ as in Eq. (19), and the complex conductivity σ becomes simply a real number σ_n. Thus, Eq. (24) can be written as

$$Z_{s-eff} = \frac{\omega\mu_0\delta}{2}\left[\frac{1}{6}(\frac{t}{\delta})^3 + i(\frac{t}{\delta})\right]$$

$$= R_{s,bulk}\left[\frac{1}{6}(\frac{t}{\delta})^3 + i(\frac{t}{\delta})\right] \qquad \text{(for T>T}_c\text{, and } \delta >> t\text{)} \tag{60}$$

Apparently the correction to the bulk surface impedance is important, i.e. the $(\frac{t}{\delta})^3$ factor for the surface resistance of a thin film will dramatically change the measured quality factor Q compared with that of a bulk sample of the same quality. A calculation of $Z_{s,eff}(T) = \frac{1}{\sigma\lambda^*(T)}\tanh(\frac{t}{2\lambda^*(T)})$ with a simple two-fluid Gorter-Casimir conductivity is shown in **Figure 3.7** as the solid lines labeled $\chi = 0$.

Comparing this effective surface impedance calculation with the data shown in **Figure 3.7**, it is easy to see that in the normal state X_S is approximately correct (although the peak in X_S is not reproduced), whereas the measured R_s is far bigger than what one would expect from Eq. (24).

One possible explanation for the discrepancy between Eq. (24) or Eq. (60) and the data is the presence of asymmetric magnetic fields (magnitude) at the two surfaces of the thin film.[24] Reasons for this may include a non-unity magnetic permeability of the substrate, or a slight misalignment of the film in the cavity. Another possibility is that there is a phase difference between the fields on both sides of the films. This phase difference can be caused by the substrate, and the size of the phase shift will depend on the dielectric constant and the thickness of the substrate. As we mentioned in section 3-2, the perturbation of the fields near the sample do not need to be small compared with the unperturbed resonant modes. Hence, the fields in the neighborhood of the sample could be very different with the eigen modes.

We now calculate the effects of the asymmetric magnetic fields on the measured effective surface impedance of a superconducting sample. In the case of the fields applied on the surfaces $y = \pm\, t/2$ are different (see **Figure 3.1** and **Figure 3.2**) and assuming $t \ll w, h$, the effective surface impedance of Eq. (24) must be modified. Assume the field on the $y= -\,t/2$ side is H_L and the field on the $y = +\,t/2$ side is

$$H_R = H_L \eta e^{i\theta}$$

where $0 \leq \eta = 1 - \chi \leq 1$ represents the asymmetry of the magnitude of the field and θ represents the difference of the phase angle. The case $\chi = 0$ and $\theta = 0$ corresponds to the symmetric field case considered above, and $\chi = 1$ and $\theta = 0$ corresponds to finite field on only one side of the sample. We expect in our case that χ will be small because of the design of the cavity system. Following Eqs. (15) and (17), we have for the field distribution in the sample,

$$H(y) = \frac{-H_L}{2\sinh(t/\lambda^*)} \left\{ [e^{-t/2\lambda^*} - \eta e^{i\theta} e^{t/2\lambda^*}]e^{y/\lambda} + [-e^{-t/2\lambda^*} + \eta e^{i\theta} e^{-t/2\lambda^*}]e^{-y/\lambda^*} \right\} \quad (61)$$

$$E = \frac{1}{\sigma} \frac{dH}{dy}$$

$$= \frac{-H_L}{2\sigma\lambda^* \sinh(t/\lambda^*)} \left\{ [e^{-t/2\lambda^*} - \eta e^{i\theta} e^{t/2\lambda^*}]e^{x/\lambda^*} + [e^{t/2\lambda^*} - \eta e^{i\theta} e^{-t/2\lambda^*}]e^{-x/\lambda^*} \right\} \quad (62)$$

Hence Eq. (22) is replaced by a generalized expression for the complex power loss,

$$P(\omega) = \frac{\hbar w}{\sigma\lambda^*} \frac{H_L^2}{\sinh(t/\lambda^*)} [(1+\eta^2)\cosh(t/\lambda^*) - 2\eta\cos\theta] \quad (63)$$

· By the definition of Eq. (20), the effective surface impedance is

$$Z_{s,eff} = \frac{p(\omega)}{\iint |H|^2 \, ds} = \frac{P(\omega)}{H_L^2 \hbar w + |H_L \eta e^{i\theta}|^2 \hbar w} = \frac{P(\omega)}{H_L^2 \hbar w (1+\eta^2)}$$

$$= \frac{1}{\sigma\lambda^*} \frac{(1 - 2\eta\cos\theta + \eta^2)\coth(t/\lambda^*) + 2\eta\cos\theta\tanh(t/2\lambda^*)}{1+\eta^2} \quad (64)$$

A similar expression only considering the difference of the magnitude was derived by Huang, et al.[24]

Let us consider Eq. (64) for three limiting situations :

(1) In the bulk limit t >> λ, $\tanh(\frac{t}{2\lambda^*})$ and $\coth(\frac{t}{2\lambda^*}) \to 1$, and Eq. (64) reduces to $Z_{s,eff} = Z_{s,bulk}$, independent of the values of χ (or η) and θ.

(2) When $\chi = 0$ (or $\eta = 1$) and $\theta = 0$ (or $\cos\theta = 1$), Eq. (64) reduces to Eq. (24), as expected.

79

(3) When $\chi = 0$ (or $\eta = 1$) and $\theta = \pi$ (or $\cos\theta = -1$), Eq. (64) reduces to $Z_{s,eff} = Z_{s,bulk}\{-\tanh(\frac{1}{2\lambda}) + 2\coth(\frac{t}{\lambda})\}$. In the normal state, it becomes $Z_{s,eff} = \frac{2}{\sigma t} - i\frac{2t}{\delta}\frac{1}{\sigma\delta}$.

Hence, when the sample thickness t is comparable with the penetration depth λ, the asymmetry of the fields may affect the measured effective surface impedance significantly.

To see which of the two effects (magnitude or phase) dominates our experiments, we shall examine each effect separately. First consider the case of a magnitude difference only ($\theta = 0$). In the normal state, Eq. (64) can be simplified with the assumption t $\ll$ δ, and be written as

$$Z_{s-eff} \cong \frac{\frac{1}{\sigma\lambda^*}\left\{2(1-\chi)\left[\frac{t}{2\lambda^*} - \frac{1}{3}\left(\frac{t}{2\lambda^*}\right)^3\right] + \chi^2\left(\frac{\lambda^*}{t} + \frac{1}{3}\frac{t}{\lambda^*}\right)\right\}}{2(1-\chi) + \chi^2}$$

$$= \frac{\frac{1}{\sigma_n\delta}\left\{i\left[\frac{2t}{\delta}(1-\chi+\frac{\chi^2}{3})\right] + \left[\frac{\chi^2\delta}{t} + \frac{1-\chi}{3}(\frac{t}{\delta})^3\right]\right\}}{2(1-\chi) + \chi^2} \quad (T>T_c) \quad (65)$$

For the symmetric field case $\chi = 0$, it reduces to Eq. (60) above. Comparing Eqs. (60) and (65), we can see the asymmetry of the magnitude of the field, which is determined by χ, can have a large effect on the surface resistance, but the surface reactance is relatively insensitive to the χ factor. To fit both $X_{s,eff}(T)$ and $R_{s,eff}(T)$ in **Figure 3.7** quantitatively, two different value of χ are required, and the values of χ are too big to be explained. **Figure 3.8** shows that values of χ of 0.2 and 0.16 are required to fit $X_{s,eff}(T)$ and $R_{s,eff}(T)$ respectively.

Next we consider the case in which only a phase difference exists between the fields on the two sides of the film ($\chi = 0$ or $\eta = 1$). Simple two-fluid model fits with a non-zero $\theta = \frac{2t}{\delta} \approx 9.7°$ and $\chi = 0$ (or $\eta = 1$) for

80
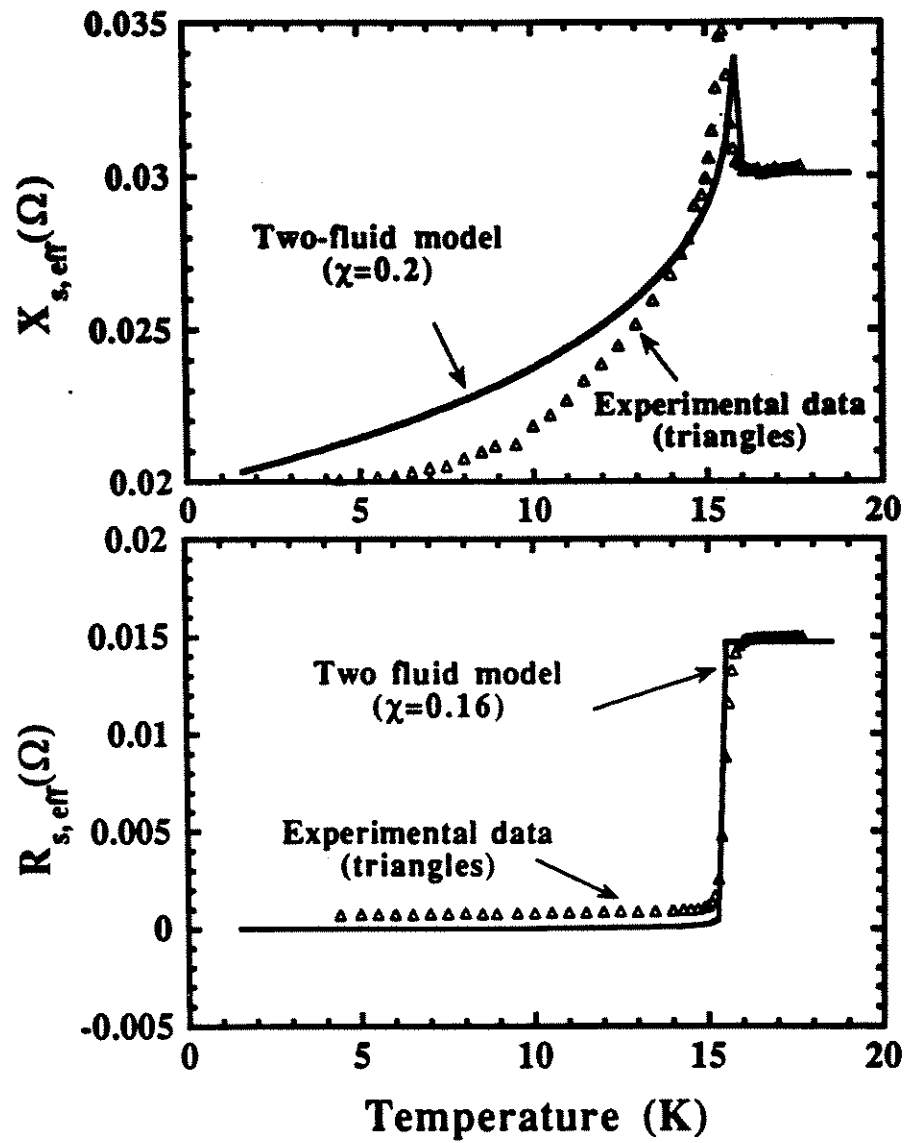
Figure 3.8

Figure 3.8 The effective surface impedance vs. temperature for a NbN thin film. The solid lines are the two-fluid model fits assuming only a magnitude difference between fields on either side of the film. Values of χ of 0.2 and 0.16 are required to fit $X_{s,eff}(T)$ and $R_{s,eff}(T)$ respectively.

both $X_{s,eff}(T)$ and $R_{s,eff}(T)$ of a NbN thin film are shown in **Figure 3.7**. The two-fluid conductivity and Eq. (64) or (65) are applied with $\lambda(0) \cong 3900\,\text{Å}$ (determined from parallel plate resonator measurements[25]) for this granular NbN film. The fits reproduce all the major features of the data quantitatively, although the exact temperature dependence below T_c requires more sophisticated BCS calculations. The value of θ is fixed by the normal state $R_{s,eff}$ and this same value of θ gives the observed peak height and normal state value of $X_{s,eff}(T)$. The asymmetry of a phase factor with $\chi = 0$ (or $\eta = 1$) actually explains all the features of the data obtained on various thin film samples.

Here is a summary of the main results of this model for the case of equal magnitudes and variable phase angle:

(1) For thin films, there will usually be a peak in the effective surface reactance $X_{s,eff}(T)$ and the range of $X_{s,\ eff}$ peaks is similar to the range of data we have on NbN, $Nd_{1.85}Ce_{0.15}CuO_4$, and $YBa_2Cu_3O_{7-\delta}$ thin films. The theory also predicts that a peak in $X_{s,eff}(T)$ is not observed for a phase angle $\theta = 0$ or in the bulk limit.

(2) There is no peak in the surface resistance $R_{s,eff}(T)$, except possibly for anisotropic materials.[19]

(3) $X_{s,\ eff}(T > T_c)$ can be smaller than $X_{s,\ eff}(T = 0)$, while $R_{s,\ eff}(T > T_c)$ can be bigger or smaller than $R_{s,\ bulk}$, depending on θ.

(4) $|X_{s,\ eff}(T > T_c)|$ is relatively insensitive to θ, except for $\theta \to \pi$.

(5) $|R_{s,\ eff}(T > T_c)|$ scales with θ: $\theta = 0$ corresponds to the symmetric fields case and Eqs. (60) determines the surface resistance, which is reduced from

the bulk value by a factor $(\frac{t}{\delta})^3$; $\theta \to \pi$ on the other hand, will give $R_{s,eff}(T>T_c) = \frac{2\rho}{t}$, which will be bigger than the bulk value.

3-7 Conclusions

We have derived from first principles the relationship between measured quantities and the surface impedance and conductivity of superconducting samples measured by the cavity perturbation technique. Also discussed are some examples of this method applied to bulk and thin film superconductors. A set of essential requirements for the data obtained by cavity perturbation have also been set down and discussed. We believe this Chapter will clarify many of the ambiguities and contradictions found in the earlier literature on cavity perturbation with superconducting samples.

Appendix 1

Here we describe a simple alternative way to derive the complex frequency shift in terms of the integral of the Poynting vector in a perturbed resonant cavity.

For a perfectly conducting empty cavity executing a resonance mode (E_0, H_0), Maxwell's equations with harmonic time dependence give,

$$\nabla \times E_0 = i\omega_0 B_0 \tag{A1.1}$$

$$\nabla \times B_0 = -i\omega_0 \mu_0 \varepsilon_0 E_0 \tag{A1.2}$$

where E_0, B_0 are out of phase by $\pi/2$.

Consider a small perturbation to the cavity, so that

$$\nabla \times E = i\omega B \tag{A1.3}$$

$$\nabla \times B = -i\omega \mu_0 \varepsilon_0 E \tag{A1.4}$$

where ω is a complex frequency close to ω_0.

Calculating $(A1.1)^* \cdot B - E_0^* \cdot (A1.4)$, we have

$$(\nabla \times E_0)^* \cdot B - E_0^* \cdot (\nabla \times B) = -i\omega B_0^* \cdot B + i\omega \mu_0 \varepsilon_0 E_0^* \cdot E \tag{A1.5}$$

Making use of a vector identity, one finds that the left side of Eq. (A1.5) is equal to $\nabla \cdot (E_0^* \times B)$, and we get

$$\nabla \cdot (E_0^* \times B) = -i\omega B_0^* \cdot B + i\omega \mu_0 \varepsilon_0 E_0^* \cdot E \tag{A1.6}$$

Similarly, starting with Eqs. (A1.2) and (A1.3), we have

$$\nabla \cdot (E \times B_0^*) = i\omega B \cdot B_0^* - i\omega \mu_0 \varepsilon_0 E \cdot E_0^* \tag{A1.7}$$

Adding Eq. (A1.6) and Eq. (A1.7), and integrating the sum over the volume $V_0 - V_1$, and using Green's theorem, we have

$$\oiint_{S_{\text{_____}}} (E_0^* \times B) \cdot n \, dS + \oiint_{S_{\text{_____}}} (E \times B_0^*) \cdot n \, dS$$

$$= i(\omega - \omega_0) \iiint_{V_0 - V_1} (B \cdot B_0^* + \mu_0 \varepsilon_0 E \cdot E_0^*) dV \tag{A1.8}$$

As the first term on the left of Eq. (A1.8) is equal to zero,[14] we will have

84

$$\frac{\omega - \omega_0}{\omega_0} = \frac{\oiint_{S_{sample\ and\ cavity\ wall}}(E \times B_0^*) \cdot \mathbf{n}\,dS}{i\omega_0 \iiint_{V_0 \cdot V_1}(B \cdot B_0^* + \mu_0 \varepsilon_0 E \cdot E_0^*)\,dV}$$

$$\cong \frac{\oiint_{S_{sample\ and\ cavity\ wall}}(E \times B_0^*) \cdot \mathbf{n}\,dS}{i\mu_0 \omega_0 \iiint_{V_0}(B \cdot B_0^* / \mu_0 + \varepsilon_0 E \cdot E_0^*)\,dV} \qquad (A1.9)$$

Here we have assumed $V_1 \ll V_0$ and because $B_0^* = -B_0 = -\mu_0 H_0$, equation (A1.9) is the same as Eq. (9).

Appendix 2

In the TE_{011} mode of a cylindrical cavity with height L and radius R (Figure 3.1.), the resonant frequency is [15]

$$\omega_{TE_{011}} = c\sqrt{(\frac{\pi}{L})^2 + (\frac{x_{01}'}{R})^2} \qquad (A2.1)$$

while the electric and magnetic field are given by

$$E_{TE_{011}}(r,z) = \hat{\phi}\mu_0 c H_0 \sqrt{(\frac{\pi R}{x_{01}' L})^2 + 1} J_1(x_{01}' \frac{r}{R})\sin(\pi \frac{z}{L}) \qquad (A2.2)$$

$$H_{TE_{011}}(r,z) = H_0[-\hat{r}(\frac{\pi R}{x_{01}' L})^2 J_1(x_{01}' \frac{r}{R})\cos(\pi \frac{z}{L}) + \hat{z}J_0(x_{01}' \frac{r}{R})\sin(\pi \frac{z}{L})] \qquad (A2.3)$$

where $x_{01}' = 3.832 \cdots$ is the first root of the Bessel function $J_0'(x) = 0$ (or $J_1(x) = 0$) and H_0 is the field at the center of the cavity H(r = 0, z = L/2) where the magnetic field is the maximum. Calculating the time averaged energy stored in the cavity in this mode, Eq. (11),

$$2 < U >= 2 \times \frac{1}{2}\iiint_{cavity}[\mu_0|H|^2 + \varepsilon_0|E|^2]dV$$

$$= \mu_0\iiint_{cavity}|H|^2 dV = \varepsilon_0\iiint_{cavity}|E|^2 dV$$

$$2 < U >_{TE_{011}} = \mu_0 H_0^2[1 + (\frac{\pi R}{x_{01}' L})^2]\int_0^L \sin^2(\frac{\pi z}{L})dz\int_0^R J_1^2(x_{01}' \frac{r}{R})2\pi r dr$$

$$= \mu_0 H_0^2[1 + (\frac{\pi R}{x_{01}' L})^2]\pi L(\frac{R}{x_{01}'})^2\int_0^{x_{01}'} J_1^2(x)x dx$$

$$2 < U >_{TE_{011}} = \frac{\mu_0 H_0^2 V_0}{2}[1 + (\frac{\pi R}{x_{01}' L})^2]J_2^2(x_{01}') \qquad (A2.4)$$

where $V_0 = \pi R^2 L$ is the volume of the cavity, and we have use mathematical formula for the integral of the Bessel function,[23] which is

$$\frac{1}{x_{01}'^2}\int_0^{x_{01}'} xJ_1^2(x)dx = \int_0^1 xJ_1^2(x_{01}'x)dx = \frac{1}{2}J_2^2(x_{01}').$$

Because $J_2(x_{01}') = \frac{2}{x_{01}'}J_1(x_{01}') - J_0(x_{01}') = -J_0(x_{01}')$, we have Eq. (58).

In the calculation of reference [9], the expression for <U> is off by a factor of 2, which results in a reduced geometric factor, hence their estimates of surface resistance are too small by a factor 2.

Appendix 3

Here we derive the complex frequency shift for a superconductor in a perturbed resonant cavity from the view of method II.

The Maxwell's Equations are

$$B = \mu_0(H^{II} + M) \tag{A3.1}$$

$$\nabla \times B = \mu_0 J^{II} + \mu_0 \nabla \times M + \mu_0 \frac{\partial D}{\partial t} \tag{A3.2}$$

$$\nabla \times H^{II} = J^{II} + \frac{\partial D}{\partial t} \tag{A3.3}$$

$$\nabla \times E = -\frac{\partial B}{\partial t} \tag{A3.4}$$

$$\nabla \cdot B = 0 \tag{A3.5}$$

where H^{II} is the magnetic field. Compared with method I, the difference (mathematically) is that the induced J is replaced by $J = \nabla \times M$. The oscillating fields in the normal mode of the cavity, before and after the perturbation can be written as:

before (considering a perfect conducting empty cavity)

$$E = E_0 e^{i\omega_0 t} \qquad H^{II} = H_0^{II} e^{i\omega_0 t}; \tag{A3.6}$$

after (considering the finite loss due to the perturbation)

$$E = (E_0 + E_1)e^{i(\omega_0 + \delta\tilde{\omega})t} \qquad H^{II} = (H_0^{II} + H_1^{II})e^{i(\omega_0 + \delta\tilde{\omega})t}. \tag{A3.7}$$

Thus, the Maxwell's Equations give

$$\nabla \times E = \nabla \times E_0 = -i\omega_0 B_0^{II} \tag{A3.8}$$

$$\nabla \times E = \nabla \times (E_0 + E_1) = -i(B_0^{II} + B_1^{II})(\omega_0 + \delta\tilde{\omega}) \tag{A3.9}$$

Subtracting Eq. (8) from Eq.(9),

$$\nabla \times E_1 = -i[\omega_0 B_1^{II} + \delta\tilde{\omega}(B_0^{II} + B_1^{II})]. \tag{A3.10}$$

Similarly, the Maxwell's Equations give

$$\nabla \times H^{II} = \nabla \times H_0^{II} = i\omega_0 D_0 \tag{A3.11}$$

$$\nabla \times H^{II} = \nabla \times (H_0^{II} + H_1^{II}) = i(\omega_0 + \delta\tilde{\omega})(D_0 + D_1) \tag{A3.12}$$

and subtracting Eq. (11) from Eq. (12)

$$\nabla \times H_1'' = i\big[\omega_0 D_1 + \delta\tilde{\omega}(D_0 + D_1)\big] \tag{A3.13}$$

Forming a scalar product of H_0'' with Eq. (13) and of E_0 with Eq. (10)

$$H_0'' \cdot \nabla \times E_1 = -i[\omega_0 H_0'' B_1'' + \delta\tilde{\omega} H_0''(B_0'' + B_1'')] \tag{A3.14}$$

$$E_0 \cdot \nabla \times H_1'' = i[\omega_0 E_0 D_1 + \delta\tilde{\omega} E_0 (D_0 + D_1)] \tag{A3.15}$$

and adding Eq. (14) and (15), we obtain
$$H_0'' \cdot \nabla \times E_1 + E_0 \cdot \nabla \times H_1'' =$$
$$i\omega_0(E_0 D_1 - H_0'' B_1'') + i\delta\tilde{\omega}[E_0(D_0 + D_1) - H_0''(B_0'' + B_1'')] \tag{A3.16}$$

Apply the vector identity
$$\nabla \cdot (H_0'' \times E_1 + E_0 \times H_1)$$
$$= E_1 \cdot \nabla \times H_0'' + H_1'' \cdot \nabla \times E_0 - H_0'' \cdot \nabla \times E_1 - E_0 \cdot \nabla \times H_1'' \tag{A3.17}$$

for the left hand side of Eq. (16), we have
$$i\omega_0(E_1 D_0 - H_1'' B_0'') - \nabla \cdot [H_0'' \times E_1 + E_0 \times H_1''] =$$
$$i\omega_0(E_0 D_1 - H_0'' B_1'') + i\delta\tilde{\omega}[E_0(D_0 + D_1) + H_0''(B_0'' + B_1'')] \tag{A3.18}$$

Integral Eq. (18) over the volume V_0:
$$i\omega_0 \int_{V_0}(E_1 D_0 - H_1'' B_0'')dV - \int_{V_0} \nabla \cdot [H_0'' \times E_1 + E_0 \times H_1''] =$$
$$i\omega_0 \int_{V_0}(E_0 D_1 - H_0'' B_1'')dV + i\delta\tilde{\omega} \int_{V_0}[E_0(D_0 + D_1) - H_0''(B_0'' + B_1'')]dV \tag{A3.19}$$

With following assumptions,

1) The "$i\omega_0$" integral give nearly zero contribution outside of V_1.

2) The divergence integral gives zero.

3) Neglect D_1, B_1 with reference to D_0 and B_0 in the "$i\delta\tilde{\omega}$" integral.

Eq. (A3.19) can be reduced to
$$i\omega_0 \int_{V_0}(E_1 D_0 - H_1'' B_0'')dV =$$
$$i\omega_0 \int_{V_0}(E_0 D_1 - H_0'' B_1'')dV + i\delta\tilde{\omega} \int_{V_0}[E_0 D_0 - H_0'' B_0'']dV \tag{A3.20}$$

or in a simpler form

88

$$\frac{\delta \tilde{\omega}}{\omega} = \frac{\int_{V_0} [(E_1 D_0 - E_0 D_1) - (H_1^{II} B_0^{II} - H_0^{II} B_1^{II})] dV}{\int_{V_0} [(E_0 D_0 - H_0^{II} B_0^{II})] dV} \qquad (A3.21)$$

Now let us write B^{II} in terms of only H^{II}, M in Eq. (21),

$$H_1^{II} B_0^{II} - H_0^{II} B_1^{II} =$$

$$\mu_0 H_1^{II} (H_0^{II} + M_0) - \mu_0 H_0^{II} (H_1^{II} + M_1) = \mu_0 H_1^{II} M_0 - \mu_0 H_0^{II} M_1$$

Therefore

$$\frac{\delta \tilde{\omega}}{\omega} = \frac{\int_{V_1} [(E_1 D_0 - E_0 D_1) + \mu_0 H_0^{II} M_1 - \mu_0 H_1^{II} M_0)] dV}{\int_{V_0} [(E_0 D_0 - H_0^{II} B_0^{II})] dV} \qquad (A3.22)$$

Let us consider the approach of method II for a superconducting slab inside a uniform magnetic field and calculate the field distribution and magnetization. The induced current J in method I is replace by $J = \nabla \times M$. See **Figure 3.9 (a)**. As the applied external current is zero, $\nabla \times H^{II} = 0$ inside the slab. Thus it can readily be seen that H^{II} is constant in the slab. Since the magnetic field is continuous at the boundaries, it should be uniform throughout the region. The magnetization can be calculated from the know current distribution of method I, although it is not easy to be calculated otherwise. Thus from Eq. (16) and Eq. (19), we get

$$M_z(y) = H_0^{II} \left(\frac{\cosh(y/\lambda)}{\cosh(t/\lambda)} - 1 \right) \qquad (A3.23)$$

Then, by using Eq. (A3.1), we obtain the magnetic field B with the same values as in method I:

$$B_z(y) = \mu_0 H_0 \frac{\cosh(y/\lambda)}{\cosh(t/\lambda)} \qquad (A3.24)$$

The magnetization given by Eq. (A3.23) depends on position in the slab (see **Figure 3.9 (b)**).

In Eq. (A3.22), for the sample in the hot-finger technique, $M_0 = 0$ and M_1 is given by Eq. (A3.23). E_0 and D_0 are considered to be zero inside the V_1. The resonant frequency shift is determined by

$$\frac{\delta\omega}{\omega} = \frac{\int_{V_1} \mu_0 H_0{}'' M_1 \, dV}{\int_{V_0} (E_0 D_0 - H_0{}'' B_0{}'')]dV} \tag{A3.25}$$

If we consider a position-dependent relative permeability μ_r by define

$$\mu_r(r) = \frac{H+M}{H} \tag{A3.26}$$

we come to the result of Waldron's [10].
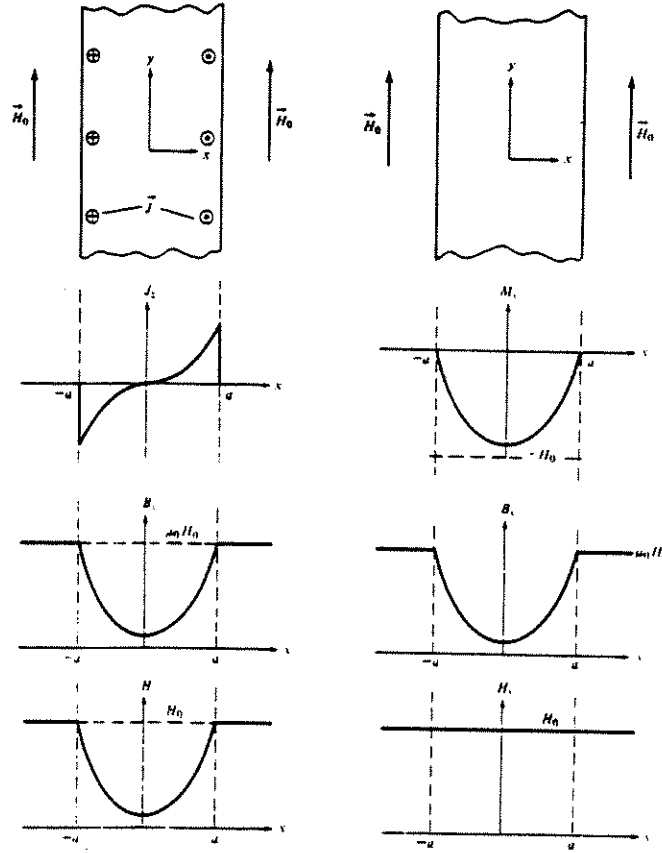
Figure 3.9   Two different ways of treating a superconductor. (a) Supercurrent are induced, no magnetization (method I); (b) Magnetization represents the Meissner effect, no supercurrent (method II).

References

[1] J. Mao, D. H. Wu, J. L. Peng, R. L. Greene and Steven M. Anlage, Phys.Rev. B *Rapid Communication* **51**, 3316 (1995); D. H. Wu, Jian Mao, S. N. Mao, J. L. Peng, X. X. Xi, T. Venkatesan, R. L. Greene and S. M. Anlage, Phys. Rev. Lett. **70**, 85(1993).

[2] T. Shibauchi, *et al.*, Phys. Rev. Lett. **72**, 2263 (1994).

[3] O. Klein *et al.*, Int. J. Infrared and Millimeter Waves **14**, 2423 (1993), and papers following.

[4] N. Klein *et al.*, J. Supercond. **5**, 195 (1992).

[5] D. A. Bonn, D. C. Morgan and W. N. Hardy, Rev. Sci. Instrum. **62**, 1819 (1991).

[6] D. L. Rubin *et al.*, Phys. Rev. B **38**, 6538 (1988).

[7] S. Sridhar and W. L. Kennedy, Rev. Sci. Instrum. **59** , 531 (1988).

[8] N. Exon *et al.*, IEEE Trans. Appl. Supercond. **3**, 1442 (1993).

[9] W. L. Kennedy, Ph. D. Thesis, Northeastern University , 1990.

[10] R. A. Waldron, Proc. IEE **107C**, 272 (1960).

[11] M. E. Brodwin and M. K. Parsons, J. Appl. Phys. **36**, 494 (1965).

[12] T. Van Duzer and C. W. Turner, "Principles of Superconductive Devices and Circuits", Section 6.05, Elsevier North Holland, Inc. (1981).

[13] In Waldron's paper, the formula (Eq. (14)) for the resonant frequency shift is $\dfrac{\delta\omega}{\omega} = \dfrac{\oiiint_{V_1}[(\boldsymbol{E}_1 \cdot \boldsymbol{D}_0 - \boldsymbol{E}_0 \cdot \boldsymbol{D}_1) - (\boldsymbol{H}_1 \cdot \boldsymbol{B}_0 - \boldsymbol{H}_0 \cdot \boldsymbol{B}_1)]dV}{\oiiint_{V_0}(\boldsymbol{E}_0 \cdot \boldsymbol{D}_0 - \boldsymbol{H}_0 \cdot \boldsymbol{B}_0)dV}$. This formula applies to materials, defined by Eqs. (4) and (5) of our paper, which do not induce currents (non conducting), such as dielectric materials,

ferittes or superconductors under method II, but can not apply to conductive materials such as superconductors under method I. The reason for this is that when Waldron evaluates the divergence integral by Green's theorem, the volume V_0 has to be divided into two regions, V_1 and V_0-V_1. The integral on the surface of volume V_1, which is pointing out of the sample, and the integral on the inner surface of V_0 - V_1, which is pointing into the sample, do not cancel each other when there is a current flowing on the sample surface (in other words, there is an energy flow at the sample surface which can be calculated through the Poynting vector). These two surface integrals cancel out for non-conducting materials, which is why it is correct in Waldron's case (method II).

[14] As $n \times E_0 \big|_{surface} = 0$ for a perfect conductor, we

have $(E_0 \times H) \cdot n = H \cdot (n \times E_0) = 0$ at the surface of the wall or sample.

[15] J. D. Jackson, "Classical Electrodynamics", second edition, section 8.7 and 8.8, Johns Wiley & Sons, Inc. (1975).

[16] S. M. Anlage, D. H. Wu, Jian Mao, S. N. Mao, X. X. Xi, T. Venkatesan, J. L. Peng and R. L. Greene, Phys. Rev. B **50**, 584 (1994).

[17] Often in the literature the surface impedance $Z_s = R_s + iX_s$ is defined as

$$Z_s = \frac{E_{\parallel}}{n \times H_{\parallel}} \text{ or } Z_s = \sqrt{\frac{i\omega\mu}{\sigma}}$$

where the unit vector n is defined as normal to the element of S_{sample} pointing outward from the sample, and $E_{\parallel}$ or $H_{\parallel}$ are the tangential components of the field on the surface. But it is not clear that this definition can be directly applied to a superconductor with $R_s \propto 1/Q$ and $X_s = \mu_0 \omega \lambda \propto \omega$.[7][9][21] It can be easily verified that this definition

92

is consistent with the power loss definition for a normal conductor occupying half of the infinite space with a uniform field applied on one side. Considering Eqs. (9) and (10), and the fact that the ratio of the electric field and magnetic field normally does not depend on position, we know it is also consistent with the definition of Eq. (20). As the total measured complex loss, which is related to the quality factor and resonant frequency, depends on the area of the sample where the field is applied and the field distribution itself, in a lot of measurements, such as the hot finger technique, what we measure is $Z_{s\text{-eff}}$ defined by Eq. (20). Hence the relation $X_s = \mu_0 \omega \lambda \propto \omega$ is not correct in general without the correction term (see Eq. (24)).

[18] H. Ning, H. Duan, P. D. Kirven, A. M. Hermann, and T. Datta, J. Supercond. **5**, 503 (1992).

[19] E. Gough and N. J. Exon, Phys. Rev. B **50**, 488(1994).

[20] H. Ning, Ph.D. Thesis, University of South Carolina, 1991.

[21] M. Portis, D. W. Cooke, and E. R. Gray, J. Supercond. **3**, 297 (1990).

[22] A. Bonn, *et al.*, Phys. Rev. B **47**, 11314 (1993).

[23] I. S. Gradshteyn and I. M. Ryzhik, "Table of Integrals, Series, and Products", 4th Edition, Academic Press, Inc. (1980).

[24] M. X. Huang, S. M. Bhagat, A. T. Findikoglu, T. Venketesan, M. A. Manheimer and S. Tyagi, Physica C **193**, 421 (1992).

[25] M. S. Pambianchi, Steven. M. Anlage, E. S. Hellman, E. H. Hartford, Jr., M. Burns and S. Y. Lee, Appl. Phys. Lett. **64**, 246 (1994).

CHAPTER 4

MATERIAL PREPARATION AND CHARACTERIZATION

High quality $Nd_{1.85}Ce_{0.15}CuO_{4-y}$ (NCCO) and $YBa_2Cu_3O_{7-\delta}$ (YBCO) single crystals and high quality NCCO thin films were made at the Center for Superconductivity Research. By working with microwave characterization interactively with sample fabrication method, we improved the fabrication techniques to obtain high quality samples. As a result, the microwave properties of the materials were improved dramatically, in the sense of higher T_c, sharper transition and lower surface resistance R_s. In this Chapter, we describe the fabrication of NCCO and YBCO single crystals and thin films and present characterization results on these materials.

4-1   NCCO Crystals and Films Fabrication and Characterization

The so called electron-doped (n-type) superconductors $R_{2-x}Ce_xCuO_{4-y}$ (R = Nd, Pr, Sm, Eu) single crystals were grown using a directional solidification technique, which employs a stationary crucible in a strong vertical temperature gradient (~20°C/cm) inside a box furnace.[1] To make NCCO single crystals, high purity oxide $Nd_{2-x}Ce_xCuO_{4-y}$ compound and excess CuO powder are mixed first. Because of the high melting point of $Nd_{2-x}Ce_xCuO_{4-y}$ compound, CuO was added as a flux to the compound to lower the melting temperature. About 50 wt% of CuO flux was added. The crucibles used are made of Al_2O_3, ZrO_2 and Pt. All of them were reacted

with the melt, especially at high temperatures. The Al_2O_3 crucibles were the least reactive and hence were chosen for the NCCO crystal fabrication. A typical temperature program for a successful growth is listed in **Figure 4.1**. The optimum growth parameters varies with Ce concentration. At the end of the growth experiment, the flux was allowed to flow out of the crucible, so that only the free standing crystals were left in the bottom of the crucible. The as-grown NCCO crystals are non-superconducting. So we annealed the as-grown NCCO crystal in a reduced atmosphere to remove excessive oxygen. In order to produce homogeneous superconducting NCCO crystals, the annealing was carried out in an inert gas atmosphere, such as pure argon, at 850°C for at least one day. The change in oxygen content during annealing was determined by thermogravimetric analysis using a Dupont 951 TGA system.[2] Oxygen loss was observed at temperatures above 770 °C, which is a rather high temperature in comparison with those for other cuprate oxide superconductors. The oxygen deficiency could not be measured but similar annealing conditions typically produce $y \approx 0.03$-0.05 in ceramic $R_{2-x}Ce_xCuO_{4-y}$.[2] The stoichiometry and sample homogeneity were determined by wavelength dispersive spectroscopy, using a JEOL JXA-840A electron microscope. The experimental uncertainty for each cation is approximately $\pm$ 0.02. Within the instrumental accuracy, no other element besides Nd, Ce, Cu and Al was detected. The Al impurity was due to the reaction with the crucibles, and was close to the detection limit (< 0.5%). Energy dispersive x-ray analysis (EDX) measurements done on many crystals reveal that the Ce distribution is quite uniform within the experimental accuracy (~0.01). The Ce
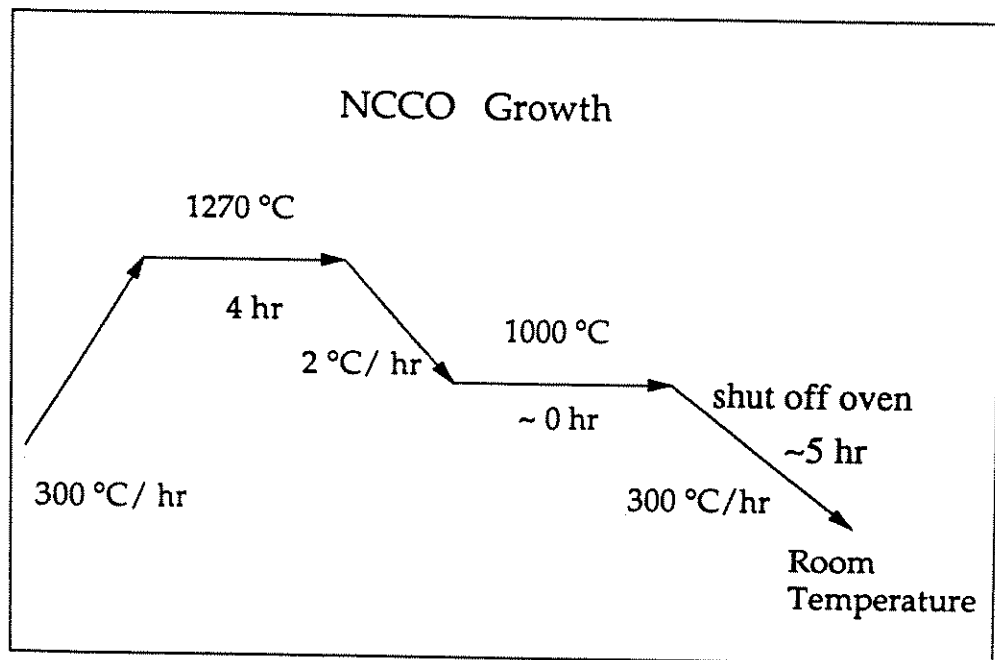
Figure 4.1   A typical temperature program for NCCO crystal growth.

homogeneity along the c-axis in thin crystals is also revealed by an optical study combined with EDX on similarly prepared thick crystals which shows that the Ce distribution is uniform with layers of about 20~25 μm.[3] The composition of the NCCO crystals used for microwave measurements are $Nd_{1.85}Ce_{0.15}CuO_{4-y}$.

X-ray diffraction on powdered NCCO crystals show the tetragonal T' 2-1-4 structure with no impurity phases present. The lattice parameters were determined from the peak value of 2θ by indexing to a tetragonal Nd_2CuO type structure.[4] The c-axis lattice parameter (c) and the unit cell volume decrease with increasing Ce concentration while the a-axis parameter (a) shows little change, indicating Ce_{4+} (r = 0.97 Å) substitution for Nd_{3+} (r = 1.12 Å).

Bulk superconductivity with $T_c \approx$ 23-24 K in NCCO crystals are determined by dc magnetization and also by dc resistivity measurements. The transition width (10% ~ 90%) is < 0.5 K, indicating high quality. **Figure 4.2** shows the dc magnetization vs. temperature for a superconducting NCCO single crystal. **Figure 4.3** is the dc resistivity data for a superconducting NCCO single crystal showing $T_c \approx$ 24 K with transition width less than 0.5K.

The pulsed laser deposition (PLD) method were chosen for NCCO film fabrication because it reproduces the target composition in the films. This is important because superconductivity in $Nd_{2-x}Ce_xCuO_{4-y}$ occurs only in a very narrow Ce concentration range near x = 0.15. The films are deposited on single crystals of perovskite type substrates such as $(100)SrTiO_3$, $(100)LaAlO_3$, (100) $NdGaO_3$, and fluorite-type substrates such

Figure 4.2   Dc magenetization vs. temperature for a NCCO single crystal.

Dc Resistivity of a NCCO Crystal
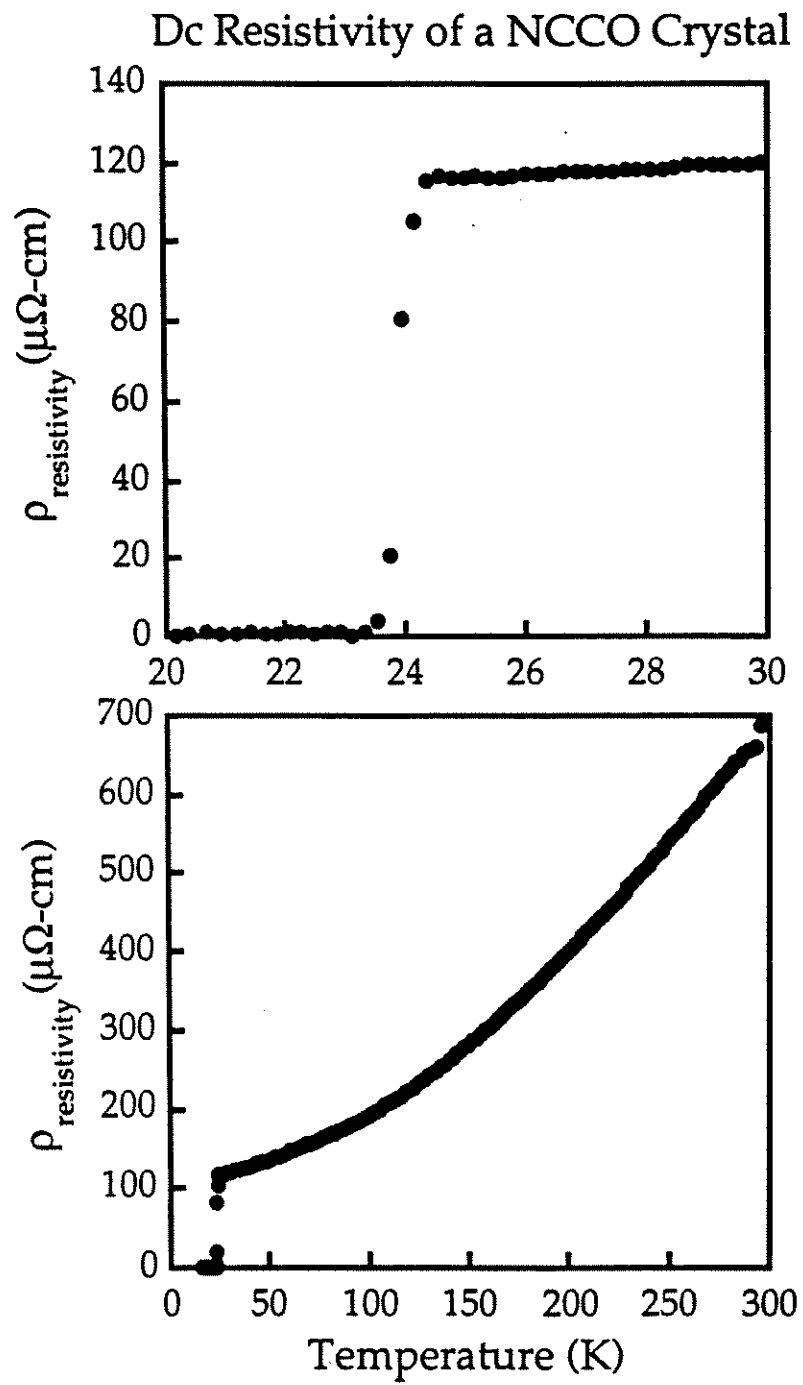
Figure 4.3   Dc resistivity for a NCCO single crystal.

as Y_2O_3 stabilized ZrO_2 (YSZ) at a substrate temperature of 800 °C in a 200 mTorr N_2O ambient at a deposition rate of 0.3Å/pulse and a repetition rate of 10 Hz. After the deposition, the films are either cooled down to room temperature in 200 mTorr N_2O, or cooled with the chamber being evacuated to 10^{-5} Torr and maintained at the deposition temperature in the vacuum for different time periods. Different film thicknesses require different optimum reduction conditions. The films were then characterized for structural and superconducting properties using x-ray diffraction, dc resistance, and ac susceptibility measurements. Careful microstructure analysis with x-ray diffraction, and both plan-view and cross-sectional transmission electron microscopy, reveal that the NCCO grains crystallize with the c-axis normal to the substrate. The only impurity phase detected was $Nd_{0.5}Ce_{0.5}O_{1.75}$ (NCO), a cubic insulating material. NCO is present in grain sizes of a few hundred angstroms at about the 1 to 2 volume % level in the highest quality thin films.[7]

A typical θ-2θ X-ray diffraction shows that the film is highly oriented with c-axis perpendicular to the substrate surface. A small amount of $Nd_{0.5}Ce_{0.5}O_{1.75}$ (NCO) phase (<2%) is found in some of the films from transmission electron microscopy (TEM) studies. A small fraction of a-axis oriented grains was observed only in films grown on LAO substrates, possibly because of the lattice mismatch between the substrate and the thin film.[7]

In general, the superconducting transition temperature is about $T_c \approx$ 22.4 K for a film thicker than 3000 Å. The film quality can be optimized through vacuum annealing at temperatures slightly lower than the
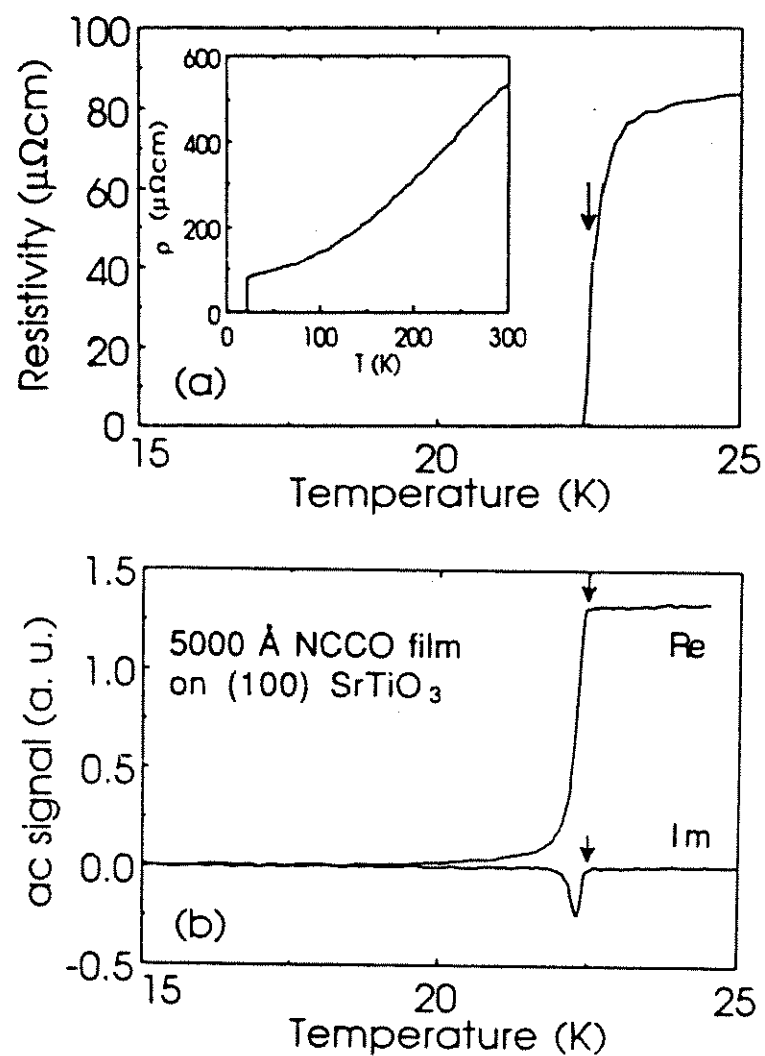
Figure 4.4   Dc resistivity vs. temperature and the ac susceptibility results for a NCCO film made under optimal conditions.

deposition temperature. **Figure 4.4** presents the dc resistivity vs. temperature and the ac susceptibility results for a film made under optimal conditions, showing a T_c (resistance = 0) of 22.4 K with a transition width of 0.2 K. The ratio of room temperature resistance to the residual resistance is over 6 with a residual resistivity of 80 $\mu\Omega$cm.[6] For 4000Å thick NCCO thin films on STO and YSZ substrate, Rutherfeld Back Scattering (RBS) channeling yields (χ_{min}) are 11.5% and 11% respectively, as shown in **Figure 4.5.**[6] The values are fairly larger than that of YBCO samples which could be as low as 3%. This may be due to the difference of the lattice perfection between the two systems. It may also be an indication of greater disorder in the NCCO system, due to the random substitution of C_e for N_d.

Both thin films and single crystals show a sharp transition ($\leq$ 0.2 K wide in AC susceptibility or in a dc SQUID characterization) at $T_c \sim$ 21-22 K. However, while the initially fabricated nominal crystals show no evidence of the NCO impurity phase, the crystals showed evidence of multiple superconducting transitions when studied at microwave frequencies. We found that NCCO samples showing a single transition in dc resistivity measurements showed multiple transitions in microwave measurements. A procedure was developed to remove the surface layers of the crystals by means of mechanical polishing, chemical etching, and re-annealing, to eliminate inhomogeneous layers. It was found that several such treatments were required to obtain single-phase response and low residual losses at microwave frequencies. After the polishing and annealing treatments, the single crystals were about 2 × 2 mm^2 with a thickness of approximately 20 μm. Through interactive collaboration with thin film
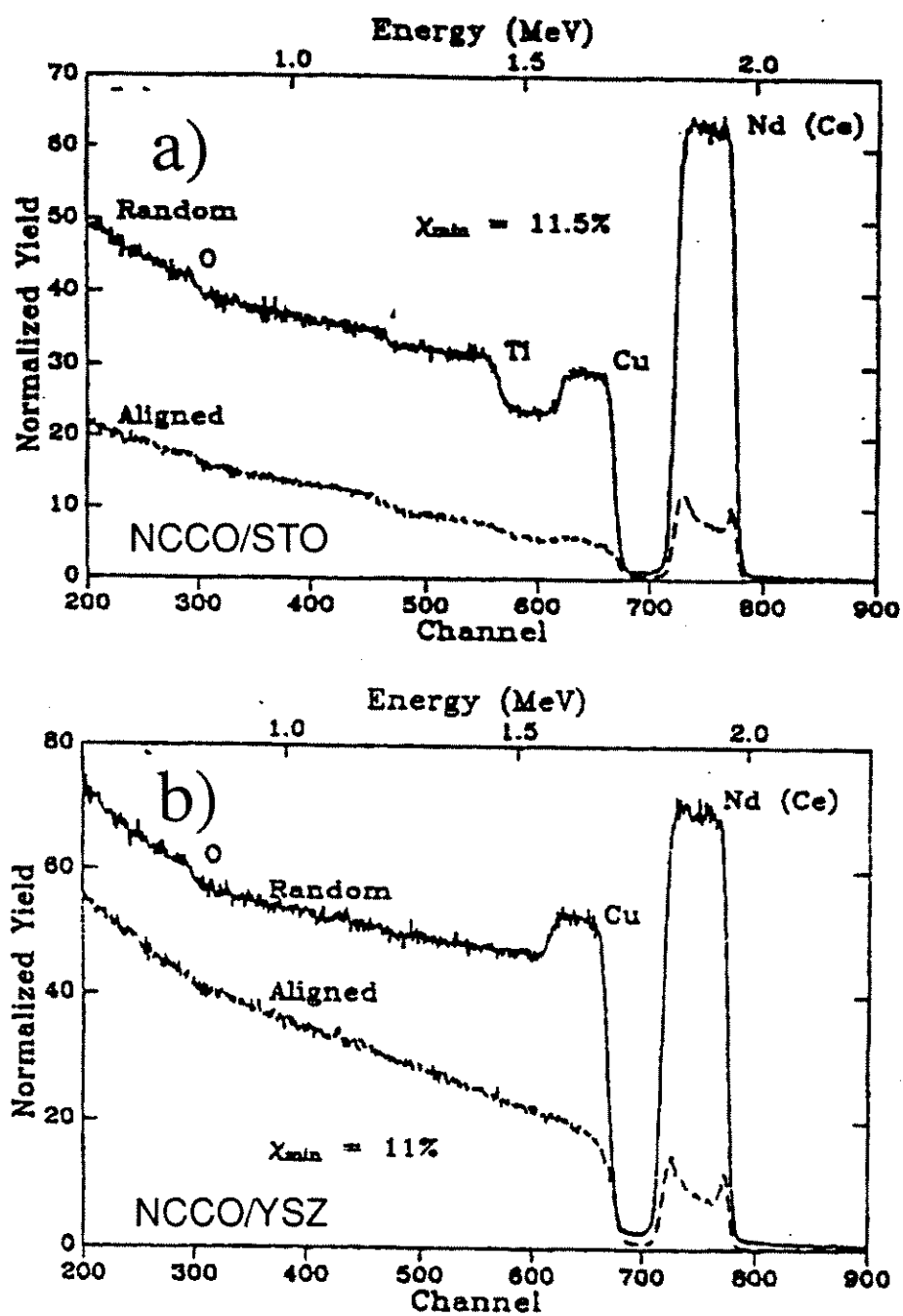
Figure 4.5   RBS channeling yield for a NCCO thin film made on STO and a thin film made on YSZ substrate.

fabrication group, films with a sharp single transition, high T_c and low surface resistance were fabricated. **Figure 4.6 (a)** is the dc magnetization data for an as-grown and argon annealed NCCO crystal. **Figure 4.6 (b)** is the result of microwave characterization for this NCCO crystal. Clearly, one can find multiple transitions in **Figure 4.6 (b)**, although the dc magnetization shows only a single transition. **Figure 4.6 (c)** is the results of microwave characterization for an initially fabricated NCCO film. It shows a broad transition, although low frequency ac susceptibility and dc resistivity measurement on films made under similar conditions show only one fairly sharp transition. **Figure 4.7 (a)** is the dc magnetization data for this NCCO crystal after we performed the improvement procedure discussed above. The transition width is about the same. **Figure 4.7 (b)** is the results of microwave characterization for this improved NCCO crystal, showing only one single transition. **Figure 4.7 (c)** is the results of microwave characterization for an improved NCCO film. The improvement over **Figure 4.7 (c)** is dramatic: the new film has a single sharp transition with a much high transition temperature.

4-2 YBCO Crystals

The YBCO crystals are grown by a self-flux method.[8] A mixture of stoichiometric $BaCO_3$, CuO and Y_2O_3 powders are prereacted to form the $YBa_2Cu_3O_7$ phase. The product is then mixed with the appropriate amount of flux (BaO and CuO) and melted at 980 C in a ZrO_2 crucible, followed by slow cooling to room temperature. We verified by x-ray diffractometry that the as-grown crystals are single phase, and then annealed the crystals in

Dc magnetization data
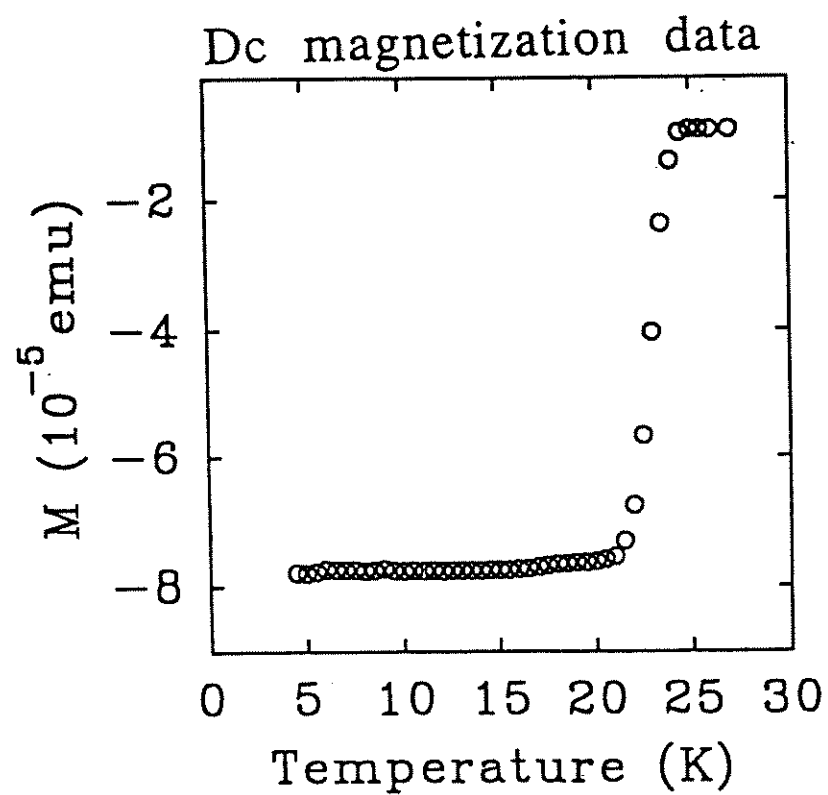
Figure 4.6 (a)   Dc magnetization for a as-grown and argon annealed
NCCO crystal. It shows a single relatively sharp transition.
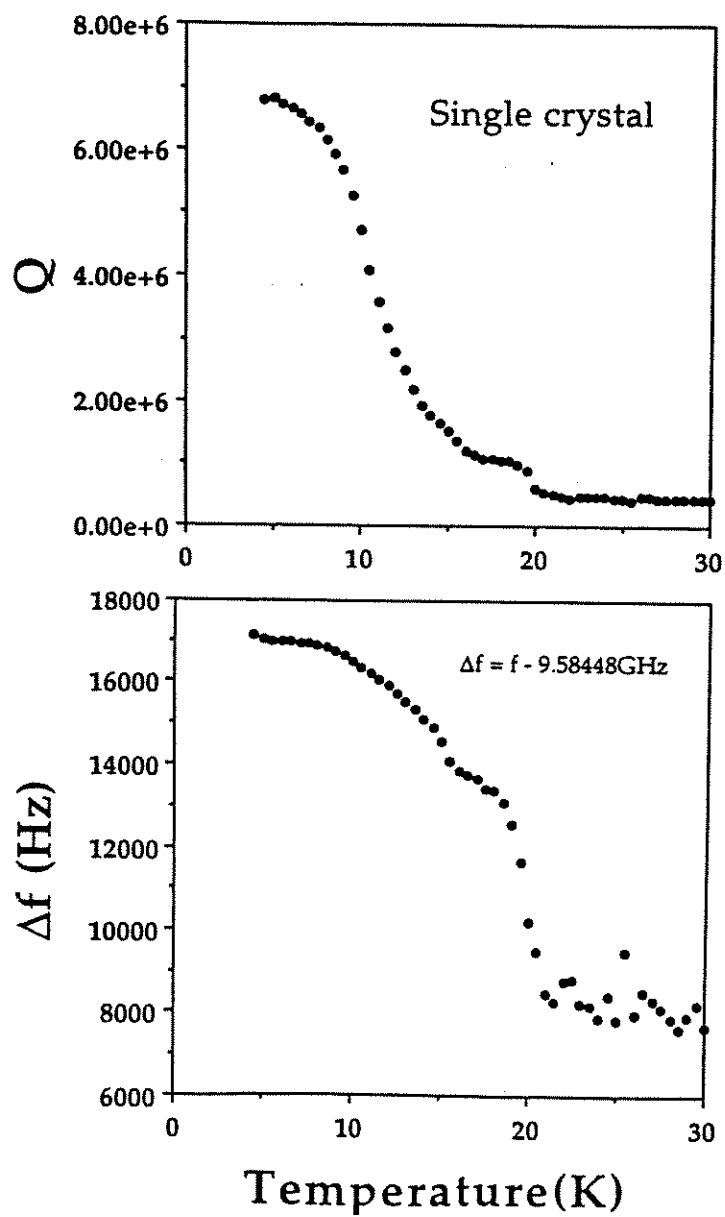
Figure 4.6 (b)   The microwave characterization results ($Q \propto -1/R_s$ and $\Delta f \propto -\Delta \lambda$) for this crystal, showing multiple transitions, although the dc magnitization data shows only one single transition.

106
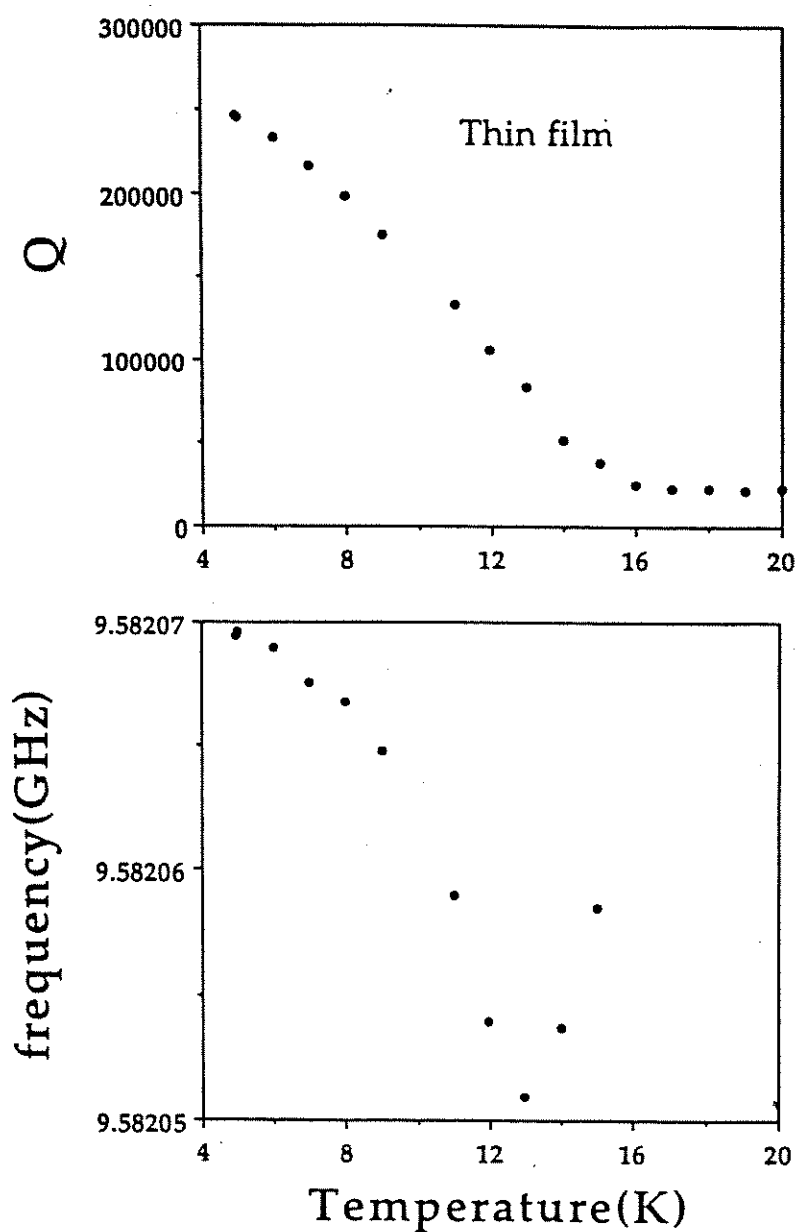
Figure 4.6 (c)   Microwave characterization for an early NCCO thin film. It shows a broad transition, although low frequency ac susceptibility and dc resistivity measurement on films made under similar conditions show only one fairly sharp transition.

107

Dc magnetization data
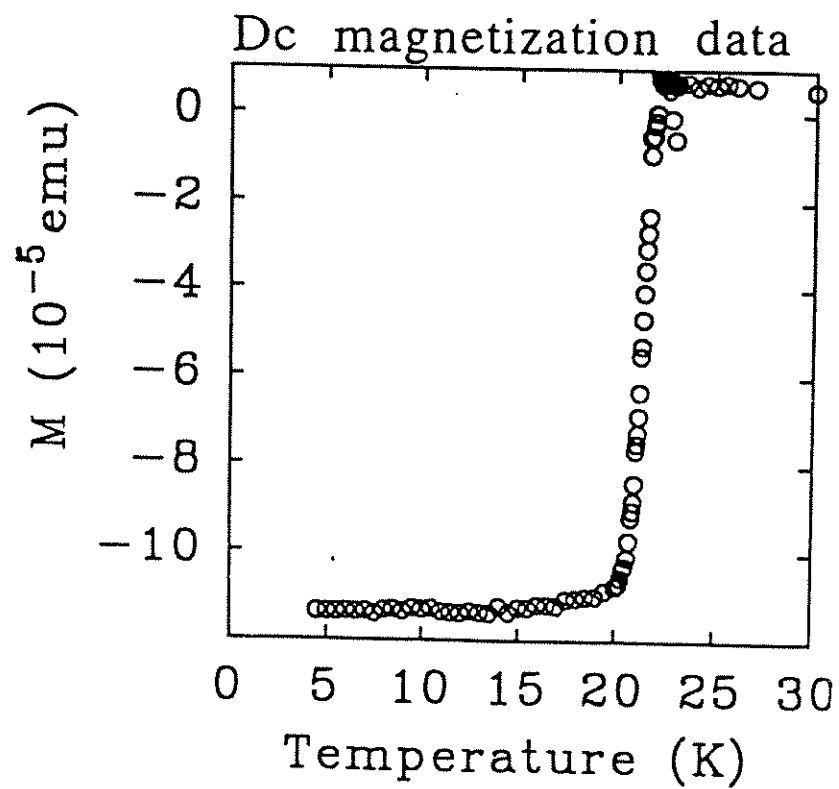
Figure 4.7 (a)   Dc magnetization for the improved NCCO crystal. It also shows a single sharp transition.

108
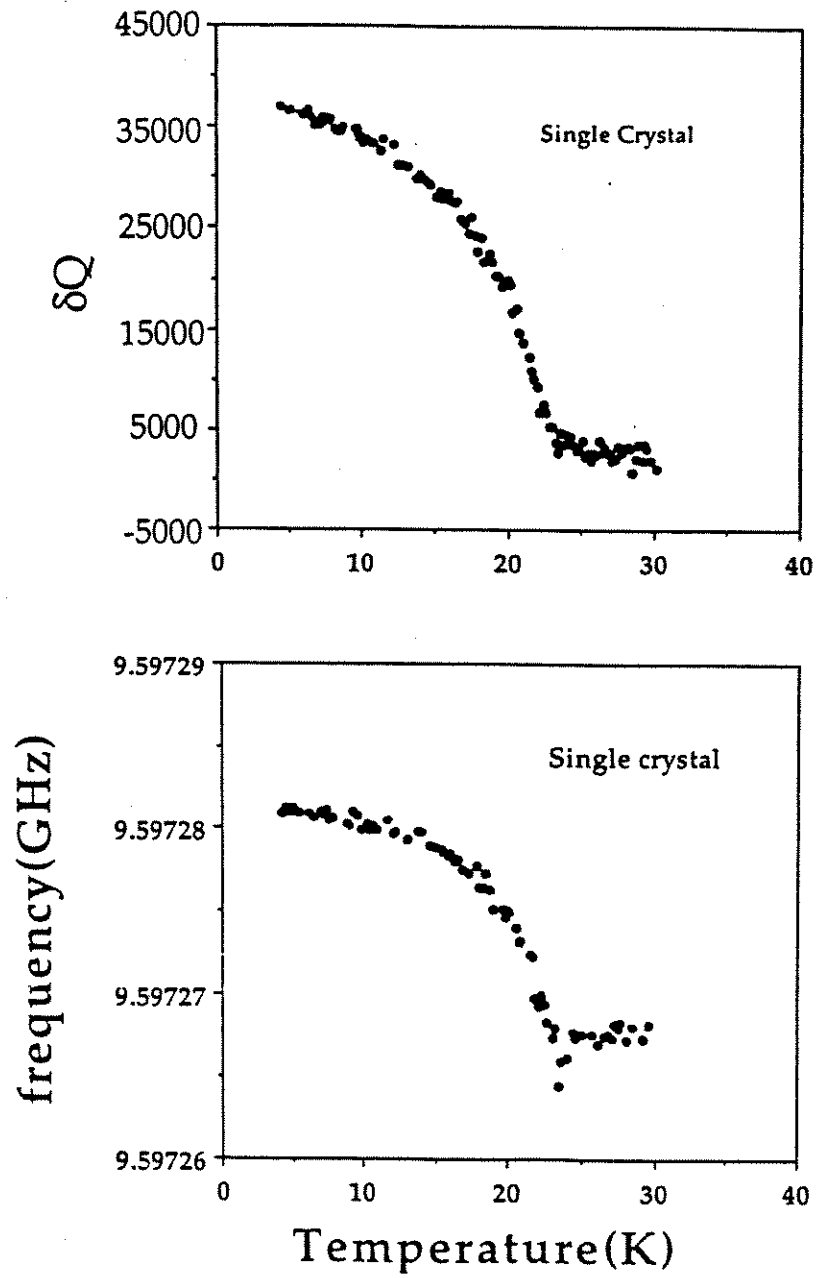
Figure 4.7 (b)   The microwave characterization results of this improved NCCO crystal. It shows a single transition.
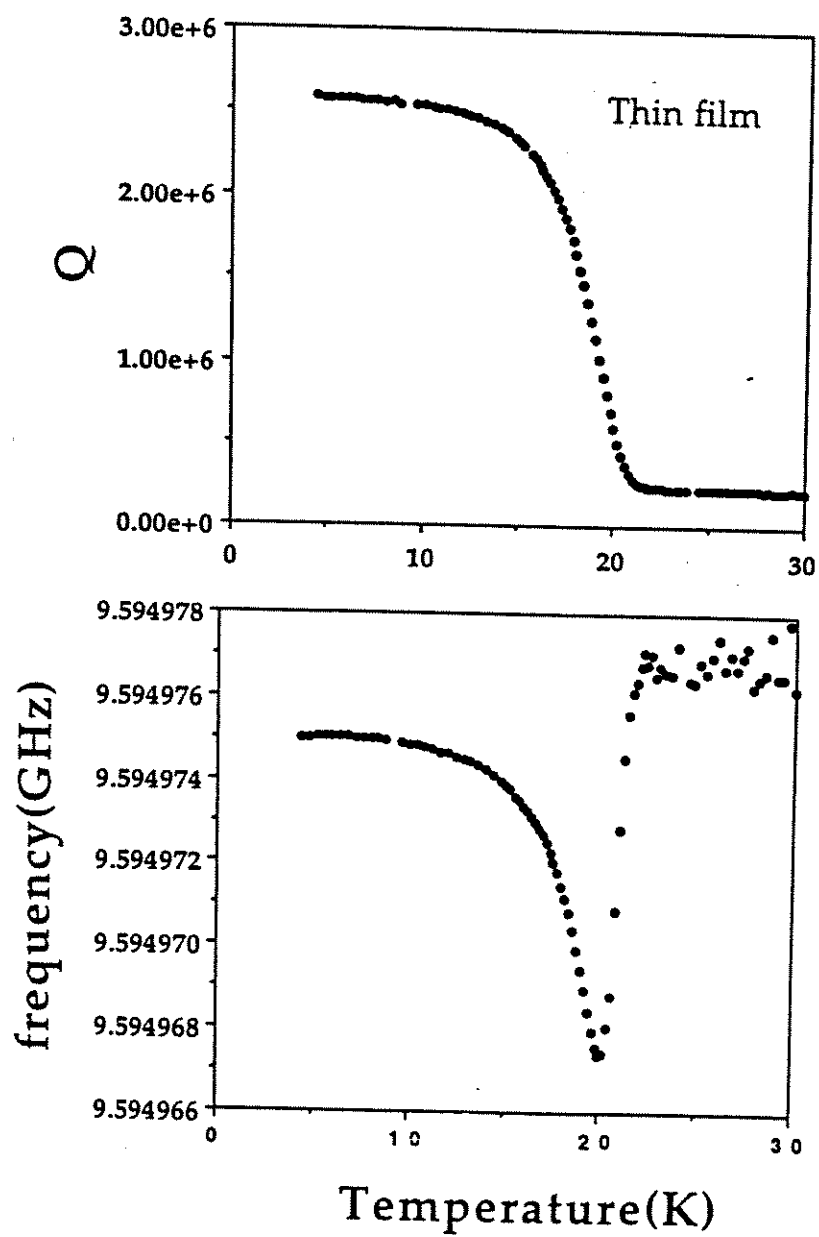
Figure 4.7 (c) Microwave characterization for an improved NCCO thin film. It shows a sharp transition.
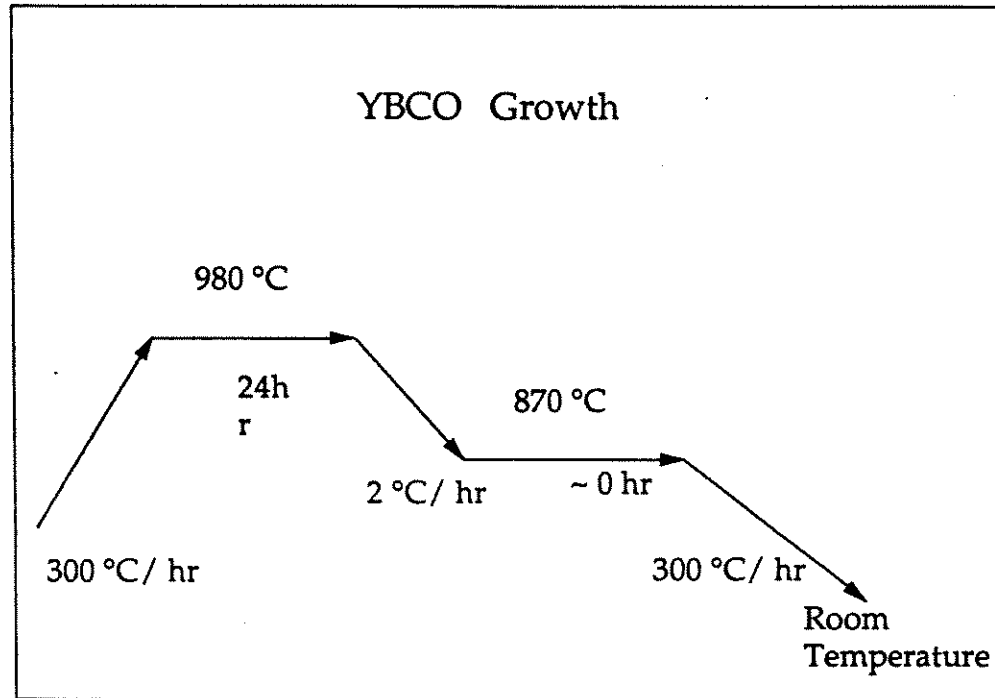
Figure 4.8   The temperature program for YBCO single crystal growth.

111

flowing oxygen at 450 C for at least two weeks. **Figure 4.8** shows the temperature program for YBCO crystal growth. The crystals typically show zero resistance at 92-93 K in dc resistivity measurements. Ac susceptibility and dc magnetization measurements also confirm the transition temperature to be 92-93 K with the transition width less than 0.25 K for most of the high quality YBCO crystals. **Figure 4.9** is the dc resistivity result. **Figure 4.10** is the magnetization data. The 10%-90% transition width, ΔT_c, is less than 0.3 K, indicating very high quality. **Figure 4.11** shows the ion channeling angular scans of the YBCO crystal taken with 1.5 Mev He+ ions. The crystal is first aligned in such a way that the incident ion beam is along the [001] direction. The angular scan is taken across the [001] axial direction. Two such scans are presented here. One taken above Tc at 100 K and the other below T_c at 80 K, with the same crystal. The quality of the channeling dips with a minimum yield about 3% indicating a very good quality of the YBCO single crystals. A clear change of ~ 7% in the FWHM is seen across T_c has been indicated earlier.[9]

For our microwave measurements, we chose samples with minimum twinning and smooth shiny surfaces with typical crystal sizes of about 1 mm x 1 mm x 15-25 μm. The normal state resistivity at 100 K is about 40-50 μΩcm by dc measurement, similar to that of the Illinois crystals[10] and substantially less than ~ 70 μΩcm of the UBC group.[11]

As a summary, we have improved the quality of NCCO samples dramatically. Both single crystals and thin films show a single sharp transition with T_c above 21 K for dc resistivity, AC susceptibility, dc magnetization and microwave surface impedance characterization.

112
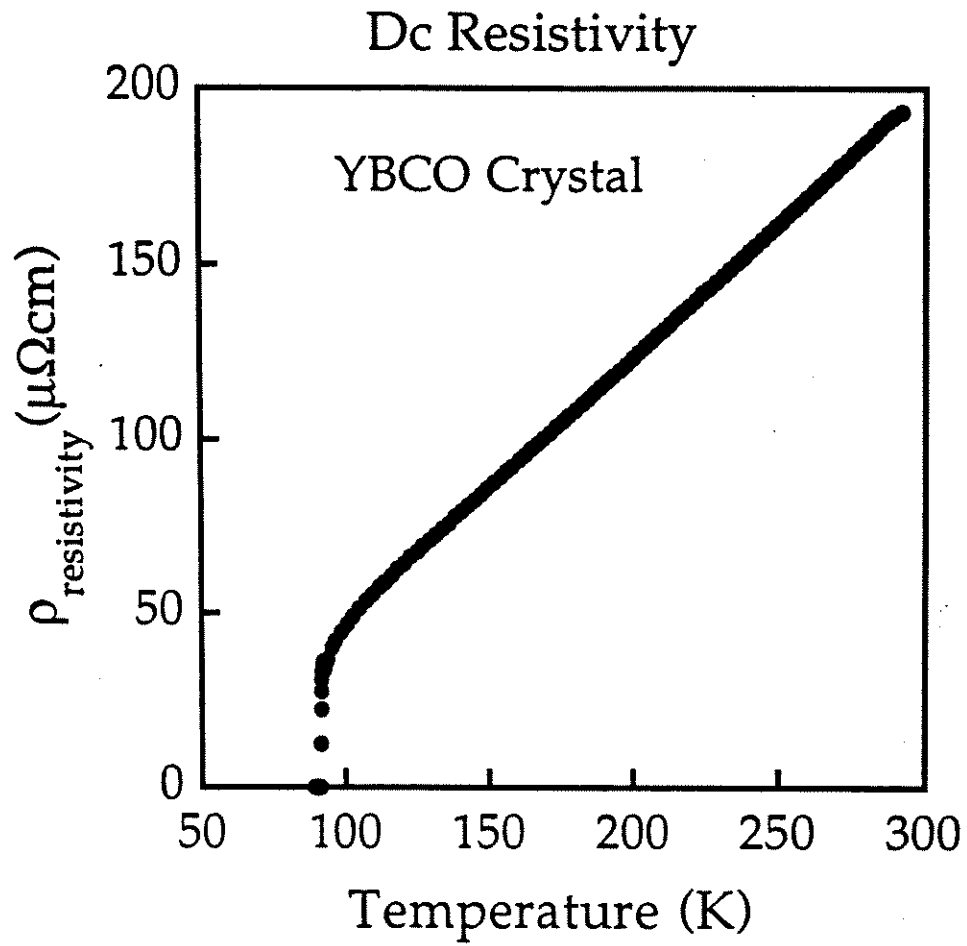
Dc Resistivity

Figure 4.9   Dc resistivity for a YBCO single crystal.

Dc Magenetization
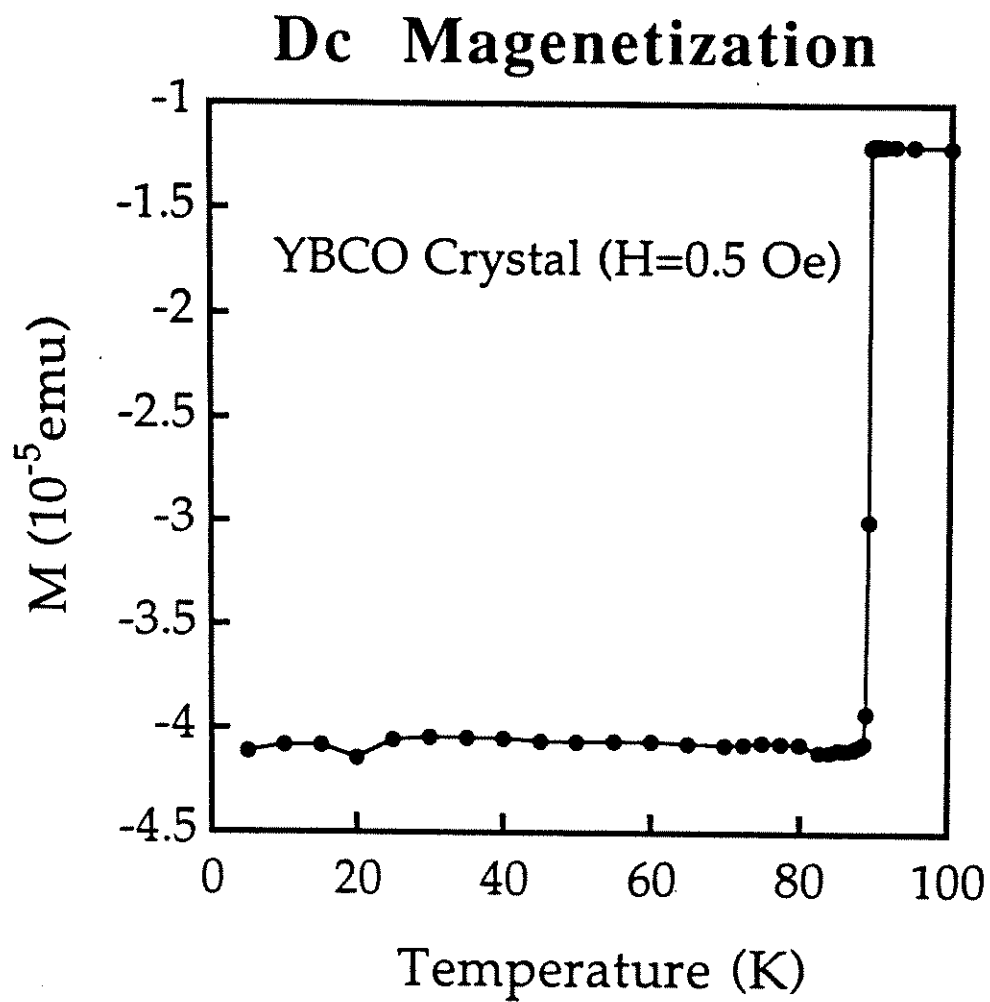
YBCO Crystal (H=0.5 Oe)

Figure 4.10   Dc magnetization for a YBCO crystal.

114
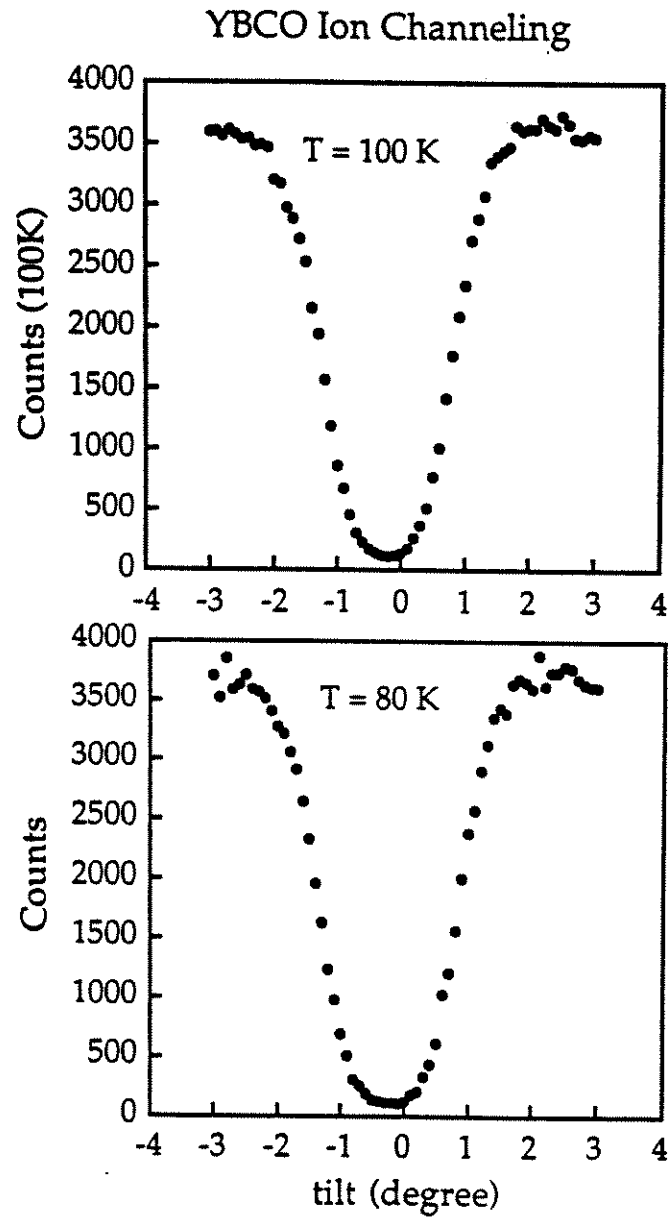
Figure 4.11   Ion channeling angular scans for a YBCO single crystal taken with 1.5 Mev He+ ions. (a) A scan performed at superconducting state (T = 80 K < T$_c$ ~ 92 K.); (b) A scan performed at normal state (T = 100 K).

115

4-3 The Crystal Structures of YBCO and NCCO

Figure 4.12 shows the crystal structure of YBCO. It has a perovskite structure with oxygen deficiency. The unit cell is orthorhombic with a= 3.818Å, b=3.89Å, and c=11.68Å. Each unit cell consists of two CuO_2 planes separated by an atom of yttrium, a CuO chain along the b direction above these planes and two barium atoms lying between the CuO_2 planes and the CuO chains

Figure 4.13 shows the crystal structure of NCCO. Nd_2CuO_4 has a tetragonal T'-phase structure similar to the well known K_2NiF_4 structure. By Ce doping, some Nd atoms are replaced by Ce atoms, electrons are created in the CuO_2 plane, and $Nd_{2-x}Ce_xCuO_4$ are formed in the same tetragonal structure with lattice parameters a = b = 3.945 Å and c = 12.06 Å. Each unit cell of NCCO has one CuO plane and there is no CuO chain.

4-4 Phase Diagrams

Figure 4.14 shows the temperature-dopant concentration phase diagrams of n-type NCCO and p-type LaSrCuO. It shows the same occurrence of the insulator to metallic and superconducting transition independent of electron or hole doping. From the phase diagram of a cuprate $La_{2-x}Sr_xCuO_4$, we can see that as x increases, which means additional holes are added to the CuO_2 layer when Sr replaces some of the La, the antiferromagnetic order is suppressed and the system eventually becomes metallic and superconducting. Generally, all the high temperature superconductors can be made by changing the doping element level (hence the doing level of holes or electrons) in their parent compounds, which are

Crystal Structure of YBCO
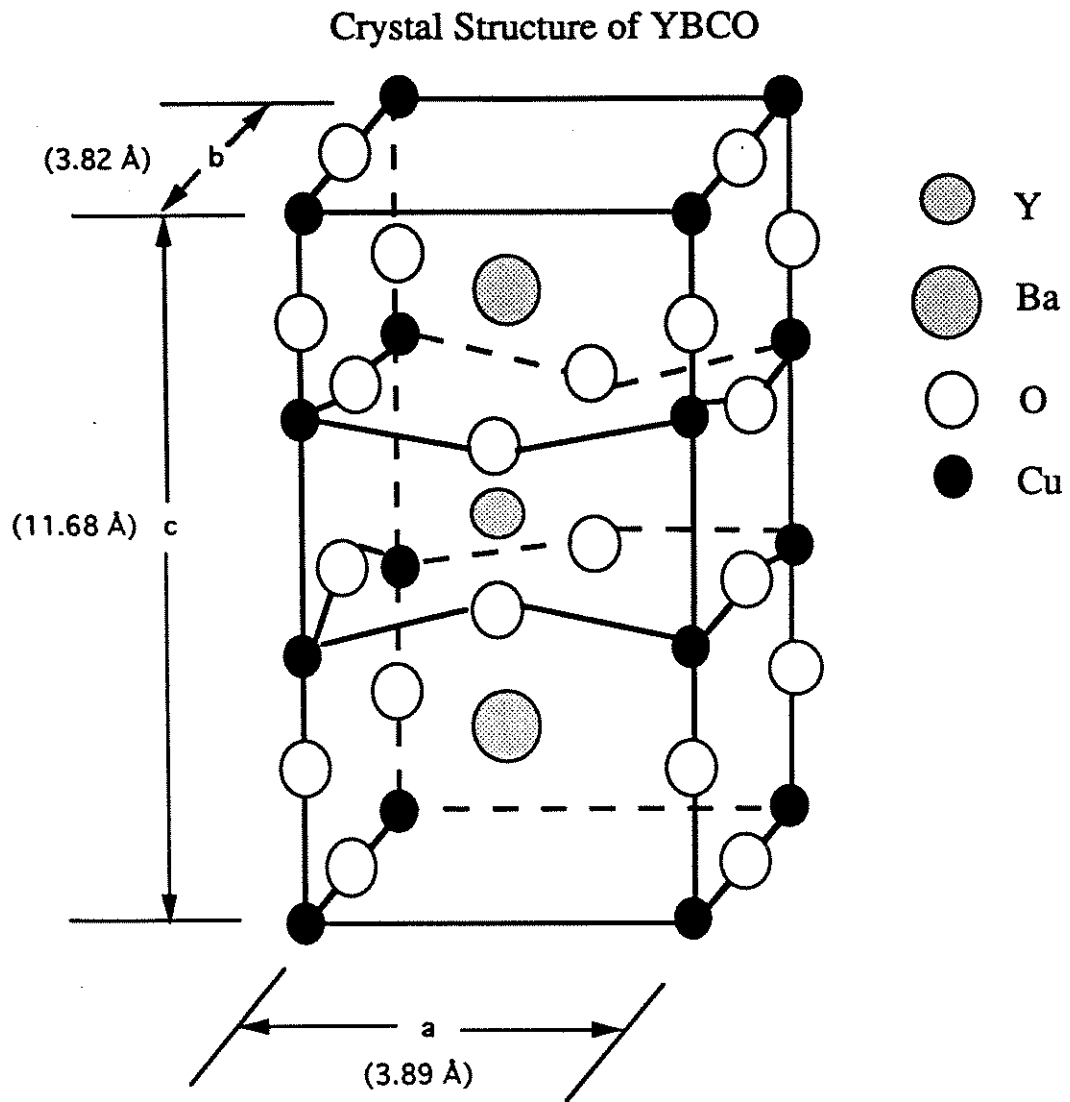
Figure 4.12   Crystal structure of YBCO.

Crystal Structure of NCCO
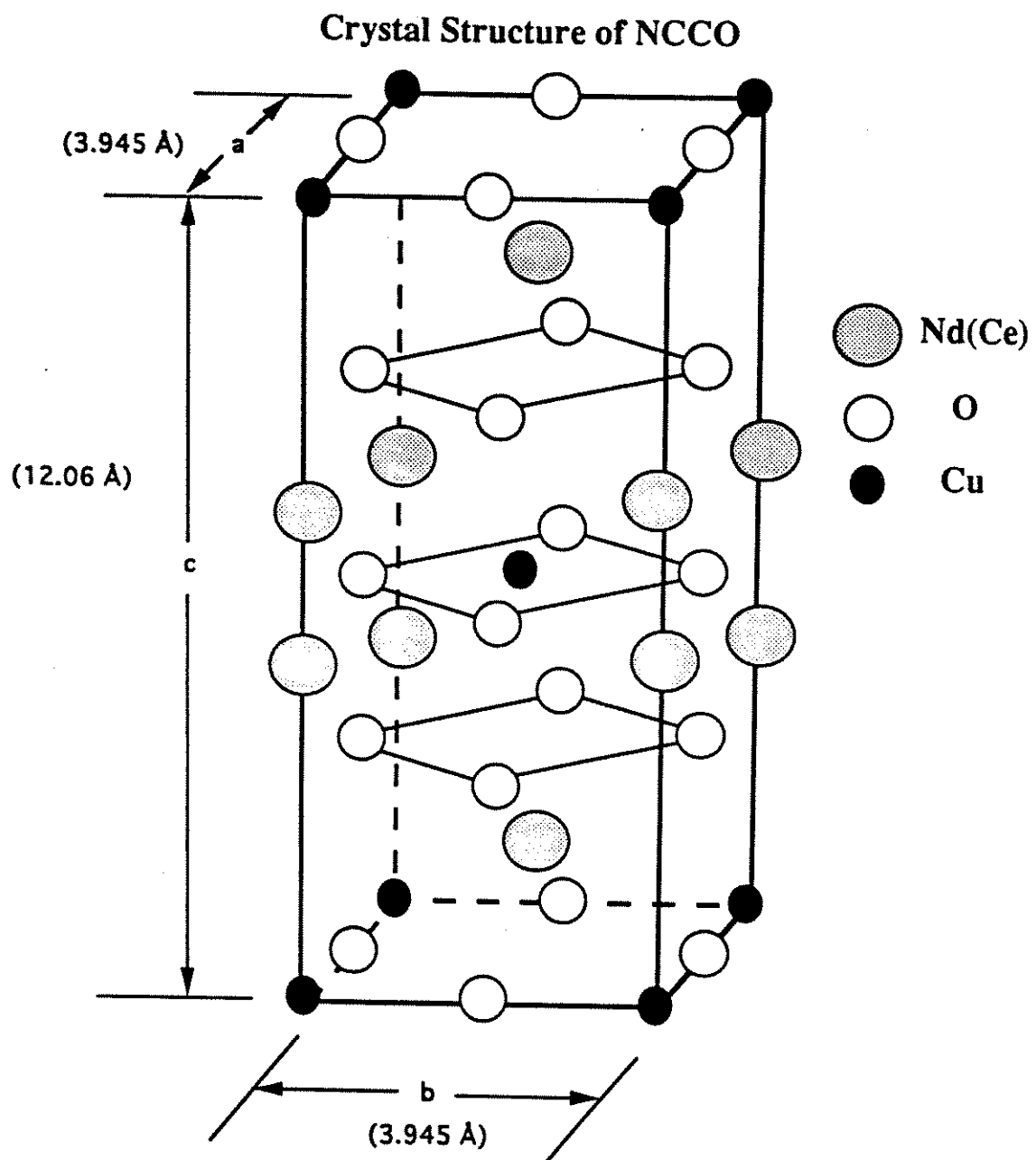
Figure 4.13   Crystal structure of NCCO.

118

NCCO phase diagram

Metallic ⟵ Insulating ⟶ Metallic
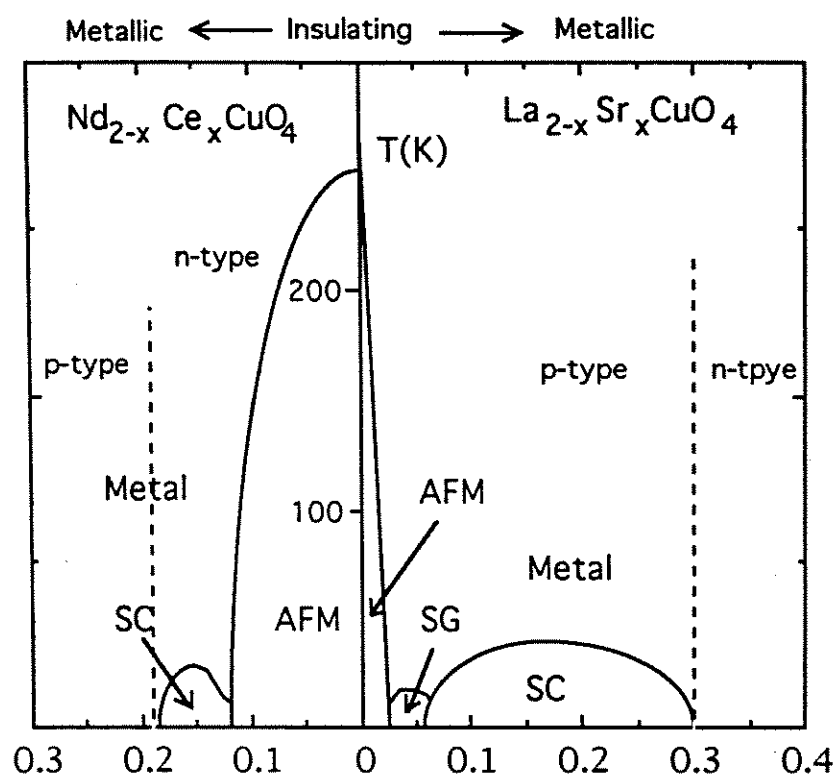
SC: Superconductor
AFM: Insulating Antiferromagnet
SG: Spin glass

Figure 4.14   Temperature-dopant concentration phase diagram of NCCO.

all insulating antiferromagnets (AFM). However, there are marked differences between electron- and hole- doped systems. For instance, in the NCCO compound, the superconductivity disappears abruptly and it becomes an insulating antiferromagnet with decreasing deping in contrast to that of LaSrCuO. Also in LaSrCuO, the superconducting doping range is much broader.

With such a rich phase diagram, it is not surprising that there have been many proposed pairing mechanisms, including electron-phonon[12] or charge-transfer[13] models (s-wave pairing) and models based upon the antiferromagnetic nature of the undoped system which involve d-wave pairing. [14-16]. There are also models which suggest that the pairing is caused by the interlayer hopping, which is predicted to give rise to anisotropic s-wave pairing.[17]

REFERENCES

[1] J. L. Peng, Z. Y. Li and R. L. Greene, Physica C **177**, 79-85 (1991).

[2] J. L. Peng, R. L. Greene, P. Klavins, R. N. Shelton and H. B. Radousky, Mat. Res. Soc. Symp. Proc. **169** , 173(1990); J. L. Peng and R. L. Greene, Physica C **172**, 173(1990).

[3] A. R. Drews *et al.*, Physica C **200**, 122 (1992).

[4] H. Muller-Buschbaum, Angew. Chem. Inst. Engl. **16**, 674(1977).

[5] A. Gupta, G. Koren, C. C. Tsuei, A. Segmueller, and T. R. McGuire, Appl. Phys. Lett. **55**, 1795 (1989).

[6] S. N. Mao, X. X. Xi, S. Bhattacharya, Qi Li, T. Venkatesan, J. L. Peng, R. L. Greene, Jian Mao, Dong Ho Wu, and S. M. Anlage, Appl. Phys. Lett. **61**, 2356 (1992); S. N. Mao et al., J. Appl. Phys. **75**, 2119 (1994).

[7] D. Prasad Beesabathina, L. Salamanca-Rica, S. N. Mao, X. X. Xi, T. Venkatesan, X. D. Wu, J. Mater. Res., 1376 (1994); D. Prasad Beesabathina, L. Salamanca-Rica, S. N. Mao, X. X. Xi, T. Venkatesan, Appl. Phys. Lett. **62**, 3022 (1993).

[8] D. L. Kaiser, F. Holtzberg, B. A. Scott, and T. R. Mcguire, Appl. Phys. Lett. **51**, 1050 (1987).

[9] R. P. Sharma, et al., Phys. Rev. B. 43, 13711 (1991); R. P. Sharma et al., Phys. Rev. B **40**, 11396 (1989).

[10] T. A. Friedman et al., Phys. Rev. B **42**, 6217 (1990).

[11] D. A. Bonn et al., Phys. Rev. B **47**, 11314 (1993).

[12] W. E. Pickett, Rev. Mod. Phys. **61**, 433 (1989).

[13] C. M. Varma et al., Solid State Comm. **62**, 681 (1987).

[14] D. S. Rokhsar, Phys. Rev. Lett. **70**, 493 (1993).

[15] P. Monthoux, D. Pines, Phys. Rev. B **47**, 6069 (1993).

[16] N. Bulut, D. J. Scalapino, and S. R. White, Phys. Rev. B **47**, 6157 (1993).

[17] P. W. Anderson, Physica C **185**, 11 (1991).

CHAPTER 5

MICROWAVE SURFACE IMPEDANCE MEASUREMENTS OF HIGH Tc SUPERCONDUCTORS

One of the central questions in the study of high T_c superconductivity is the pairing state symmetry for the ground state wavefunction describing superconductivity. The debate on pairing mechanism responsible for superconductivity in the high T_c copper oxide materials is still an unresolved issue. Studies of the electrodynamic properties provide a clear phenomenological picture, and reveal information regarding the pairing state, energy gap, and density of states of the superconductor, and give important insights into the mechanisms of high T_c superconductivity.

To understand the electrodynamic properties of the cuprates, we performed measurements on Nb, NCCO, and YBCO, and studied them in a comparative manner as they represent a conventional BCS s-wave superconductor, an electron doped cuprate superconductor, and a hole-doped cuprate superconductor.

In this chapter, we present our experimental results and discuss them in the light of current theories or models. It is believed that a good experiment will past the test of time and can stand alone to establish a guidepost for new theoretical models in the future.

5-1   Penetration depth and Surface resistance

As we have discussed in previous chapters, penetration depth and surface resistance can be used as a probe to study the thermo-electric properties of a superconductor. The principle behind using $\lambda(T)$ as a probe of the pairing state is straightforward. In the conventional BCS theory (for instance, see "Introduction to Superconductivity" by M. Tinkham), the penetration depth is given by

$$\left(\frac{\lambda(0)}{\lambda(T)}\right)^2 = 1 - 2\beta \int_0^\infty d\omega \frac{N(\omega)}{N_0} f(\omega)(1-f(\omega)) \tag{1}$$

with $N(\omega)$ the quasi-particle density of states normalized to the normal state single-spin density of states N_0. For a constant s-wave gap Δ_0,

$$\frac{N(\omega)}{N_0} = \text{Re}[\frac{\omega}{\sqrt{\omega^2 - \Delta_0^2}}] \tag{2}$$

and the number of quasi-particles is exponentially small at low temperatures. The schematic Fermi surface in K_{xy} space for s-wave and d-wave states is shown in **Figure 5.1**.

Eq. (1) gives the well known BCS s-wave result

$$\frac{\lambda(T)}{\lambda(0)} - 1 \sim e^{-\Delta_0/k_B T} (\frac{2\pi\Delta_0}{k_B T})^{1/2} \tag{3}$$

for $\lambda(T)$ at low temperatures. For the $d_{x^2-y^2}$ state, a gap is developed over the Fermi surface with line nodes. The gap has a directional variation in the k_{xy} plane and can be described as

$$\Delta_K = \Delta_0 \cos\phi \tag{4}$$

where ϕ is the angle defined in **Figure 5.1**. For a gap with a node, such as a $d_{x^2-y^2}$ gap, at an energy ω which is small compared to the maximum value of the gap Δ_0, the ratio of density of states is given as

$$\frac{N(\omega)}{N_0} \approx \frac{\omega}{\Delta_0}, \tag{5}$$
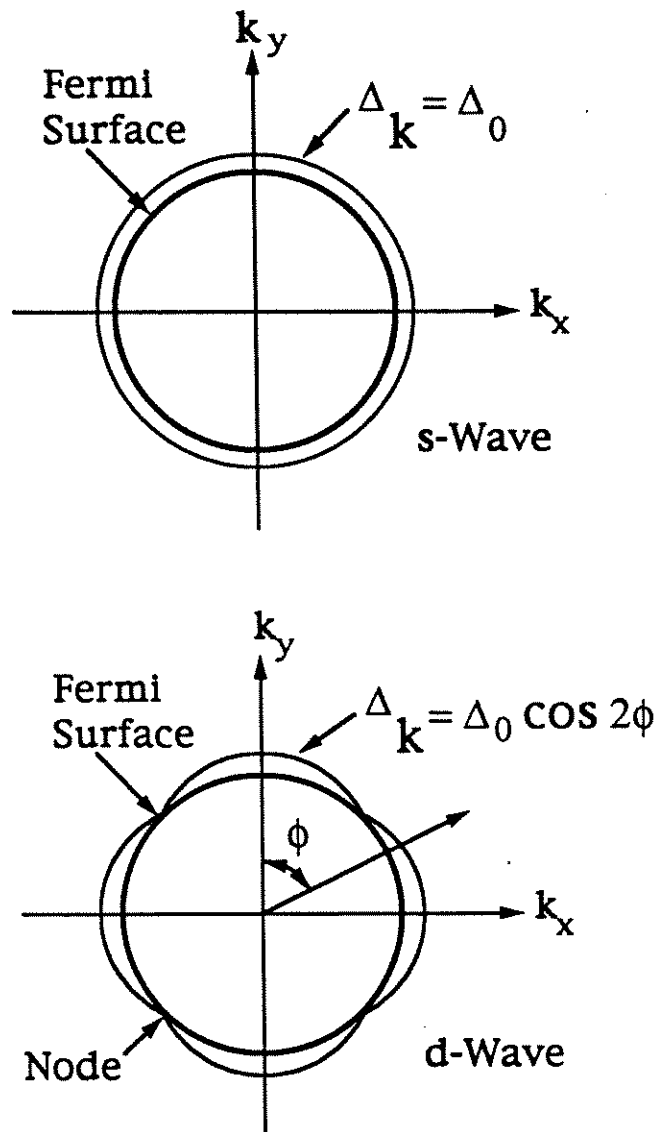
Figure 5.1 Schematic two-dimensional representations of idealized three-dimensional Fermi surfaces and associated superconducting energy gaps. On top is a cross section of an idealized spherical Fermi surface with a spherically symmetric energy gap representing an ideal s-wave superconductor. On the bottom is a cross section of an idealized cylindrical Fermi surface and a d-wave energy gap.

125

Hence, because of the nodes, the density of states increases as E-E$_F$ with respect to the Fermi energy at low energy and the number of quasiparticles is proportional to the temperature T. Using Eq. (1), we obtain

$$\frac{\lambda(T)}{\lambda(0)} - 1 \sim \ln(2)\frac{k_B T}{\Delta_0}. \qquad (6)$$

Thus, in principle, observation of an exponential temperature dependence at low temperature would enable the gap Δ_0 to be inferred. The absence of exponential behavior at low temperatures is consistent with nodes in the gap or gapless superconductivity.

The behavior of the surface resistance can also be predicted based on the same model. For the s-wave state, a full gap is developed over the Fermi surface and the number of quasiparticles is proportional to $e^{-\frac{\Delta_0}{k_B T}}$ for T<<T. Since the electromagnetic absorption, which corresponds to microwave loss, is proportional to the number of quasiparticles, the surface resistance

$$R_s \propto e^{-\frac{\Delta_0}{k_B T}} \qquad (7)$$

for T<<T$_c$. For a $d_{x^2-y^2}$ gap with line nodes as shown in **Figure 5.1**, the density of states increases as E-E$_F$ with respect to the Fermi energy at low energy. Hence, the number of quasiparticles is proportional to the temperature T. Consequently,

$$R_s \propto T^2 \qquad (8)$$

for T<<T$_c$ in a clean d-wave superconductor.

5-2   Measurements of Surface Impedance of YBCO

Recently a number of experimental results and theoretical interpretation of the results, suggest 2D d-wave superconductivity in the

ab-plane of hole-doped cuprate superconductors such as $YBa_2Cu_3O_{7-\delta}$ (YBCO).[1]-[4] However other theoretical models have been proposed to explain the linear temperature dependence of $\lambda_{ab}(T)$. Klemm explained the $\lambda_{ab}(T)$ data of Hardy et al.[3] in YBCO quantitatively, based upon proximity coupling between one s-wave superconducting and one normal layer per unit cell.[5] He also suggested measurements of $\lambda_c(T)$ as a way to conclusively distinguish the pairing state symmetry. Another theory proposed by Chakravarty et al.,[6] features low T_c pairing in each copper oxide layer enhanced by Josephson pair tunneling between layers. There is an experiment suggesting that the electrodynamic properties in the superconducting state along the c-axis of $La_{2-x}Sr_xCuO_4$ can be explained by a similar Josephson-coupled layer model,[7] although no conclusion was made about the pairing state symmetry.

In principle, one should be able to use c-axis surface impedance measurements to measure the anisotropy of the gap and put further constraints on the pairing state symmetry.[8][9] The properties of the superconducting state in the c-direction of YBCO, such as the penetration depth, surface resistance R_s and conductivity σ, are still not clear. In this Chapter, we present the temperature dependence of $\lambda_{ab}(T)$, $\lambda_c(T)$, R_{s-ab}, R_{s-c} and σ_c of YBCO single crystals, to shed further light on the pairing state symmetry of the cuprates.

The surface impedance measurements were made by the cavity perturbation method described in the previous Chapters. The surface resistance and the penetration depth data are obtained via the simultaneous measurement of the quality factor Q and the resonant

127

frequency f_0 of the cavity as a function of the sample temperature in a cylindrical Nb cavity. The surface impedance is obtained from the Q and f_0 using Eqs. (26)(31)(34) of Chapter 3

$$R_s = \Gamma_s (1/Q - 1/Q_{cav}), \Delta X_s = 2\pi f_0 \mu_0 \Delta\lambda, \text{ and } \Delta\lambda = -\xi_s \nabla\omega \qquad (9)$$

The quality factor of our cavity without a sample was $Q_{cav} \sim 2.3 \times 10^7$ at 4.2 K and 9.6 GHz. With this high Q, we achieved a resolution of $\Delta(1/Q) \sim 5\times10^{-10}$ and $\Delta f_0 \sim 1$ Hz, translating to $\Delta R_s \leq 50$ $\mu\Omega$ and $\Delta\lambda \leq 3$ Å for a typical YBCO crystal of size 1 mm x 1 mm x 25 μm. Note that in contrast to lower frequency measurements which are carried out at UBC,[3] we do not need to consider the finite thickness correction because in our frequency range the ab-plane and c-axis skin depths are far less than the corresponding sample dimensions.[10] To determine the geometric factors, both theoretical calculations (see Chapter 3) and careful experimental calibrations are performed. In the calibrations, Nb samples of dimensions similar to the NCCO and YBCO samples are used. The geometric factors obtained from calibrations were close to those calculated from our knowledge of the cavity and sample geometry. Also the value determined for geometric factors was independently verified by comparing a measured microwave R_s in the normal state with a calculated

$$R_s = \sqrt{\rho_n \omega \mu_0 / 2}, \qquad (10)$$

obtained from independent measurements of the dc resistivity.

To study the anisotropy of YBCO, we measure the crystals in two orientations: In experiment I, the c-axis of the crystal is parallel to the rf magnetic field; In experiment II, the c-axis is perpendicular to the rf magnetic field (see the inset of **Figure 5.2**). Assume the crystal has width w,

height h and thickness t (see fig. 3.3). In experiment I, the rf current is induced only in the ab plane ensuring that we measure just λ_{ab} and R_{s-ab}. As discussed in Chapter 3, the complex loss is given by

$$P(\omega) = Z_{s,ab,bulk} H_a^2 hw.$$ (11)

In this configuration, because the rf field is perpendicular to the large sample surface area (ab-plane), the demagnetization factor becomes large, and makes the calculation of the geometrical factors difficult.[10][11] Therefore the geometric factor was determined by comparing the normal state surface resistance at 100 K with the dc resistivity $\rho_{ab}(100\ K) \approx 40$ $\mu\Omega cm$ (as given in Eq. (10)). As a check, a Nb crystal of known resistivity and similar size was used to independently determine the geometric factors.[11] From these comparison and analysis, we found $R_s(T > T_c) \approx X_s(T > T_c)$ for both YBCO and Nb crystals in experiment I.

In experiment II, the demagnetization factor is approximately one. The geometric factors can be calculated precisely and are in excellent agreement with the experimental data on the Nb crystal placed in this orientation.[12] The complex loss is given by Eq. (3.53). The c-axis penetration depth λ_c, and surface resistance R_{s-c} can be extracted from experiments I and II using Eq. (3.52) of Chapter 3. The λ_c and R_{s-c} has been extracted for several crystals of different thickness t, and the results are qualitatively similar. Here we will analyze the properties of one crystal in detail which represents those of all the samples.

a) Results of $\Delta\lambda$
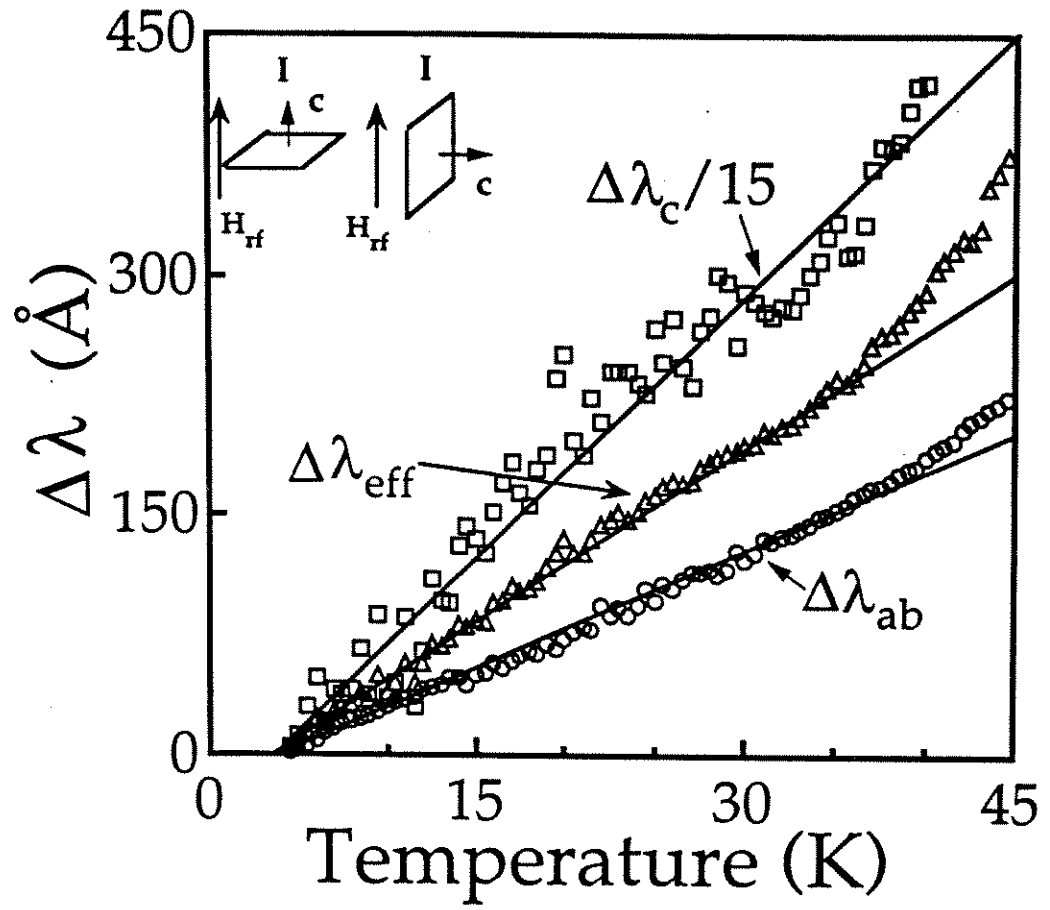
Figure 5.2   Temperature dependence of the penetration depth $\Delta\lambda = \lambda(T) - \lambda(4.2\ \mathrm{K})$ in a YBCO single crystal. Solid lines are the linear fits. The inset shows the orientation of the crystal in the two experiments.

Figure 5.2 shows $\Delta\lambda=\lambda(T) - \lambda(4.2 \text{ K})$ for $\Delta\lambda_{ab}$, $\Delta\lambda_{eff}$ and $\Delta\lambda_c/15$ for a YBCO crystal. The strong linear temperature dependence extends up to 40 K in λ_{ab} and λ_{eff}, and therefore λ_c. The slope $d\lambda_{ab}/dT = 5\text{Å}/\text{K}$, slightly bigger than $4.3\text{Å}/\text{K}$ reported by the UBC group,[3] is consistent with the clean d-wave model for a superconductor with line nodes in the gap.[9][13] As for the penetration depth along the c-axis, the slope is $d\lambda_c/dT \approx 130\pm15$ Å/K (we find that the exact values of these slopes vary from sample to sample). Recently, Klemm et al., calculated $\lambda_c(T)$ using a multilayer proximity model, and their $\lambda_c(T)$ shows an activated behavior (exponential) at low temperatures.[5] Our result that $\Delta\lambda_c(T)$ is linear at low temperatures is consistent with the d-wave model and not with the multilayer proximity model. Also, an extrinsic proximity effect model which supposes that a normal metal 'dead layer' exists on the surface of the YBCO crystal,[14] cannot account for either the ab-plane or c-axis penetration depth measured here.[15]

b) Determination of $\lambda(0)$

To determine the absolute magnitude of the penetration depth in experiment I, we assume YBCO is in the London limit $(\lambda \gg \xi(0))$ and use the identity

$$X_s(4.2 \text{ K})/R_n(100\text{K}) = 2 \lambda(4.2 \text{ K})/\delta, \qquad (12)$$

where δ is the skin depth, to deduce the value of penetration depth at 4.2 K.[16] Since $X_s=\mu_0\omega\lambda$, we have $X_s(4.2 \text{ K}) = X_s(100 \text{ K}) - \omega\mu_0 \Delta\lambda$, where $\Delta\lambda$ is the measured penetration depth change from 4.2 K to 100 K and $X_s(100 \text{ K})$ $= R_s(100\text{K}) = (\omega\mu_0\rho\delta_c/2)^{1/2}$ in the normal skin-effect regime. **Figure 5.3**

131
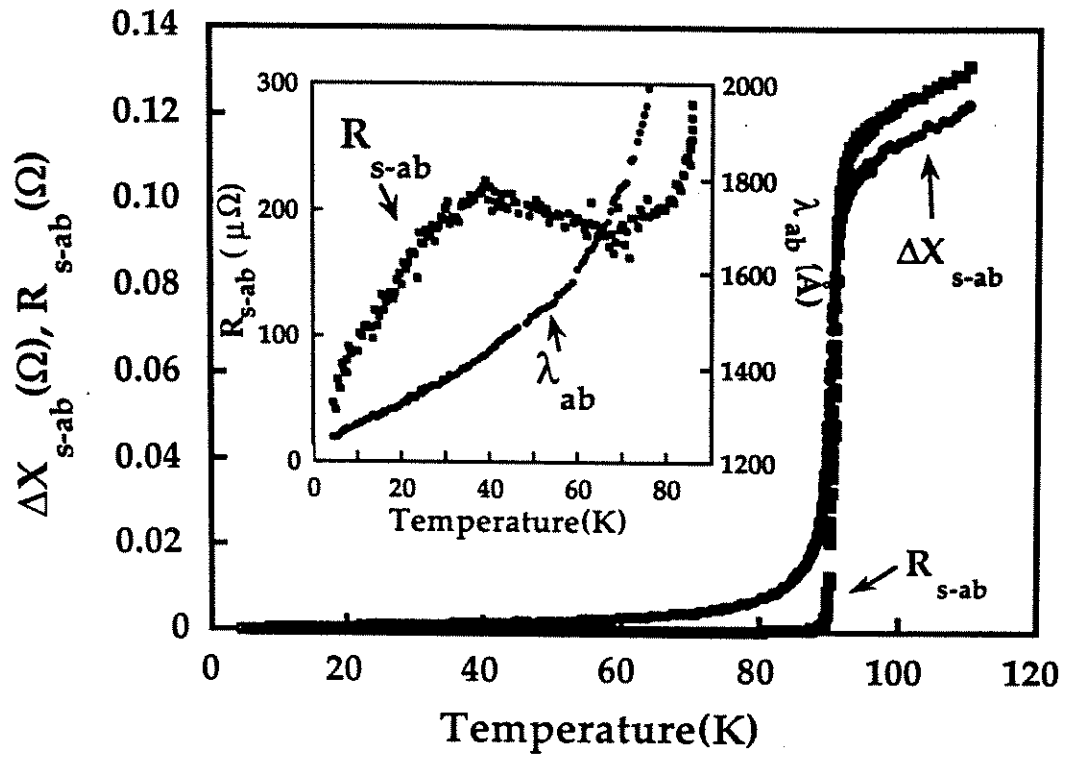
Figure 5.3   Temperature dependence of the surface impedance of a YBCO crystal measured at 9.6 GHz. Inset shows the detailed low temperature dependence of $R_{s,ab}(T)$ and $\lambda_{ab}(T)$.

shows the surface resistance R_S and the change of surface reactance $\Delta X_s = X_s(100 \text{ K}) - X_s(4.2 \text{ K})$. We obtain $\lambda_{ab}(4.2\text{K}) = 1250$ Å, and if we assume the linear behavior continues below 4.2 K, this extrapolates to $\lambda_{ab}(0) = 1230$ Å. An alternative (and somewhat arbitrary) method for estimating $\lambda_{ab}(0)$ is to plot $\Delta\lambda$ vs y, where $y = 1/[1-t^4]^{1/2}$ is the Gorter-Casimir temperature dependence, $t = T/T_c$, and T_c is chosen to be 90.5 K.[17] When the data is plotted in this way which is shown in **Figure 5.4**, we obtain a straight line from 75 K up to 90.4 K with a slope giving $\lambda_{ab}(0) = 1200$ Å, nearly equal to the value obtained above. In experiment II, we cannot determine $\lambda_{eff}(0)$ using the normal state impedance as $X_{seff}(T>Tc) \neq R_{seff}(T>T_c)$.[10][12] However, applying the Gorter-Casimir relation in the same way (**Figure 5.4**), we obtain an estimated value of $\lambda_{eff}(0) = 1380$ Å. Assuming the linear temperature dependence between 4.2 K and 40 K can be extrapolated to 0 K, we have $\lambda_{eff}(4.2 \text{ K}) = 1415$ Å. All the $\lambda(0)$ values determined here are in the range of reported values[3][18] and they are not strongly dependent on the $\lambda(T)$ extrapolation or T_c value assumed, although they do vary by $\approx$ 20% from sample to sample. Using Eq. (3.52) and the value of λ_{eff} and λ_{ab}, we extract $\lambda_c(0) \approx 1.05\mu m$. The anisotropy of the magnetic penetration depth, $\lambda_{ab}/\lambda_c \sim 9$ for $T \leq T_c/2$, in good agreement with recent estimates made from infrared reflectivity measurements.[19]

c) Interpretation of λ

Annett, et al.,[8] predicted that a superconducting state with four line nodes parallel to the c-axis on a cylindrical Fermi surface will show

$$\Delta\lambda_{ab}(T)/\lambda_{ab}(0) \sim a\ (T/T_c) + b\ (T/T_c)^3, \tag{13}$$

133
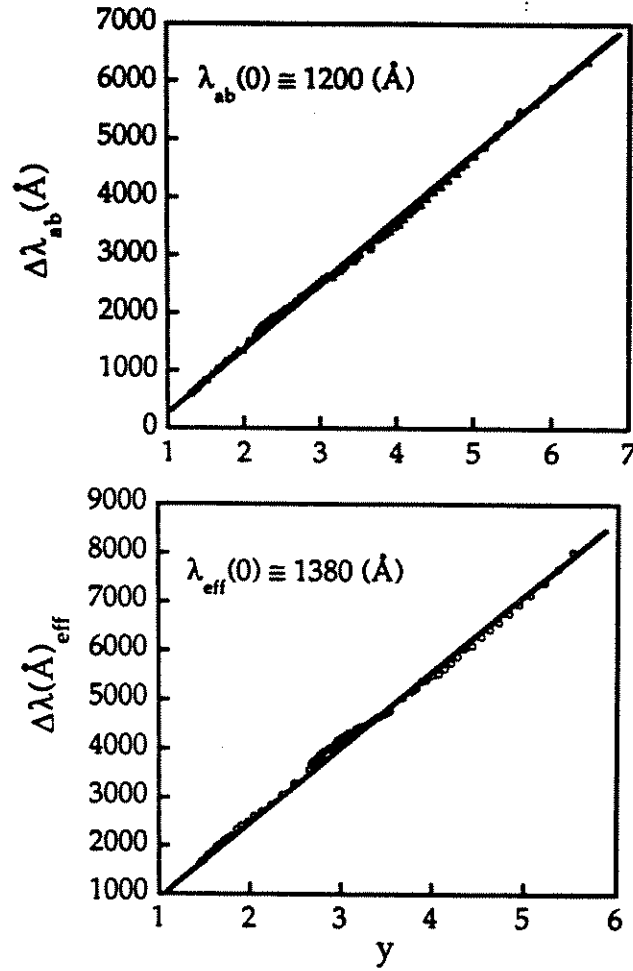
Figure 5.4   The penetration depth $\Delta\lambda = \lambda(T) - \lambda(4.2\ K)$ in a YBCO single crystal vs. $y = \dfrac{1}{\sqrt{(1-(\frac{T}{T_c})^4}}$. a) $\Delta\lambda_{ab}$ vs y with T_c of 90.5 K giving $\lambda_{ab}(0) \sim 1200$ Å; b) $\Delta\lambda_{eff}$ vs y with T_c of 90.5 K giving $\lambda_{eff}(0) \sim 1380$ Å

134

and

$$\Delta\lambda_c(T)/\lambda_c(0) \sim g\ (T/T_c) \tag{14}$$

at low temperatures. We find excellent fits to $\Delta\lambda_{ab}(T)$ of this form up to $T/T_c = 0.65$ with a = 0.32, b = 0.29, however linear fits to $\lambda_c(T)$ with g $\approx$ 1.5 are good only for $T/T_c < 0.3$.

Figure 5.5 shows the normalized superfluid density $[\lambda(0)/\lambda(T)]^2$, which is also proportional to the imaginary part σ_2 of the complex conductivity $\sigma = \sigma_1 - i\,\sigma_2$. The superfluid density along the c-axis is depleted linearly at low temperatures, but much faster than in the ab-plane, with less than 10% remaining for temperatures above 50 K. At temperatures $0.35 < T/T_c < 1$, $[\lambda(0)/\lambda(T)]^2$ is proportional to $(T-T_c)/T^2$,[20] resembling the calculation of $1/\lambda_c(T)^2$ for a $d_{x^2-y^2}$ superconductor with a spherical Fermi surface.[9] In addition, the calculation of $\sigma_{2c}(T)$ for the cubic $d_{x^2+y^2-z^2}$ state does not resemble our data.

The steep drop of the superfluid density along the c-axis and ab-plane at low temperatures is in remarkable contrast to that of the BCS s-wave calculation, which is shown by the solid line in **Figure 5.5**. The slope of $[\lambda(0)/\lambda(T)]^2$ at $T/T_c = 1$ for the ab-plane is about 4.06, and for the c-axis it is about 0.37, whereas the weak-coupled BCS theory gives a value for this slope of exactly 2 in the London limit.[21] This value for the slope in the ab-plane is larger than any conventional superconductor,[21] while the slope for the c-direction is comparable to the weak-coupled limit of a cubic d-wave superconductor.[22]

d) Surface resistance
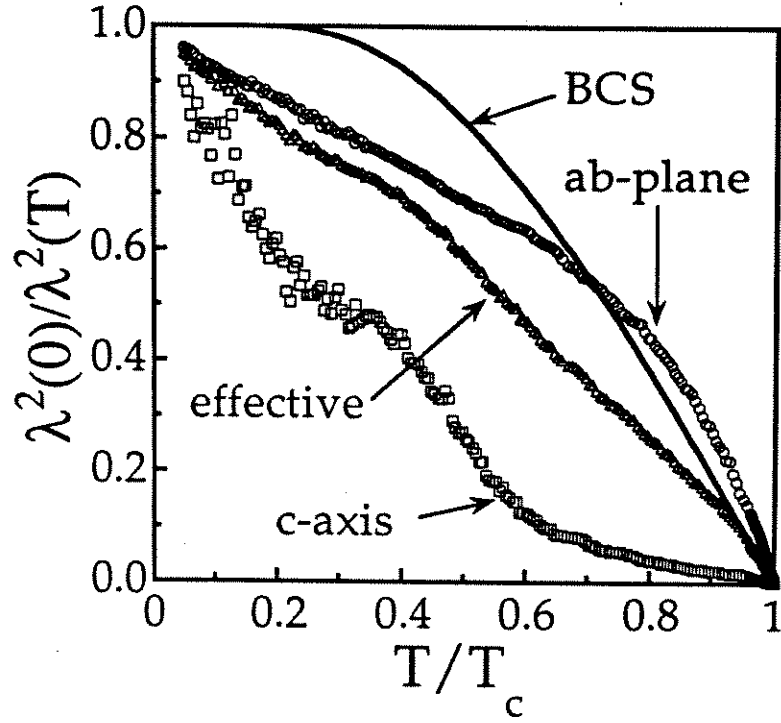
Figure 5.5 $\lambda^2(0)/\lambda^2(T)$ vs T/T_c for λ_c, λ_{ab} and λ_{eff} in a YBCO crystal. Data for λ_{ab} and λ_{eff} are experimental results. Data for λ_c are extracted from λ_{ab} and λ_{eff}. Solid line is the weak-coupled BCS s-wave calculation.
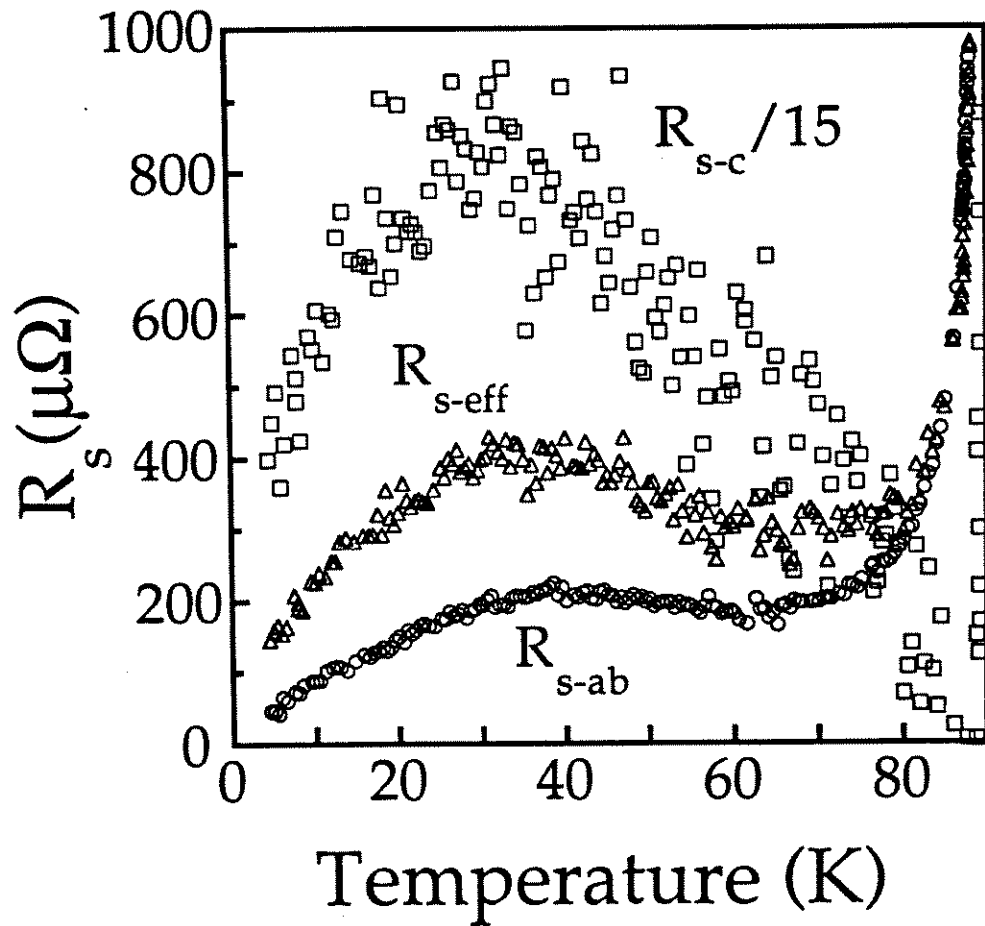
Figure 5.6 Surface resistances for $R_{s,ab}$, $R_{s,eff}$ and $R_{s,c}/15$ of a YBCO crystal. Data for $R_{s,c}$ is extracted from $R_{s,ab}$ and $R_{s,eff}$.

Figure 5.6 shows the surface resistance in the ab-plane, and the effective surface resistance, which contains the contribution from the c-axis component. The losses drop by 3 orders of magnitude in a few degrees below T_c, reach a minimum around 70 K, and then increases to a maximum around 40 K for R_{s-ab} and 30 K for R_{s-c} before falling down again. The lowest value of $R_{s-ab} \sim 165\ \mu\Omega$ at the minimum dip around 70 K (210 $\mu\Omega$ at 77 K) is among the lowest reported surface resistance values measured at 10 GHz near 77 K.[23] The normal state $R_s(T)$ and $X_s(T)$ imply a metallic temperature dependence for $\rho_c(T)$, with a value $\rho_c(100K) \approx 4$ mΩcm, consistent with values obtained by c-axis transport[24] and infrared reflectivity.[19][25]

e) Conductivity $\sigma_1(T)$

Because we measure both R_s and ΔX_s simultaneously, we can determine $\sigma_1(T)$ using the fewest assumptions.[1][16] **Figure 5.7** shows the real part of the complex conductivity σ_1 along the c-direction and in the ab-plane. There is no residual resistance subtraction from R_{s-ab}, while for R_{s-c}, about 5 mΩ was subtracted to make $\sigma_{1-c}(T\rightarrow0)\rightarrow0$ in **Figure 5.7**. From **Figure 5.7**, we can clearly see that there are two peaks in σ_{1-ab}: a broad peak centered around 30 K and sharp peak near T_c. These peaks resemble the conductivity data reported by Bonn *et al.* (YBCO crystals) and Gao *et al.* (thin film YBCO samples). In σ_{1-c}, the first peak occurs between 15 and 30 K, and the conductivity in the c direction is at least 30 times less than that of the ab-plane. In the clean d-wave model, one expects $\sigma_1(T) \sim T^2$ at low
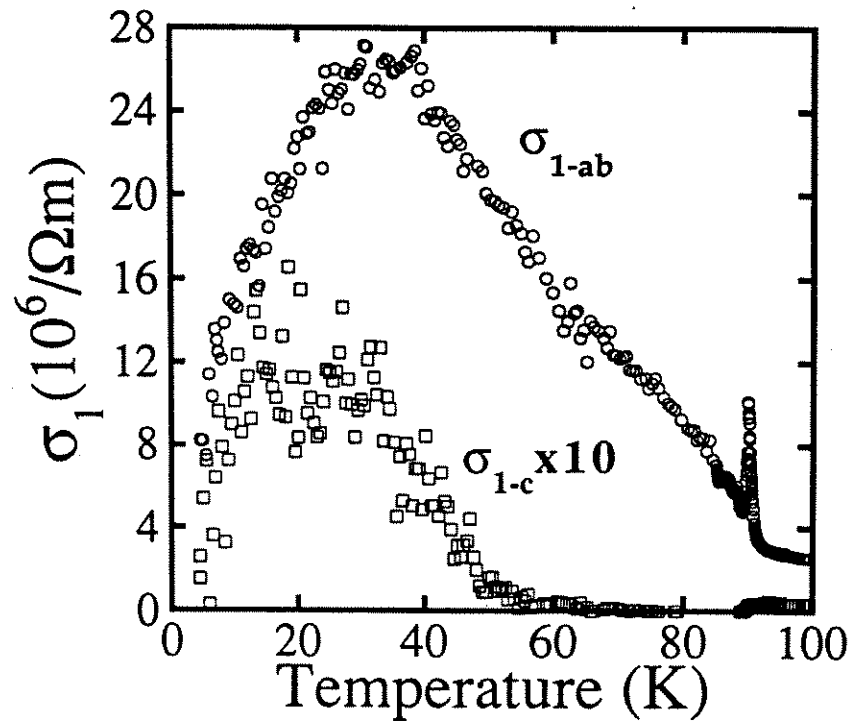
Figure 5.7   The real part of conductivity $\sigma_{1\text{-}ab}$ and $10 \times \sigma_{1\text{-}c}$ as a function of temperature for a YBCO crystal.

temperatures.[13] However, we see a sublinear temperature dependence for $\sigma_1(T)$ in both the ab-plane and c-axis directions at low temperatures.

The second sharp peak in $\sigma_{1\text{-ab}}(T)$ occurs just near T_c precisely at the point where $\sigma_2 = \sigma_1$, and it is not seen in data on Nb crystals. This peak in $\sigma_1(T)$ may be due to the sample inhomogeneities which broaden the transition, and/or enhanced fluctuations in the microwave conductivity near T_c.[17] The peak in **Figure 5.7** is among the sharpest ever seen at microwave frequencies[1] and if it is due to inhomogeneities, it is a sign that all YBCO crystals studied to date are by no means "ideal".

f) Quasiparticle scattering

A two-fluid interpretation of the c-axis conductivity leads to qualitatively similar conclusions as those obtained for the ab-plane results by the UBC group.[1][26] We find that both $1/\tau_{ab}(T)$ and $1/\tau_c(T)$ fall dramatically below T_c, although neither clearly follow the $(T/T_c)^3$ form predicted by the d-wave model,[13][27] with $1/\tau_{ab}(4.2K) \sim 10^{11}$ Hz and $1/\tau_c(4.2K) \sim 3 \times 10^{11}$ Hz.[28] The ab-plane scattering rate is better described as $1/\tau_{ab}(T) \sim x_{n,ab}(T)^p$ where $p \sim 2.1$ to 2.4 (for ab-plane normal fluid fraction $x_{n,ab} > 0.25$), and $p < 1/2$ (for $x_{n,ab} < 0.25$), perhaps indicative of quasiparticle-quasiparticle scattering at high temperatures, and residual scattering at lower temperatures. The c-axis scattering rate reaches its residual value below about 10 K, and its value is somewhat smaller than a recent far-infrared determination of 85 cm^{-1} ($\sim 2.6 \times 10^{12}$ Hz).[19] This low value of the residual scattering rate is consistent with our observation of a 'clean-node' $\Delta\lambda_c(T) \sim T$ at low temperatures.[8][29] It may also mean that

non-local electrodynamic corrections could become important in YBCO at low temperatures.

g) Discussion

Our results for $\sigma_{1c}(T)$ and $\lambda_c(T)$ in YBCO are rather different from other recent measurements of c-axis properties in related cuprate materials. s-wave-like temperature dependencies have been seen in the c-axis plasma frequency of $YBa_2Cu_4O_8$ by Basov, et al.,[30] and in $\lambda_c(T)$ of $La_{2-x}Sr_xCuO_4$ by Shibauchi, et al. [7] The samples measured by Basov, et al., had no coherent Drude-like component in the low frequency conductivity and are thought to be naturally underdoped[30] whereas our samples, like those of Schützmann, et al.,[19] have a metallic c-axis conductivity above T_c. This suggests that the c-axis electrodynamic properties may be very sensitive to doping (since the low resistivities of our samples, and the low T_c of Schützmann's samples suggest that they are overdoped), as well as to the particular layered structure of each cuprate material.

5-4   Measurement Results of Surface Impedance of NCCO

In this section, we report experimental results on the temperature dependent penetration depth $\lambda(T)$ and surface resistance $R_s(T)$ of high quality NCCO samples, measured at 9.6 GHz. In addition, we also report a comparison of $\lambda(T)$ at 9.6 GHz and at zero frequency, measured using a dc SQUID at low-fields (≤ 0.3 Oe).

The typical dimension of thin film NCCO samples is 2.6×5.5 mm^2 with a film thickness of about 5000Å.

Both thin films and single crystals show a sharp transition (≤ 0.2 K wide in AC susceptibility or in a DC SQUID characterization) at $T_c \sim 21$-22 K. Measurements of the complex surface impedance Z_s ($= R_s + i\omega\mu_0\lambda$) of NCCO were carried out by using the same hot finger technique which is used for YBCO samples. The geometrical factors were carefully determined experimentally by using Nb samples of dimensions similar to the $Nd_{1.85}Ce_{0.15}CuO_4$ samples. The measured geometry factors were close to those calculated from our knowledge of the cavity and sample geometry. The measurements were carried out in the temperature range of 4.2 K $\leq$ T ≤ 30 K, where the background temperature dependence of the cavity and sapphire hot-finger, Q_{cav}, are negligible (by experiment) and does not limit the resolution for either R_s or λ. With a typical size of thin film, we achieved a resolution $R_s \approx 10$ $\mu\Omega$ and $\delta\lambda \leq 2$ Å, over the entire temperature range.

In **Figure 5.8**, we show typical results for $1/Q(T)$ and $\delta f(T)$ for $T/T_c \leq 0.5$, for an NCCO thin film. The insets display Q and f over the entire temperature range. Bearing the relation $\delta\lambda \propto \delta f$ and $R_s \propto 1/Q$ in mind, we can discern the temperature dependence of $\delta\lambda$ and R_s directly from the raw data, particularly at low temperatures since it is widely believed that the symmetry of the pairing state[8] of a superconductor is directly manifested in the low temperature dependence of Z_s. The best fit of $\delta f(T)$ can be obtained with an exponential dependence[31] with $\delta f \propto \frac{1}{\sqrt{T}}\exp(-\frac{\Delta(0)}{K_BT})$ implying the energy gap ratio $2\Delta(0)/k_BT_c = 4.1$ or a power-law dependence $\delta f \propto T^n$ with $n \geq 4$ (which is, in practice, indistinguishable from the exponential.) In the fit for $1/Q(T)$, identical results were obtained, i. e. the

142
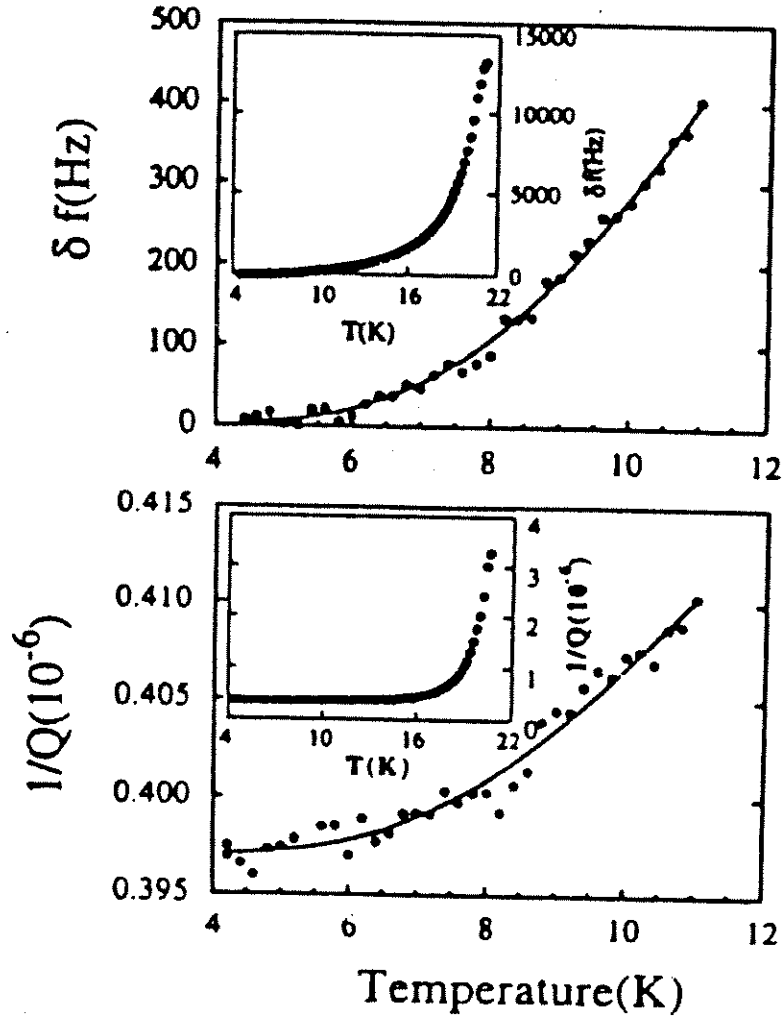
Figure 5.8 Temperature dependence of δf and $1/Q$ for $T/T_c < 0.5$ for a NCCO thin film. The solid lines are the best fit to data which show $\delta f \propto \frac{1}{\sqrt{T}} \exp(-\frac{\Delta(0)}{k_B T})$ and $1/Q \propto \frac{1}{T} \exp(-\frac{\Delta(0)}{k_B T})$ both with the gap ratio $2\Delta(0)/k_B T_c = 4.1$. Insets: δf and $1/Q$ for entire temperature range.

143

exponential dependence $1/Q \propto \frac{1}{f}\exp(-\frac{\Delta(0)}{k_{B}T})$ and the gap ratio $2\Delta(0)/k_{B}T_{c} =$ 4.1, as well as the power-law with $n \geq 4$. Hence, both the Q and f data strongly suggest the s-wave BCS type temperature dependence of R_{s} and λ at low temperatures in NCCO.

In our data, the BCS-like features are not limited to only low temperatures but also continue up to near T_{c}, and moreover, the data show a clear quantitative agreement with the BCS description. In **Figure 5.9**, a comparison with a detailed BCS calculation, with the frequency and wave-vector dependence kernel,[31] is made for two typical data sets of $\lambda(T)$: one from a thin film at 9.6 GHz and the other from a single crystal at zero frequency by dc magnetization measurements. Both of them exhibit the s - wave BCS-type temperature dependence in general, although the later is less obvious because of much larger experimental error. The numerical calculation requires several parameters, including a measurement frequency f, transition temperature T_{c}, the London penetration depth λ_{L}, the coherence length ξ, the quasiparticle mean free path ℓ, and gap ratio $2\Delta(0)/k_{B}T_{c}$. The typical parameter values for the best fits to thin film and single crystal data are listed in **Table I**. Frequency dependence of the parameters is not seen in this work, and is possibly less than the error (~ 10%) in determining the parameter values. The coherence length was determined experimentally, while the mean free path, the London penetration depth λ_{L} and the gap ratio $2\Delta(0)/k_{B}T_{c}$ were treated as fitting parameters to yield the best fit. The in-plane coherence length $\xi_{\parallel}$ (this agrees with reference [32]) at zero temperature was estimated from the magnetoresistance measurements. An estimate of the

144
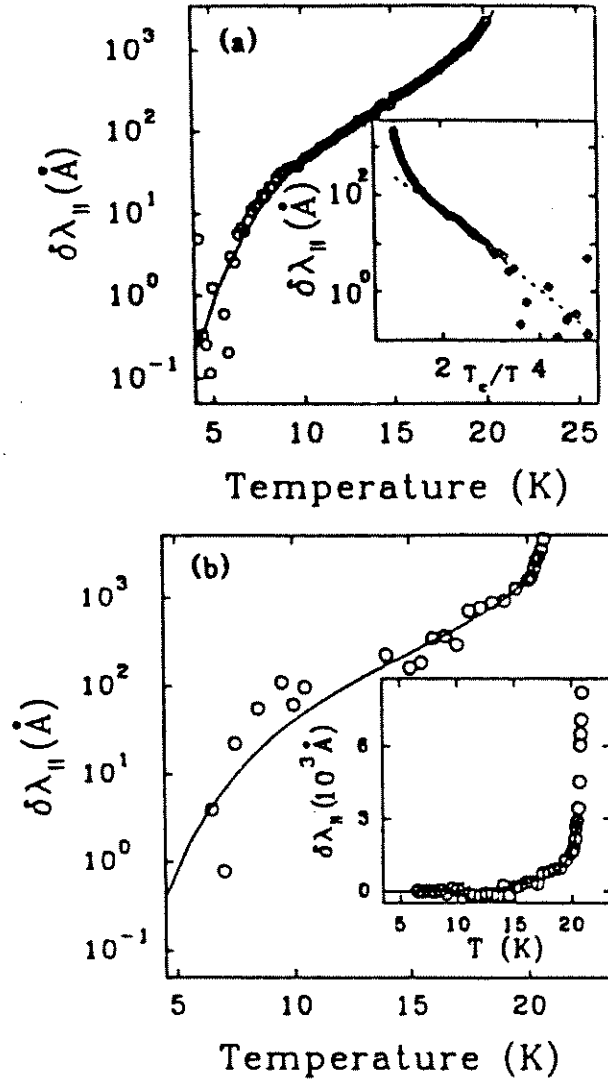
Figure 5.9 a) Change in the penetration depth $\delta\lambda_{||}(T)$ at 9.6 GHz for a NCCO thin film. The solid line represents the BCS calculation with $2\Delta(0)/k_BT_c = 4.1$. Insets: $\delta\lambda_{||}$ vs T_c/T. Note the exponential behavior (dashed line) $\delta\lambda(T) \equiv \lambda(T) - \lambda(0) = \lambda(0)\, (\pi\,\Delta(0)/2k_BT)^{1/2}\, \exp(-\Delta(0)/k_BT)$ for $T_c/T{\geq}2$. b) $\delta\lambda_{||}(T)$ extracted from a dc magnetization measurement for a NCCO single crystal with a BCS fit for $2\Delta(0)/k_BT_c = 4.2$. Inset: Linear plot of $\delta\lambda_{||}(T)$.

145

mean free path ℓ is obtained from an experiment and analysis similar to reference [33]. However because a considerable uncertainty is involved in determining ℓ, we have further adjusted the value of ℓ in the BCS calculations.

Although ℓ, λ_L and $\Delta(0)/k_B T_c$ are used as free parameters, we adjust the values within certain ranges, because the experimentally determined effective penetration depth λ_{eff} constrains λ_L through

$$\lambda_{eff} = \lambda_L [1 + \xi_0 / J(R = 0, T) l]^{1/2} \tag{15}$$

where $J(0,T)$ is the BCS range function with a value $1 \leq J(0,T) \leq 1.33$. Further, the interplay between λ_L and $\Delta(0)/k_B T_c$ could change the value of λ_L as $\Delta(0)/k_B T_c$ varies. Considering these, we plot $d\lambda_{\parallel}/dy$ vs. $y \equiv 1/\sqrt{1-t^4}$, as shown in **Figure 5.10**, which shows the $d\lambda_{\parallel}/dy$ at $y > 2$ converges to yield $\lambda_{\parallel}^{eff}(0) \sim 1300 \pm 100 \text{Å}$. Using the value $\xi_0 \sim 80$ Å and $\ell = 115$ Å, we deduce $\lambda_{L\parallel} \sim 1000 \pm 90$ Å. We found that these values, along with a choice of gap ratio $2\Delta(0)/k_B T_c$, yield the best fit (Solid lines in **Figure 5.9** and **Figure 5.10** for our experimental $\lambda_{\parallel}(T)$ data. We also note that in **Figure 5.10**, $d\lambda_{\parallel}/dy$ diverges for $y < 1.3$, similar to what Schawlow and Devlin[34] and other investigators had seen in conventional superconductors as evidence of a finite energy gap in the low-lying excitation spectrum of the superconductor. Indeed, in **Figure 5.10**, we show without any ambiguity the BCS features with the gap ratio $2\Delta(0)/k_B T_c = 4.06$ (corresponding to $\Delta(0) \approx 3.67$ meV.) This value of the energy gap is in good agreement with the tunneling results on a NCCO single crystal by Huang et al.,[35] and is also consistent with the gap value obtained from the exponential

146
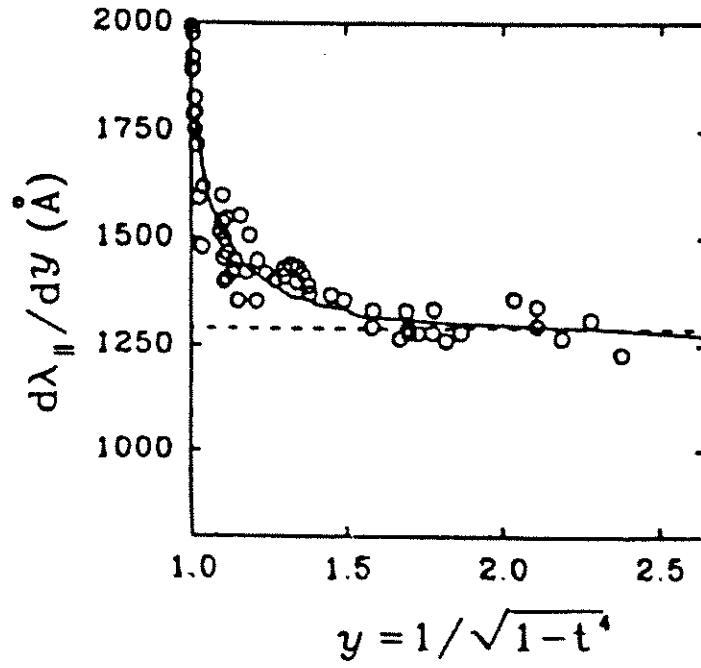
Figure 5.10 $d\lambda_\parallel/dy$ as a function of $y \equiv 1/\sqrt{1-t^4}$ for a NCCO thin film. The solid line is a BCS calculation. The horizontal dashed line is a two fluid temperature dependence with $\lambda_\parallel(T) = 1300\mathring{A}/\sqrt{1-(T/T_c)^4}$ and $T_c = 21$ K.

147

dependence of the raw f(T) and Q(T) data. Recent Raman experimental results support an isotropic gap in NCCO.[36]

Using $\lambda(0) \approx 1000$ Å, $\Delta(0)/k_B T_c = 2.03$ and the BCS expression in the low-temperature limit,

$$\delta\lambda(T) \equiv \lambda(T) - \lambda(0) = \lambda(0) \, (\pi \, \Delta(0)/2k_B T)^{1/2} \exp(-\Delta(0)/k_B T), \qquad (16)$$

we obtained an excellent quantitative description for $\delta\lambda(T)$ at low temperatures (dashed line in **Figure 5.9**. This detailed agreement for $\lambda(T)$ implies a single-gap s-wave BCS-like behavior over the entire temperature range, in strong contrast to $\lambda(T)$ and $R_s(T)$ measurements in YBCO.[37] [38]

These electrodynamic properties are further validated by the results of measurements, in which we cross examine several fundamental properties which were identified from $\lambda(T)$. The behavior of the surface resistance R_s with temperature for a thin film is shown in **Figure 5.11**. To obtain a quantitative agreement (solid line in the main figure) between the theoretical R_s and the experimental R_{sexp}, we use parameter values which are modified slightly from those for $\lambda(T)$, and further use a modified relation $A^* R_s = R_{sexp} - R_0$, where A^* is a correction factor, and R_0 is the temperature-independent residual resistance, as is commonly done in conventional superconductors.[31] To our knowledge, the most detailed comparison between BCS theory and experiment was done by Turnaeure, et al. on niobium.[39] They obtained a residual resistance of 10^{-2} μΩ at 10 GHz, with a correction factor $A^* \approx 1.1$. The correction factor $A^* \approx 1.35$ used in this work implies that the parameter values are reasonable. Here, we note that although the data display good agreement with the calculation over the entire temperature range, a slight mismatch can be found very

148
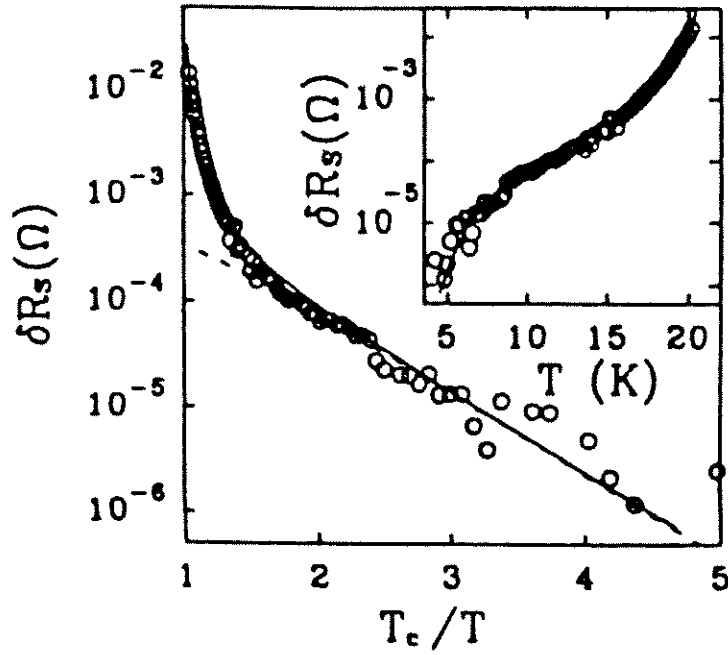
Figure 5.11 δR_s vs T_c/T for a NCCO thin film at 9.6 GHz with a BCS

calculation (solid line). Exponential behavior (dashed line) of

$\delta R_s(T) \propto \dfrac{(\hbar\omega)^2}{k_B T}\ln(\dfrac{4k_B T}{\hbar\omega})\exp(-\dfrac{\Delta}{k_B T})$ at low temperatures $(T_c/T>2)$ with

$2\Delta(0)/k_B T_c = 4.1$. Inset: δR_s vs T.

near T_c where a simple two-fluid like dependence $R_s \propto \lambda^3 (T/T_c)^4$ better fits the experimental data. This, we believe, indicates that a considerablenumber of unpaired charge carriers or quasi-particles exists at temperature near T_c. (It seems that R_s is much more sensitive to the existence of the unpaired charge carriers than λ.) Also we note that in contrast to the calculation of λ, the calculated R_s is much more sensitive to the choice of the parameter values, and the resulting values are less certain. Nevertheless, what is significant is the remarkable agreement over orders of magnitude between R_{sexp} and the BCS calculation in the entire temperature range. We also emphasize that our results clearly show the exponential behavior $Rs \propto e^{-\Delta(0)/k_BT}$ at low temperatures (dashed line in the inset of **Figure 5.11**, as expected from the raw $1/Q$ data.

Since λ and R_s are magnetic field dependent, and the comparison with the BCS calculation is valid only in the Meissner state, we need to prove that our results represent those of the Meissner state. **Figure 5.12** shows a typical microwave field dependence of R_s with a thin film sample, at $T = 20$ K. The data can be represented as

$$R_s(H_{rf}) - R_s(0) = g(T)H_{rf}^2, \tag{17}$$

where $R_s(0)$ is the surface resistance at zero field, $g(T)$ is an experimentally determined coefficient and H_{rf} is the rf magnetic filed strength parallel to the sample surface. This quadratic effect is a typical signature[40] that the sample is in the Meissner state where $H_{rf} < H_{c1}$. Because the microwave power used for measuring $\lambda(T)$ and $R_s(T)$ is in the range of -17dBm $< P_{\mu\text{-}}$ $_{wave} < 17$dBm (i.e. $H_{rf} < 12$ Oe $< H_{c1}$) throughout the entire experiment,
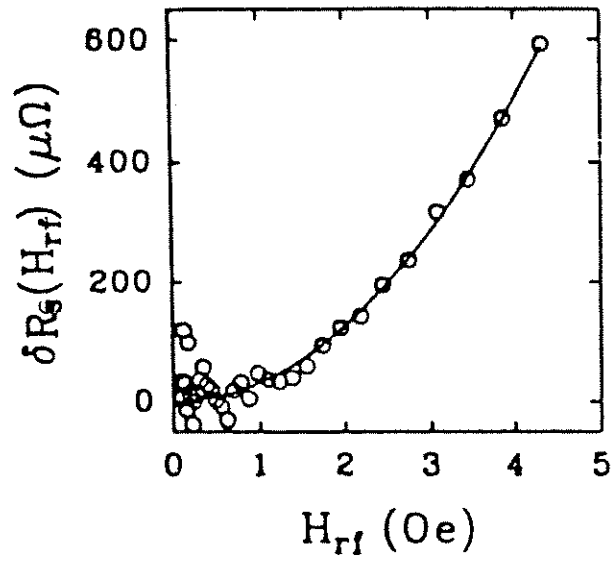
Figure 5.12 Microwave field dependence of $\delta R_s(H_{rf})$ for a NCCO thin film at T = 20.7 K. Solid line represents $\delta R_s(H_{rf}) = g(T)H_{rf}^2$ with g(20.7 K) = 24 $\mu\Omega/Oe^2$.

we believe our experimental results for $\lambda(T)$ and $R_s(T)$ represent those of the Meissner state.

We next explore the relationship of our experimental results with other physical parameter measured by other techniques. From the Ginzburg-Landau model[41] (expected to be hold near T_c), we derive the quadratic coefficient

$$g(T) = [R_s(0) / 2H_c^2]\Delta(0) / kT \tag{18}$$

to the first order approximation for $H_{rf} < H_{c1} < H_c$. Using the measured values $g(20.7K) = 2.4 \times 10^{-5}\ \Omega/Oe^2$, and $R_s(0) = 18 \times 10^{-3}\ \Omega$, and the relation

$$H_c = H_{c0}[1-(T/T_c)^2]^2, \tag{19}$$

we estimate the zero temperature thermodynamic critical field $H_{c0} \approx 2$ kOe. This value is larger that of polycrystalline $Sm_{1.85}Ce_{0.15}CuO_{4-y}$ (≈ 431 Oe)[42], but comparable to the estimated $H_c(0) \approx 2.5kOe$, obtained from

$$H_c = \Phi_0 / 2\sqrt{2}\pi\xi\lambda_L \tag{20}$$

using $\xi = 80\text{\AA}$ and $\lambda_L = 1000\text{\AA}$. Also using the in plane effective penetration depth $\lambda_a \approx 1300\text{\AA}$, the lower critical field $H_{c1,\perp} = 320Oe$ can be estimated from

$$H_{c1,\perp} = \frac{\Phi_0}{4\pi\lambda_{\|}^2}[\ln(\frac{\lambda_{\|}}{\xi_{\|}}) + 0.5]. \tag{21}$$

This value is an order of magnitude larger than a published value for a polycrystalline $Sm_{1.85}Ce_{0.15}CuO_{4-y}$[42] and comparable to $H_{c1,\perp}$ of YBCO.[43]

5-4 Comparison of Nb, NCCO and YBCO

In this section, the temperature dependence of the penetration depth, surface resistance, and the complex conductivity for Nb, NCCO and
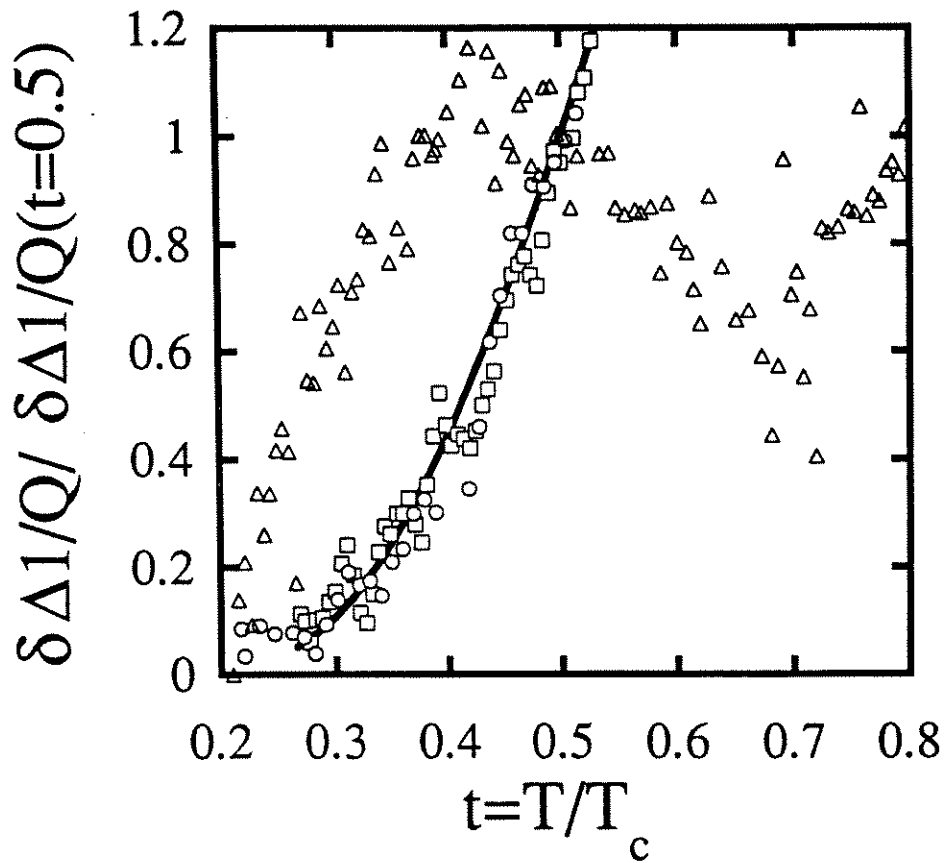
Figure 5.13 $[\Delta(1/Q(t))-\Delta(1/Q(t=0.2))]/[\Delta 1/Q(t=0.5)-\Delta 1/Q(t=0.2)]$
(proportional to $R_s(T)$) for $t \equiv T/T_c \leq 0.5$ for NCCO film (squares), Nb
single crystal (circles) and YBCO single crystals (triangles). Solid line is an
exponential fit mentioned in the text.
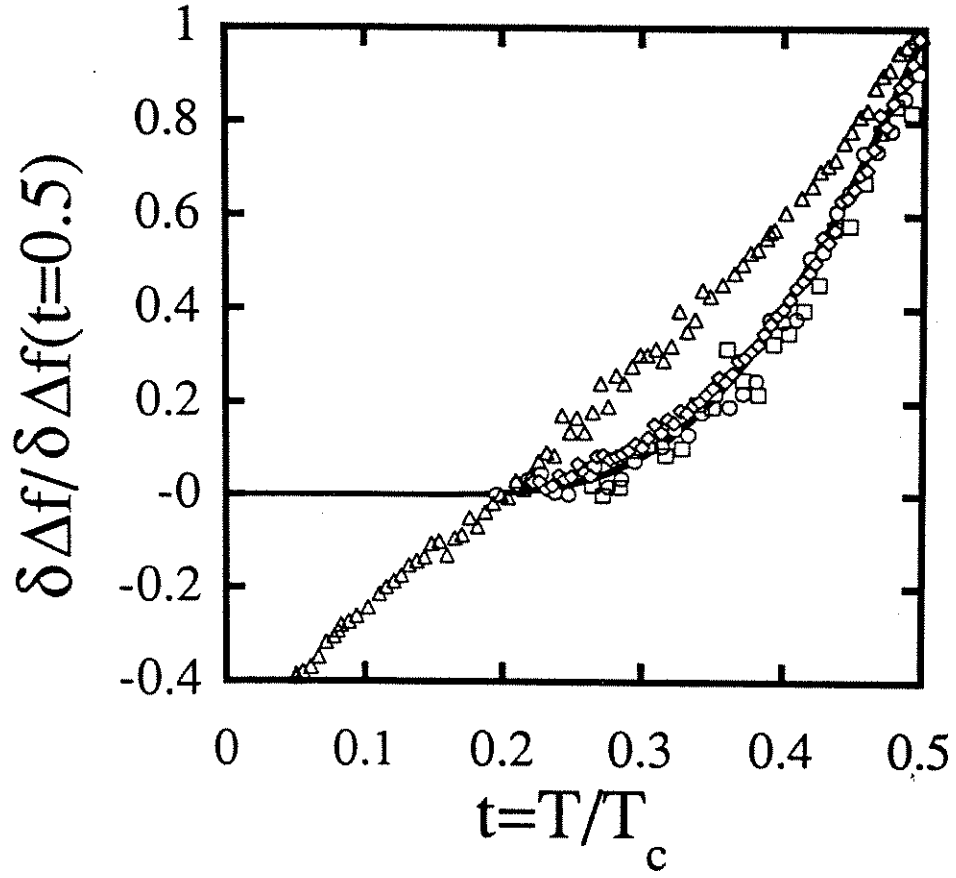
Figure 5.14 $[\Delta f(t)-\Delta f(t=0.2)]/[\Delta f(t=0.5)-\Delta f(t=0.2)]$ (proportional to $\Delta\lambda(t)$) for t

$\equiv T/T_c \leq 0.5$ for NCCO film (squares), NCCO single crystals (diamonds),

Nb single crystal (circles) and YBCO single crystals (triangles). Solid line is

an exponential fit mentioned in the text.
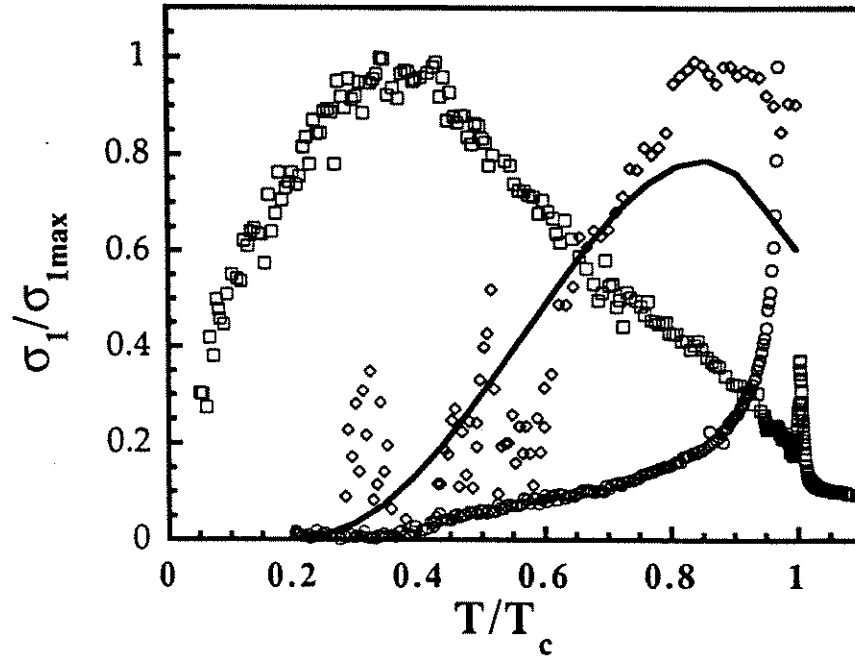
Figure 5.15 Real part of the complex conductivity $\sigma_1(T)$, normalized to its maximum value σ_{1max}, versus T/T_c for the ab-plane of single crystals of YBCO (squares, $\sigma_{1max} = 2.7 \times 10^7$ $(\Omega m)^{-1}$, $T_c = 90.1$ K), Nb (diamonds, $\sigma_{1max} = 3.5 \times 10^8$ $(\Omega m)^{-1}$, $T_c = 9.2$ K), and an NCCO thin film (circles, $\sigma_{1max} = 3.5 \times 10^7$ $(\Omega m)^{-1}$, $T_c = 21.5$ K). The solid line represents a calculated $\sigma_1(T)$ for Nb using the BCS s-wave model with gap ratio $2\Delta/k_BT_c \sim 4$. The absence of a coherence peak in the NCCO thin film data may be due to the finite thickness effect.

155

YBCO are examined in a comparative manner to provide a better understanding of these experimental results and the theoretical implications.

Figure 13 and **Figure 14** show the low temperature behavior of various samples: single crystals of Nb, NCCO and YBCO, as well as NCCO thin films. The data are plotted in a manner which normalizes away different geometry coefficients and T_c's. While there are obvious similarities between data from Nb and NCCO samples, a dramatic difference between YBCO and the rest of samples can been seen. Those similarities and differences are discussed in the following:

(1) In **Figure 5.13**, as $\Delta\lambda = -\zeta \, \Delta f$, the penetration depth in the ab plane, λ_{ab}, of YBCO crystals shows a linear temperature dependence for $T/T_c \leq 0.4$. The best fit for the frequency shift data of NCCO and Nb is consistent with the BCS s-wave model, yielding an exponential temperature dependence for $T/T_c \leq 0.5$ with an activation barrier $2\Delta(0)/k_B T_c \approx 4.0 - 4.2$.

(2) In **Figure 5.14**, the best fits to $R_s(T)$ for Nb and NCCO samples are again consistent with the BCS s-wave model which is also suggested by the exponential behavior with the gap ratio $2\Delta(0)/k_B T_c \approx 4.0 - 4.2$. For YBCO, however, the temperature dependence of the surface resistance is non-monotonic and is quite different from the BCS s-wave model. It shows a sub-linear temperature dependence from 4.2K up to 30 K, before it reaches a broad peak around 40 K and a dip around 70 K, which resembles the feature of the Univ. of British Columbia's results.[1][4]

156

(3) There are very sharp drops just below T_c for both the penetration depth and the surface resistance of YBCO, as shown in **Figure 3.4 and Figure 3.5**. This indicates that the temperature dependence of those parameters are not similar to the conventional BCS superconductors even near the transition temperature.

(4) **Figure 15** shows the real part of the complex conductivity σ_1 of YBCO, NCCO and Nb. The σ_1 of Nb displays a well defined BCS coherence peak and overall good agreement with the BCS s-wave model. Although the conductivity data from NCCO in general follows the conventional temperature dependence, the coherence peak is not seen, possibly due to the finite thickness effect of the NCCO film. By Eq. (3.24) of Chapter 3, the finite thickness effect of the film becomes significant when the value of the penetration depth λ becomes comparable to the thickness t. It is precisely in this temperature range that the delicate balance of the bulk $R_s(T)$ and $X_s(T)$ give rise to the coherence peak in σ_1. Since the corrections to R and X generated by the finite thickness effect can approach 100%, the de-convolution of the effective impedance data to determine $\sigma_1(T)$ is not reliable. In contrast to Nb and NCCO samples, the conductivity of YBCO can not be reconciled with the BCS s-wave model. The real part of the conductivity σ_{1-ab} of the YBCO sample follows a linear T-dependence for T<30 K, shows a broad peak near T~35 K, and another peak at the transition temperature. Neither peak in $\sigma_{1-ab}(T)$ is attributed to the coherence effect. The peak around 35 K has been ascribed to the

competition between the unusual rapid increase of the quasiparticle scattering time τ and the decreasing density of quasiparticles as the temperature decreases.[6] The second peak in $\sigma_{1\text{-ab}}(T)$ occurs just below T_c precisely at the point where $\sigma_{1-ab} = \sigma_{2-ab}$ and it is not seen from Nb data. The origin of the second peak may due to flunctuations or inhomogeneities.[44][45]

5-5   Discussion

There are many theories and models on high T_c superconductivity. [46-49] Many experiments have been performed to study high T_c superconductivity, most of them on the hole-doped superconductors. Earlier observations are interpreted in terms of an s-wave BCS behavior, although there was no clear low-temperature exponential activation of the surface resistance and penetration depth[50][51]. Measurements of the penetration depth of YBCO epitaxial thin films have been interpreted in terms of a weak s-wave superconducting state associated with the CuO chains[52], or as a manifestation of weak links between grains[53][54]. The confusion regarding the electrodynamic properties of YBCO is due, in part, to its complex microstructural properties. Its short coherence length can easily give rise to a plethora of weak-link phenomena[54], while the presence of twin boundaries can interrupt the highly conductive Cu-O chains in the structure. Aside from the s-wave pairing, some models postulate that the pairing mechanism involves the exchange of antiferromagnetic spin fluctuations.[55] Monte Carlo calculations based on the Hubbard model suggest that pairing occurs in the $d_{x^2-y^2}$ channel.[56]

158

There was also strong evidence for a d-wave picture on high quality single crystals recently.[3] [4]

Relatively little progress has been made with NCCO up to this work, because of the difficulties in preparing homogeneous, single-phase samples.[57][58] In principle, NCCO should be one of the simplest and easily understood examples of the cuprate superconductivity. NCCO has a single Cu-O plane layer, tetragonal crystal structure at the optimum superconducting doping, and relatively long in-plane coherence length. During this work, we have examined over 20 samples NCCO samples and 10 YBCO samples.

Some key physical properties of the NCCO and YBCO materials are contrasted in **Table II**. One major difference between NCCO and YBCO is the fact that YBCO is an ordered, stoichiometric compound at optimal doping, whereas NCCO is thought to be a random alloy due to the disordered Ce doping on Nd sites. In addition, for both cuprates, there is disorder on the oxygen sites, as suggested by work on the YBCO CuO chains, and by electron microscopy on NCCO.[59] It may be that due to its disordered nature, NCCO shows a non-linear normal-state resistivity $\rho_n(T) \sim T^2$ with signs of a constant residual resistivity setting in above T_c.[60] Magnetoresistance measurements by References [33][61] also show that the underdoped NCCO material shows evidence of weak localization of the charge carriers. From transport measurements, Jiang et al., have shown that excessive oxygen in as-prepared NCCO crystals may cause localization of electrons introduced by Ce doping.[62] We speculate that poor oxygen stoichiometry, or the random doping of Ce, may be

159

responsible for the observation of weak localization. Finally, the high RBS channeling yields in NCCO films (see **Figure 4.4**) also suggest a great density of point defects. In summary, several types of data all suggest that NCCO is a more disordered material than the hole-doped YBCO.

To our knowledge, the differences in electronic structure of cuprates between electron and hole doping have not been explored in detail. Starting from an antiferromagnetic insulator and doping with holes is thought to increase the magnetic frustration in the copper-oxygen planes and quickly extinguish long-range antiferromagnetic order.[63] Electron doping, on the other hand, is thought to simply dilute the spin system in the copper-oxygen planes, allowing for persistance of antiferromagnetic correlations to much higher doping levels. Whether these correlations still exert some influence in the superconducting state is not known, but the asymmetry of carrier is clearly important. Whether or not this asymmetry has an effect on the symmetry of the ground state superconducting wave function is not known either. However, Rokhsar proposes that electron doping a Mott insulator will lead to s-wave pairing in the superconducting state, while hole doping eventually leads to d-wave pairing.[64]

Lee has suggested that the electrodynamic properties of d-wave superconductors will be very sensitive to the presence of disorder. He predicts that a disordered d-wave superconductor will develop a "mobility gap" near the nodes of the d-wave energy gap.[65] Below this mobility gap, the low-lying quasiparticle states will become localized on relatively short length scales and effectively no longer participate in transport processes.

The surface resistance and penetration depth may also be affected by this localization, and show a disorder-induced artificial energy gap in their low-temperature dependence. According to this picture, the measured energy gap in NCCO will be very sensitive to the type and the extent of disorder in the thin films and single crystals.

Several experimental observations are not consistent with the mobility gap idea. First is our observation of very nearly the same activated temperature dependence of λ and R_s in both thin films and single crystals. It is commonly believed that the nature of disorder is entirely different in thin films and single crystals. The thermodynamic and kinetic conditions present during growth of a film and crystal are very different, and arguments hinging on this difference have been made before to explain the high residual losses in YBCO crystals as compared to YBCO films.[1] Hence we find it difficult to believe that the same disorder-induced mobility gaps would develop in our films and crystals of NCCO.

A second experimental observation at odds with the mobility gap idea is the work of N. Klein et al. on the oxygen dependence of the surface resistance in YBCO thin films.[52] They found that the residual surface resistance decreased with longer annealing times in activated oxygen. At the same time, the activation energy for $R_s(T)$ at low temperatures increased with prolonged annealing. Klein et al. suggest that the annealing resulted in an increase in the oxygen content of the film and a decrease in the disorder of the oxygen sublattice. These results suggest that decreasing disorder among the oxygen in YBCO actually serves to increase the

activation barrier, quite the opposite from what is expected of a mobility gap.

The electrodynamic properties of d-wave superconductors have been calculated in detail by Hirschfeld and coworkers.[66][67] The find that very clean d-wave superconductors have a pure response in which the magnetic penetration depth increases linearly with temperature at low temperatures, as shown in Eq. (5). Below a characteristic temperature T*, which depends on the degree of disorder, a disorder-dominated limit is reached and the penetration depth increases quadratically with temperature:

$$\lambda(T) = \lambda + c_1 T^2 \qquad (22)$$

where

$c_1 \sim n_i^{-\frac{1}{2}}$ and n_i is the density of resonant scattering sites. In addition, $T^* \sim n_i^{-\frac{1}{2}}$, so the disorder dominated temperature range expands to ever higher temperatures with increasing disorder. For typical YBCO crystals we fit the penetration depth with the fitting form

$$\lambda = \lambda_0 + a \frac{T^2}{T^* + T}. \qquad (23)$$

for $T \leq T_c/2$, and we obtain T*~10 K. But the NCCO films and crystals show no sign of a linear temperature dependence, presumably because the density of resonant scatterers has pushed T* up above $T_c/2$. Note that increased disorder tends to decrease c_0, making the penetration depth temperature dependence look flatter at low temperatures. Hence in this d-wave picture, the explanation for our NCCO results is a large degree of resonant scattering which has pushed T* ≥ 20 K without significantly decreasing T_c. However, the fit to $\lambda(T) \sim T^2$ is still very poor, suggesting

that the simple approach of Hirschfeld et al., does not apply to extremely disordered materials like NCCO, or that NCCO is not a d-wave superconductor. From all of these observations, we conclude that the NCCO data can not be reconcile with the disordered d-wave electrodynamics calculations of Lee and Hirschfeld.

Other theoretical proposals of superconductivity in NCCO are based on phonon-mediated mechanisms of superconductivity. Point-contact tunneling spectroscopy measurements on NCCO by Huang et al. showed a low zero-bias conductance, much lower than is ordinarily found for the hole-doped cuprates. [35] They were able to extract the $\alpha^2 F(\omega)$ Eliashberg function from the $d^2 I / dV^2$ data by conventional techniques. The $\alpha^2 F(\omega)$ data bear some resemblance to the phonon density of states as obtained from inelastic neutron scattering.[68][69] They could calculate T_C in the context of Eliashberg theory, and found close agreement with the experimental T_C. Chen and Callaway have also calculated the T_C of NCCO based on the strong-coupling theory and the Eliashberg equations, and also found fairly satisfactory agreement with the experimental T_C.[70]

With our experimental data alone, we can not prove or disprove a particular theoretical model for the mechanism of superconductivity in NCCO or YBCO. However, as the data suggest, we propose that a theoretical model for cuprate superconductivity should be able to explain the electrodynamic properties of NCCO and YBCO, especially the differences, and how these properties depend on disorder.

5-6   Summary

163

In this chapter, we presented the results on the anisotropic surface resistance R_{s-ab} and R_{s-c}, as well as the penetration depth λ_{ab} and λ_c of $YBa_2Cu_3O_{7-\delta}$ (YBCO) single crystals measured at 9.6 GHz. We find that $\lambda_c(T)$ and $\lambda_{ab}(T)$ are linear in temperature at low temperatures with much different slopes, consistent with the existence of line nodes on a cylindrical Fermi surface. A collapse of the c-axis scattering rate below T_c is also observed, and the temperature dependence of the ab-plane scattering rate is consistent with quasiparticle-quasiparticle scattering. The behavior of $\lambda_c(T)$ is not consistent with proximity-effect models, or with cubic $d_{x^2+y^2-z^2}$ pairing symmetry, but is consistent with a cubic $d_{x^2-y^2}$ pairing state. However, the sub-linear temperature dependence of the real part of the conductivity $\sigma_1(T)$ at low temperatures is not consistent with the clean d-wave model.[4]

We presented the microwave surface impedance of high quality $Nd_{1.85}Ce_{0.15}CuO_4$ (NCCO) thin films and single crystals at 9.6 GHz. The measured results of the temperature dependence of the penetration depth λ and surface resistance R_s for both thin films and crystals are consistent with a single gap BCS s-wave behavior. At low temperatures ($T/T_c < 0.5$), both λ and R_s exhibit exponential temperature dependencies, which is one of the most distinctive features of an s-wave superconductor, and yield a single energy gap ratio $2\Delta(0)/k_BT_c = 4.1 \pm 0.2$. This gap ratio and the s-wave BCS temperature dependence are also found to be a good description of $\lambda(T)$ and $R_s(T)$ over the entire temperature range below T_c. [71]

We compared the experimental results of the surface impedance of electron-doped cuprate NCCO, hole-doped cuprate YBCO and

conventional low temperature superconductor Nb. As the measurements of different materials were made by the same technique in the same cavity, the comparison of R_s, λ, as well as the complex conductivity σ extracted from R_s and λ, is much more convincing in the study of the pairing symmetry and the electrodynamics of cuprates than data of R_s and λ taken separately as performed in reference [1][3].[72]

Experimental results indicate that the YBCO results show marked differences, while the behavior of the λ and R_s of NCCO is extremely similar to that of a BCS s-wave superconductor, such as Nb. The surface impedance results on NCCO appear in general identical for thin films and single crystals, and similar result on clean YBCO crystals have now been seen by two groups,[3][4][73] leading us to believe we may have intrinsic properties of these cuprates. If this is the case, then a broad theory which incorporates both s-wave and d-wave cuprates may need to be developed. There are also many different types of experimental results supporting this behavior (s-wave behavior for NCCO and d-wave behavior for YBCO). These inconsistencies of experimental observations between the two cuprate superconductors (NCCO and YBCO) may suggest that an s+d wave pairing state, with variable weighting of the two symmetries, may be appropriate for the cuprates.

REFERENCES

[1] D. A. Bonn, et al., Phys. Rev. B **47**, 11314 (1993).

[2] Z. -X. Shen, et al., Phys. Rev. Lett. **70**, 1553 (1993); D. A. Wollman, et al., Phys. Rev. Lett. **71**, 2134 (1993).

[3] W. N. Hardy, et al., Phys. Rev. Lett. **70**, 3999 (1993).

[4] Jian Mao, Dong Ho Wu, S. M. Anlage et al., Phys. Rev. B Rapid Communication **51**, 3316 (1995).

[5] R. A. Klemm and Samuel H. Liu, Phys. Rev. Lett. **74**. 2343 (1995).

[6] S. Chakravarty, et al., Science **261**, 337 (1993).

[7] T. Shibauchi et al., Phys. Rev. Lett. **72**, 2263 (1994).

[8] J. Annett, N. Goldenfeld, and S. R. Renn, Phys. Rev. B **43**, 2778 (1991).

[9] M. Prohammer and J. P. Carbotte, Phys. Rev. B **43**, 5370 (1991).

[10] C. E. Gough and N. J. Exon, Phys. Rev. B **50**, 488 (1994).

[11] S. M. Anlage, et al., Phys. Rev. B **50**, 523 (1994).

[12] For Nb, we found $R_S(T > T_C) \neq X_S(T > T_C)$; but in the case of YBCO, $X_{S-eff}(T > T_C)$ is always slightly (~10%) bigger than $R_{S-eff}(T > Tc)$.

[13] P. J. Hirschfeld, W. O. Putikka and D. J. Scalapino, Phys. Rev. Lett. **71**, 3705 (1993).

[14] E. F. Skelton, et al., Science **263**, 1416 (1993).

[15] M. S. Pambianchi, J. Mao and S. M. Anlage, Phys. Rev. B **50** , 13659 (1994).

[16] O. Klein, E. J. Nicol, K. Holczer and G. Gruner, preprint.

[17] Mean field behavior of $\lambda(T)$ is not observed near T_C, hence fits to the Gorter-Casimir model were made outside the critical regime. See S.

Kamal, et al., Phys. Rev. Lett. **73**, 1845 (1994) and S. M. Anlage, Jian Mao et al., preprint.

[18] K. Zhang, et al., Phys. Rev. Lett. **73**, 2484 (1994).

[19] J. Schützmann, et al., Phys. Rev. Lett. **73**, 174 (1994).

[20] The details of $\sigma_{2c}(T)$ are not reproducible from crystal to crystal, however, the general features that $\sigma_{2c}(T)$ is linear in T at low temperatures and shows upward curvature at higher temperatures are seen in all crystals. The temperature dependence of σ_{2c} is reminiscent of the Josephson-coupling model of refs. 7 and 30 with an SNS-like $J_c(T)$.

[21] F. Marsiglio, J. P. Carbotte and J. Blezius, Phys. Rev. B **41**, 6457(1990).

[22] H. Chi and J. P. Carbotte, Phys. Rev. B **49**, 6143 (1994).

[23] YBCO crystals measured at 34.8 GHz in ref. 18 extrapolate to $R_{sab} \sim$ 140 $\mu\Omega$ or 205 $\mu\Omega$ (using ω^2 or $\omega^{1.7}$ scaling, respectively) at 10 GHz.

[24] T. A. Friedmann, et al., Phys. Rev. B. **42**, 6217 (1990).

[25] C. C. Homes, et al., Phys. Rev. Lett. **71**, 1645 (1993).

[26] Applying the two-fluid model to the c-axis data is problematic because it is not clearly in the clean limit. See D. A. Bonn, et al., Phys. Rev. Lett. **72**, 1391 (1994). However, we shall assume that $\xi_c/\ell_{mfp,c} < 1$ at all temperatures, so that the c-axis electrodynamics is never in the extreme dirty limit.

[27] S. M. Quinlan, D. J. Scalapino, and N. Bulut, Phys. Rev. B **49**, 1470 (1994).

[28] In the scattering rate analysis, residual normal fluid fractions x_{n0} of 2% and 31% are added for the ab-plane and c-axis, respectively, to

keep $\omega\tau \leq 1/2$ (see ref. 1). However, if one uses the constraint that $f(\omega\tau)$ approaches its low temperature value with zero slope, one finds x_{n0} of 5 % and ~ 50%, respectively.

[29] P. J. Hirschfeld, and N. Goldenfeld, Phys. Rev. B **48**, 4219 (1993).

[30] D. N. Bosov, et al., Phys. Rev. B **50**, 3511 (1994).

[31] J. P. Turneaure et al., J. Supercond. **4**, 341 (1991).

[32] Yoshikazu and M. Suzuki, Nature (London) **338**, 635 (1989).

[33] S. J. Hagen *et al.*, Phys. Rev. B **45**, 515 (1992).

[34] A. L Schawlow and G. E. Devlin, Phys. Rev. **113**, 120 (1959); P. C. L. Tai, M. R. Beasley, and M. Tinkham, Phys. Rev. B **11**, 411 (1975).

[35] Q. Huang et al., Nature **347**, 369 (1990).

[36] B. Stadlober et al., Phys. Rev. Lett. **74**, 4911 (1995).

[37] S. M. Anlage et al., Phys. Rev. B **44**, 9764 (1991).

[38] N. Klein, J. Supercond. **5**, 195 (1992).

[39] J. P. Turneaure and I. Weissman, J. Appl. Phys. **39**, 4417 (1968).

[40] S. Sridhar et al., Phys. Rev. Lett. **63**, 1873 (1989).

[41] V. L. Ginzburg and L. D. Landau, Zh. Eksp. Teor. Fiz. **20**, 1969 (1950).

[42] Almasan et al., Phys. Rev. B **45**, 1056 (1992).

[43] Dong Ho Wu and S. Sridhar, Phys. Rev. Lett. **65**, 2074 (1990).

[44] Steven M. Anlage, Jian Mao, J. Booth and Dong Ho Wu, Submitted to Phys. Rev. B. Rapid Communication.

[45] Dong Ho Wu, J. Booth and Steven M. Anlage, Phys. Rev. Lett., August 1995.

[46] P. W. Anderson, Physica C **185**, 11 (1991).

[47] J. R. Schrieffer, Physica C **185**, 17 (1991).

[48] D. J. Scalapino, Physics Reports, in press.

[49] M. Tachiki, Y. Muto, Y. Syono, editors, Materials and Mechanisms of High Temperature Superconductivity, North-Holland, Elsevier Science Publishers B. V. (1991).

[50] L. Krusin-Elbaum et al., Phys. Rev. Lett. **62**, 217 (1989).

[51] D. R. Harshman et al., Phys. Rev. B **39**, 851 (1989).

[52] N. Klein et al., Phys. Rev. Lett. **71**, 3355 (1993).

[53] S. M. Anlage et al., Phys. Rev. B **44**, 9764 (1991).

[54] J. Halbritter, J. Appl. Phys. **68**, 6315 (1990).

[55] N. E. Bickers, D. J. Scalapino, S. R. White, Phys. Rev. Lett. **62**, 961 (1989).

[56] Bulut, D. J. Scalapino, and S. R. White, Phys. Rev. B **47**, 14 599 (1993).

[57] R. Lightfoot et al., Physica C **168**, 627 (1990).

[58] A. R. Drews et al., Physica C **200**, 122 (1992).

[59] T. Williams et al., Physica C **161**, 331 (1989).

[60] C. C. Tusei, Phsica A 168, 238 (1990).

[61]   Andreas Kussmaul, Ph. D. thesis, MIT, 1992.

[62] W. Jiang et al., Phys. Rev. B **47**, 8151 (1993).

[63] Beom-hoan O and J. T. Markert, Phys. Rev. B **47**, 8373 (1993).

[64] D. S. Rokhsar, Phys. Rev. Lett. **70**, 493 (1993).

[65] P. A. Lee, Phys. Rev. Lett. **71**, 1887-1890 (1993).

[66] P. J. Hirschfeld et al., Phys. Rev. Lett. **71**, 3705 (1993).

[67] P. J. Hirschfeld and N. Goldenfeld, Phys. Rev. B **48**, 4219 (1993).

[68] J. W. Lynn et al., Phys. Rev. Lett. **66**, 919 (1991).

[69] N. Tralshawala et al., Phys. Rev. B **44**, 12102 (1991).

[70] H. Chen and J. Callaway, Phys. Rev. B **46**, 14321 (1992).

[71] D. H. Wu, Jian Mao, S. M. Anlage et al., Phys. Rev. Lett. **70**, 85 (1993).

[72] Jian Mao, et al., Physica C **235-240**, 2013-2014 (1994).

[73] S. M. Anlage, et al., Phys. Rev. B **50**, 523 (1994).

	Microwave	measurements	dc magnetization
	Thin films	Single crystals	Single crystal
T_c (K)	21	21.5	22
$\lambda_\parallel$ (0) (Å)	1300 ± 100	1250 ± 200	1100 ± 300
$\xi_\parallel$ (0) (Å)	72 - 80 [a]	80	N/A
R_0 (mΩ)	2.5	1	N/A
ℓ (Å)	115 - 600 [a]	300 ± 200	N/A
$2\Delta/kT_c$	4 - 4.3	3.9 - 4.3	3.9 - 4.5
$\lambda_{L\parallel}$ (0) (Å)	1000 ± 90	1050 ± 200	N/A

[a] For R_S (T), $\xi_\parallel$ (0) ~ 72 Å and ℓ ~ 600 Å. For $\lambda_\parallel$ (T), $\xi_\parallel$ (0) ~ 80 Å and ℓ ~ 100 Å.

TABLE I   Electrodynamic parameters used to fit the $\lambda_\parallel$ (T) and R_S (T) data with the BCS calculation for $Nd_{1.85}Ce_{0.15}CuO_4$. Parameters above the center line were determined by independent means, and those below the line were used as fitting parameters.

TABLE II. Contrasting physical properties of $YBa_2Cu_3O_7$ and $Nd_{1.85}Ce_{0.15}CuO_4$.

Property	$YBa_2Cu_3O_7$	$Nd_{1.85}Ce_{0.15}CuO_4$
Crystal structure at maximum T_c	Orthorhombic	Tetragonal
Conducting layers in unit cell	Double CuO_2, Cu-O chain layer	Single CuO_2, no chains
Apical oxygens	Distorted but occupied	Nominally unoccupied
"Order"	"Stoichiometric compound"	"Random alloy"
T_c	~92 K	~22 K
Coherence length		
In-plane	ξ_{ab} ~10–15 Å	ξ_a ~70–80 Å
c direction	ξ_c ~2–5 Å	ξ_c ~15 Å
Mass anisotropy m_c/m_{ab}	6	21 25
Sign of carriers:		
Nominal doping	Holes	Electrons
Hall effect (at max T_c)	Holes	Electrons
Thermopower	Holes (except for $YBCO_{7.0}$)	Holes
Photoemission FS	Holes	Holes
Normal state:		
Resistance	$\sim T$	$\sim T^2$
Scattering rate	$\sim \omega$	$\sim \omega$
Hall angle: $\cot\theta_H$	$\sim T^2$	$\sim T^4$

172

CHAPTER 6

CONSEQUENCES OF D-WAVE SUPERCONDUCTIVITY FOR HIGH FREQUENCY APPLICATIONS OF CUPRATE SUPERCONDUCTORS

In the search for the orbital symmetry of cuprate superconductors, there are a series of experiments consistent with a strong $d_{x^2-y^2}$ symmetry component to the order parameter for YBCO. As YBCO is the most widely used material for high T_c applications, it is worthwhile to understand the applications aspects of d-wave superconductivity. However, there are many other experiments which are not consistent with d-wave symmetry. Examples have been given in Chapter 1. Note that most of these experiments can be understood in terms of a linear combination of gaps, Δ_s and $\Delta_{d_{x^2-y^2}}$, with a relative weighting that varies with material.[1] A composite gap of this nature is consistent with the symmetry of the orthorhombic crystal structure of most hole-doped high-T_c cuprates.

In this chapter, we would like to speculate about the implications of d-wave superconductivity on the applications of the cuprates to high frequency technology. We rely mainly on the theoretical arguments of P. Hirschfeld, *et al.*, and P. Lee, and explore the properties of both "pure" and "disordered" d-wave superconductors.

6-1   "Pure" d-wave superconductors

173

First, since the d-wave pairing state involves lines of nodes in the energy gap on the Fermi surface,[2] a perfect cuprate will have a non-zero density of low-lying excited states down to arbitrarily low energies. This means that the surface resistance of such a material will not be thermally activated at low temperatures. P. Lee has estimated the minimum conductivity associated with a "pure" d-wave superconductor, and finds (in 3 dimensions)

$$\sigma_{min} \sim \frac{e^2}{h} \frac{\xi_0}{a} \frac{1}{s},$$ (1)

where ξ_0/a is the ratio of the in-plane coherence length to the lattice parameter, and s is the inter-layer spacing.[3] Note that this minimum conductivity estimate is independent of disorder, hence it should hold for both single crystals and thin films. In the low temperature limit in the superconducting state, where $\sigma_2 \gg \sigma_1$, the limiting surface resistance will be

$$R_{smin} \sim (\mu_0\omega)^2 \lambda^3 \sigma_{min}/2.$$ (2)

For YBCO ($\lambda \sim 1500$ Å, $\xi_0/a \sim 4$, s ~ 7 Å) at 10 GHz the estimate gives $R_{smin} \sim 1 \mu\Omega$, roughly an order of magnitude lower than the lowest R_s ever recorded in YBCO thin films in the microwave range. This would imply that the surface resistance of YBCO can still be further improved by making more ordered samples, at least if this "pure" d-wave picture is appropriate for YBCO films, crystals, and ceramics. This estimate also indicates that pure cuprates with shorter ξ_0 will have lower residual surface resistances. Hence the lowest $R_{s,min}$ should be found in the material with the highest T_c, although the improvement may not be so great upon going from a material with $T_c = 90$ K to one with $T_c = 150$ K.

As we have discussed in Chapter 5, the penetration depth in a "pure" d-wave superconductor should increase linearly with temperature at low temperatures, $\lambda(T) = \lambda_L + c_1\, T$, $(T \ll T_c)$ where λ_L is the London penetration depth, and $c_1 \sim 2$ to 4 Å/K for YBCO.[4][5] This value is surprisingly close to the observations of Hardy, et al. and Mao, et al., in twinned YBCO crystals[2][6][7], but is clearly not appropriate for the data on YBCO thin films and powders, or for NCCO. Superconductors with such a strongly temperature dependent penetration depth would clearly not be desirable for precision delay lines or low phase noise oscillators, particularly in the absence of an ultrastable cryocooler. As we shall see below, disordered d-wave superconductors should have less temperature dependence in their penetration depth, especially at low temperature.

6-2   Disordered d-Wave Superconductors

In reality, most cuprate superconductors used in applications are in thin film form and are often highly defective. The fact that thin film T_c's are often several degrees below those of single crystals is a sign that the films are either not optimally doped, or have sufficient disorder to decrease T_c by a "pair-breaking" effect. Both sources of a suppressed T_c involve some kind of disorder in the conducting layers of these materials. The effects of disorder on the properties of a d-wave superconductor are not entirely understood and are currently the subject of intense theoretical and experimental investigation. However, a few general remarks can be made about disorder.

In conventional s-wave superconductors, there are two types of defects which must be considered. Non-magnetic defects which produce elastic scattering have very little effect on superconductivity. Magnetic impurities, on the other hand, break time-reversal symmetry, thus interfering with the Cooper pairing process. This results in a substantial decrease in T_c, as well as a modification of the BCS density of states. The singularity in the density of states at the gap energy is smeared out, and states begin to fill into the gap as magnetic impurities are introduced. At a critical concentration of magnetic impurities, an s-wave superconductor becomes "gapless," meaning that there are single particle excitations available even at zero energy. By the time this concentration is reached, the T_c of the material is just a small fraction of its original value.

In a d-wave superconductor things are somewhat different. Because of the symmetry of the d-wave state, non-magnetic impurities now become pair-breakers as well.[8] The effect of disorder on the electrodynamic properties depends on the strength of the interaction of an individual scattering event, c, which is the cotangent of the scattering angle in the collision. The limit c -> ∞ corresponds to weak scattering (Born approximation), and c -> 0 is strong scattering (unitary limit). It is found theoretically that any amount of disorder causes "gapless" behavior (as defined above) in any three-dimensional d-wave superconductor.[4] The magnetic penetration depth would then vary as

$$\lambda(T) \sim \lambda_0 + c_2 T^2 \qquad (T \ll Tc) \qquad (3)$$

where

$$c_2 \sim \pi k_B^2 \lambda_L / (3.8 \Gamma^{1/2} \Delta_0^{3/2}), \qquad (4)$$

176

Γ is a scattering energy scale proportional to the density of strong scatterers, n_i, and λ_0 is related to the London penetration depth.[4]

In the presence of disorder, theory predicts a cross-over temperature T^* between a low temperature "gapless" regime, and a high temperature "pure" regime. Estimates of

$$T^* \sim 0.83\sqrt{\Gamma\Delta_0 / k_B^2} \qquad (5)$$

show that it increases roughly as the square root of the number of strong scatterers, $n_i^{1/2}$, as does $(\lambda_0 - \lambda_L)/\lambda_L$.[4] The penetration depth should therefore follow a general temperature dependence of the form

$$\lambda = \lambda_0 + a\frac{T^2}{T^*+T}. \qquad (6)$$

From this, one can estimate that $c_2 \sim c_1/T^*$, so for a typical YBCO film with $T_c = 90$ K and $T^* \sim T_c/4$, $c_2 \sim 0.2$ Å/K^2, surprisingly close to the values measured in YBCO films[9], and that obtained from the low temperature ($T \ll T_c$) expansion of an empirical fit to experimental data on YBCO films:[10-12] $\lambda(T) = \dfrac{1500\text{Å}}{\sqrt{1-(T/T_c)^2}}$.

The losses in the "pure regime" ($T^* < T \ll T_c$) in a d-wave superconductor may give us some insight into the losses at 77 K in the cuprates. At temperatures greater than T^*, but with a very low density of strong scatterers such that the measurement frequency $f \gg \Gamma\Delta_0/(hk_BT)$, one expects $\sigma_1 \sim n_i$,[13] and therefore $R_{s,pure} \sim \sigma_1 \sim n_i$, so that the losses will increase with impurity density, as one expects for s-wave superconductors. This case probably pertains only to the purest of single crystals, and may require several more years of materials refinement to achieve. However, for much more defective materials (remember $\Gamma \sim n_i$) such that $f \ll \Gamma\Delta_0/(hk_BT)$, one expects $\sigma_1 \sim 1/n_i$,[13] and $R_{s,pure} \sim 1/n_i$, quite different

from the clean limit. In this limit, the losses will actually decrease with additional non-magnetic disorder! This may have already been observed in surface resistance measurements on YBCO crystals doped with Zn.[14] However, the reduction in T_c due to the presence of strong scatterers is roughly $\Delta T_c / T_{c0} \sim \Gamma / \Delta_0$ and scales with n_i. Since it is more practical to make device materials with a large density of defects (especially in thin film form), a compromise must be found between the defects added to reduce the pure limit loss, and the need to keep the transition temperature substantially greater than the operating temperature of the device.

Finally, P. Lee has proposed that disorder in d-wave superconductors may lead to localization of low-lying quasiparticle states near the nodes of the energy gap.[3] This proposal may account for our observations of activated behavior in the surface impedance of NCCO,[15][16] and YBCO thin films overdoped with oxygen.[17] In addition, it may also allow for the creation of s-wave-like cuprate materials which can mimic the low-loss properties of traditional isotropic s-wave superconductors.

6-3 Other Effects of d-Wave Superconductivity

Due to the presence of nodes in the energy gap, a d-wave superconductor should exhibit a non-linear Meissner effect. This means that the superconductor will not generate a magnetization which is strictly proportional to the applied field, because supercurrent flowing in the direction of a node will gain kinetic energy sufficient to produce depairing, hence reducing the superfluid response. Because the gap increases for directions just away from the node, the amount of depairing will depend on

178

the strength of the applied field. Yip and Sauls have estimated that for low temperatures and small applied fields H, the effective penetration depth will behave as

$$\lambda_{eff}(H) = \lambda(H = 0) / [1 - \tfrac{2}{3}\tfrac{H}{H_0}],$$ (7)

where H_0 is on the order of the thermodynamic critical field.[18]

This non-linear effect could limit the intrinsic linearity of cuprate devices operating in the Meissner state, although it is predicted to be rather small.[18] We can estimate the 1 dB compression point for the kinetic inductance of a thin film (thickness t < λ) device as follows. At low temperatures and fields, the kinetic inductance will increase as

$$L_{Kin}(H) = L_{Kin}(0) / [1 - \tfrac{2}{3}\tfrac{H}{H_0}]^2.$$ (8)

A 1 dB increase of kinetic inductance would therefore occur for a field strength of order $H/H_0 \approx 0.17$. For YBCO (with $B_0 \approx 1$ Tesla) this corresponds to a surface field on the order of 1500 Oe. Such field strengths are probably beyond H_{c1}, but are possible for fields parallel to the surface of a thin film, and can be achieved in stripline resonators.[19] However, most devices will become nonlinear at lower field levels due to the entry of magnetic flux at weak links. Hence this form of nonlinearity will not be an issue until other materials problems are resolved. So far, the non-linear Meissner effect has not been seen in either of two experiments on single crystals of YBCO.[20][21]

Finally, d-wave superconductors may have unique mid-gap states associated with a free surface having a normal in the direction of a node in the energy gap, and also possibly at twin boundaries.[22] These states could contribute to residual microwave losses, and may explain the reduction in

residual losses of untwinned YBCO crystals compared to their twinned counterparts.[23]

In conclusion, there is growing evidence for a strong $d_{x^2-y^2}$ component to the ground state wavefunction of the cuprate superconductors. d-Wave superconductivity implies a finite microwave residual loss in the cuprates, although defects can be used to engineer the magnitude and temperature dependence of the surface impedance. Other consequences of d-wave superconductor include intrinsic non-linearity of the surface reactance in the Meissner-state, and the possibility of unique mid-gap states contributing to the microwave losses.[24]

REFERENCES

[1]   V. J. Emery and J. F. Annett, private communication, 1994.

[2]   Jian Mao et al., Phys. Rev. B Rapid Commun **51**, , 3316 (1994).

[3]   P. A. Lee, Phys. Rev. Lett. **71**, 1887-1890 (1993).

[4]   P. J. Hirschfeld and N. Goldenfeld, Phys. Rev. B **48**, 4219-4222 (1993).

[5]   P. Arberg, M. Mansor, and J. P. Carbotte, Solid State Commun. **86**, 671-673 (1993).

[6]   W. N. Hardy et al., Phys. Rev. Lett. **70**, 3999-4002 (1993).

[7]   Jian Mao, et al., Physica C **235-240**, 2013-2014 (1994).

[8]   K. Ueda and T. M. Rice in "Theory of Heavy Fermions and Valence Fluctuations," T. Kasuya and T. Saso, Editors, Springer-Verlag, Berlin, pp. 267-276 (1985).

[9]   M. R. Beasley, Physica C **209**, 43-46 (1993); Zhengxiang Ma, et al., Phys. Rev. Lett. **71**, 781-784 (1993).

[10] D. A. Bonn et al., Phys. Rev. B **47**, 11314-11328 (1993).

[11] J. M. Pond et al., J. Appl. Phys. **59**, 3033-3035 (1991).

[12] J. F. Annett, and N. Goldenfeld, J. Low Temp. Physics **89**, 197-206 (1992).

[13   P. J. Hirschfeld et al., Phys. Rev. Lett. **71**, 3705-3708 (1993).

[14] K. Zhang, et al., Appl. Phys. Lett. **62**, 3019-3021 (1993).

[15] Steven M. Anlage et al., Phys. Rev. B **50**, 523-535 (1994).

[16] Dong Ho Wu et al., Phys. Rev. Lett. **70**, 85-88 (1993).

[17] N. Klein et al., Phys. Rev. Lett. **71**, 3355-3358 (1993).

[18] S. K. Yip and J. A. Sauls, Phys. Rev. Lett. **69**, 2264-2267 (1992).

[19] D. E. Oates et al., IEEE Trans.Appl. Supercon. **3**, 1114-1118, (1993).

[20] S. Sridhar, Dong-Ho Wu, and W. Kennedy, Phys. Rev. Lett. **63**, 1873-1876, (1989).

[21] J. Buan et al., Phys. Rev. Lett. **72**, 2632-2635 (1994).

[22] Chia-Ren Hu, Phys. Rev. Lett. **72**, 1526 (1994).

[23] K. Zhang et al., Phys. Rev. Lett **73**, 2484(1994).

[24] Jian Mao and Steven Anlage, IEEE Trans. Appl. Supercond. **5**, 1997 (1995).

CHAPTER 7

SUMMARY

In this work, we studied the microwave surface impedance of superconductors by employing a novel cavity perturbation technique. We have refined the technique in both theoretical and experimental aspects. To clarify the existing confusion over the conversion of the measured quantities to electrodynamic quantities, we carried out a first principles calculation by considering the fundamental principles underlying microwave measurements. Measurements were performed using a recrystallized Nb cavity which has a very high $Q \sim 2.3 \times 10^7$ and a resonant frequency stability $\delta f / f \sim 10^{-10}$ at $T = 4.2$ K.

$YBa_2Cu_3O_{7-\delta}$ (YBCO) and $Tl_2Ba_2CaCu_2O_8$ have been the most widely utilized materials for high T_c microwave applications. But among cuprates, in principle, $Nd_{1.85}Ce_{0.15}CuO_{4-y}$ (NCCO) should be the simplest and most easily understood examples of cuprate superconductivity. It has a single Cu-O plane layer, tetragonal crystal structure at the optimum superconducting doping, and relatively long in-plane coherence length $\sim$ 80 Å compared with 10 Å for YBCO. Because of the layered structure in these cuprates, the anisotropy study of the electrodynamic properties bears both practical and theoretical information. Hence, we studied the electrodynamic properties in the ab plane and along the c-axis of YBCO single crystals. Also we performed conclusive study of the electrodynamics

183

of NCCO, which will certainly contribute to the understanding of the mechanism of high temperature superconductivity.

During this work, we have examined over 20 NCCO samples, 10 YBCO samples and 5 Nb samples. We found that the electrodynamic properties of NCCO are extremely sample dependent: for high quality samples a single sharp transition and reproducible results are typical, while for poor samples multiple-transitions and irreproducible results are common, particularly at high frequencies. However, we have dramatically improved the quality of both thin films and single crystals of NCCO, making possible conclusive experiments on the intrinsic electrodynamic properties. For YBCO, the results are also sample dependent: for high quality samples, we have observed a linear temperature dependence of $\lambda_{ab}(T)$ at low temperatures with slope of 4~5 K, while for poorer samples $\lambda_{ab}(T)$ shows a power law behavior of T^n, with n in the range of 1.2 to 2. Here we define higher quality in terms of higher T_c, sharper transition, lower residual surface resistance and lower RBS channeling yield

We fabricated and characterized our NCCO, YBCO and Nb samples carefully to assure the quality of the samples. The following is a summary of the electrodynamic properties of Nb, NCCO and YBCO which we demonstrated unambiguously.

(a) For the first time, we demonstrated the exponentially activated behavior at low temperatures of the in-plane penetration depth $\lambda_{||}$ and surface resistance R_s of NCCO. The results reveals striking similarities to Nb, and can be well described within the BCS framework, yielding an energy gap ratio $2\Delta/k_B T_c = 4.1 \pm 0.2$ and the London penetration depth $\lambda_{L||}(0$

K) ~ 1000 Å, indicating that the electrodynamics of NCCO is consistent with a single-gap s-wave BCS behavior.

(b) For YBCO single crystals, the anisotropic surface resistance R_{s-ab} and R_{s-c} show a non monotonic temperature dependence, and the penetration depth $\lambda_c(T)$ and $\lambda_{ab}(T)$ are linear in temperature at low temperatures with slopes of 130Å/K and 4Å/K respectively. They are clearly inconsistent with s-wave BCS theory. Rather the temperature dependence of the penetration depth is consistent with the existence of line nodes on the Fermi surface. These results was also analyzed in terms of an unusual rapid decrease of quasiparticle scattering rate in the ab plane and c-axis below T_c. The overall anisotropic surface impedance temperature dependence is not consistent with either intrinsic or extrinsic proximity-effect models, but is consistent with a cubic 3D $d_{x^2-y^2}$ pairing state, except for the temperature dependence of $\sigma_1(T)$ at low temperatures.

A comparison of the R_s and λ of NCCO, YBCO and Nb results reveals similarities between NCCO and Nb. It also shows distinct differences between NCCO and YBCO. The distinct differences between NCCO and YBCO, although both of them posses several common features such as CuO planes, may suggest that the pairing in cuprates includes both s-wave and d-wave components, and that the dominant component may vary from one material to another. With this possible scenario, we made a brief discussion on the consequences of d-wave superconductivity for high frequency applications.

Future Work

This thesis work certainly provides a lot of experimental information on some of the key issues in high T_c superconductivity. For instance, our concrete results on NCCO may constrain future theoretical models to be able to explain the single gap s-wave behavior of certain cuprates. On the other hand, our microwave results on high quality YBCO single crystals suggest a d-wave model. It is clear that more work, both theoretically and experimentally, needs to be done to understand the mechanism of the pairing state of cuprate superconductivity. If we can do experiments at much lower temperature (i. e. far below 4.2 K), we may be able to obtain more interesting and conclusive results with much higher sensitivity because of the higher Q of the Nb cavity at lower temperature. This will require, of course, improving and maintaining the quality of the surfaces of the Nb cavity. It may also require using different microwave measurement methods, because the quality factor of the superconducting Nb cavity will be too high, i. e. $Q \sim 10^8$, to be measured by our current method using the HP 8510C system. Additional cryogenic equipment could be required. Microwave experiments at lower temperature range (below 4.2 K) on NCCO single crystals could be interesting. For the YBCO system, it may be possible to obtain samples with lower surface resistance by making untwinned single crystals and measurement on these samples may provide valuable information on $R_s(T)$ and $\sigma_1(T)$. Our results on twinned YBCO crystals show that the temperature dependence of R_s and conductivity σ_1 at low temperatures are different from the d-wave predictions. It will be also interesting to determine the origin of the peak in σ_1 near T_c. How much of it is due to inhomogeneity and how much is

due to fluctuation? What kind of role do fluctuations play in the cuprates? Also the doping effects on the behavior of R_S and penetration depth λ are an interesting subject to be studied in the future. We have the possibility of having excellent Pr-doped YBCO single crystals made here at the center. In the experiments studying Nb and YBCO junctions' properties (to see if YBCO is a d-wave superconductor), what will happen if the junction is made of NCCO and YBCO? It will also be very interesting to measure other types of high T_C materials, which may help to answer the role of CuO planes in causing the high T_c. Another thing we can do is use other modes of the Nb cavity to study the frequency dependence of the surface resistance, penetration depth, and conductivity. All these experiments can provide the experimental grounds to stimulate and test new theories and models and could help us to understand high temperature superconductivity.

I also think considerable research work related to the practical application aspects of superconductors must be done. Although our surface impedance data can provide information to be used in the design of microwave devices, a closer examination is required. For instance, there is a lot of concern about the power dependence of high T_C thin film microwave devices. We certainly have the capabilities to answer these questions. Also similar cavity perturbation techniques can be used to study the surface impedance properties under high magnetic field. The expertise and facilities at our Center can be used to help to design and fabricate improved high quality high T_C microwave devices, such as filters, which could be used for cellular base stations.